Characterization of Collisional Shock Structures Induced by the Stagnation of Railgun-driven Multi-ion-species Plasma-jets

Maximilian K. Schneider

Dissertation submitted to the Faculty of the

Virginia Polytechnic Institute and State University

in partial fulfillment of the requirements for the degree of

Doctor of Philosophy

in

Aerospace Engineering

Colin S. Adams, Chair

K. Todd Lowe

Wayne A. Scales

Bhuvana Srinivasan

December 16, 2016

Blacksburg, Virginia

Keywords: plasma-jet, shock-wave, plasma railgun, multi-ion-species plasma

Characterization of Collisional Shock Structures Induced by the Stagnation of Railgun-driven Multi-ion-species Plasma-jets

Maximilian K. Schneider

(ABSTRACT)

The study of shock-waves in supersonic plasma jets is essential to understanding the complex dynamics involved in many physical systems. Specifically, ion-species separation caused by a shock wave propagating through a plasma is an important but not yet well understood phenomenon. In inertial confinement fusion implosions, a shock wave precedes the rapid compression of a fuel pellet to ignition conditions that theory and computational studies suggest may be separating the fuel and reducing the neutron yield. In astrophysics, the shock wave produced when a supernovae explodes has been shown to have an effect on nucleosynthesis as a result of shock heating. In both these cases the time and length scales make them difficult to study experimentally, but experiments on more reasonable scales can shed light on these phenomena. This body of work provides the basis for doing just that. The work begins by describing the development of a small, linear, plasma-armature railgun designed to accelerate plasma jets in vacuum to high-Mach-number. This is followed by discussion of an experimental campaign to establish a plasma parameter space for the jets, in order to predict how effectively the accelerator can be used to study centimeter-scale shock structures in jet collisions. The final section presents an experimental campaign in which jet collisions are induced, and the resultant structures that appear during the collision are diagnosed to assess how conducive the experiment is to the future study of shock-wave induced species separation in laboratory plasmas. This work is a foundation for future experimental studies of ion-separation mechanisms in a multi-ion-species plasma.
This research was supported in part by the National Science Foundation under grant number PHY-1903442.

Characterization of Collisional Shock Structures Induced by the Stagnation of Railgun-driven Multi-ion-species Plasma-jets

Maximilian K. Schneider

(GENERAL AUDIENCE ABSTRACT)

Plasma, the so-called fourth state of matter, is an ionized gas that often behaves like a fluid but can also become magnetized and carry an electric current. This combination leads to a lot of interesting yet often un-intuitive physics, the study of which is very important for understanding a wide array of topics. One subset of this field is the study of shock-wave induced species separation. Just like the shock-wave a jet aircraft produces when it moves through the air at a speed greater than the speed of sound, a plasma shock is characterized by a large change in parameters like density, temperature, and pressure across a very small region. A shock-wave propagating through a plasma can cause different ion species present to separate out, a phenomenon that is driven by the gradients that are present across a shock front. Understanding how these mechanisms work is important to a number of applications, including fusion energy research and astrophysical events. The first section of this work discusses the design and development of a plasma-armature railgun, a device that can produce and accelerate jets of plasma to high-Mach-number within a vacuum chamber. The next and most substantive section of the work presents results from experimental campaigns to characterize the accelerated plasma jets and then to induce plasma-jet collisions with the hope of producing shock-waves that exist on time and spatial scales that can be readily measured in a laboratory setting. This work is a foundation for future experimental attempts to measure separation induced by a shock-wave in order to better understand these complex phenomena.

Dedication

To my family for their endless support

Acknowledgments

I would not be completing this body of work if it hadn't been for the help of a great number of people. I would first like to thank my committee members, Todd Lowe, Wayne Scales, and Bhuvana Srinivasan for their guidance and support throughout this process. I would also like to thank my committee chair and advisor, Colin Adams. Without his patience and support throughout the years I would not have been able to attend graduate school at Virginia Tech, much less graduate. I would also like to acknowledge all the other students that contributed to my research and this body of work. I have been truly blessed with an enormous amount of support from graduate and undergraduate students alike who have worked in the lab on this project over the years. In no particular order, those students include Ameer Mohammed, Matt Carrier, Michael Sherburne, Marius Popescu, David Dennis, Brandon Christensen, Josh Korsness, Jacob Adams, Brian Henderson, Andrew Watson, Eric McAchren, and Ian Bean. I'd now like to turn to my family and thank my parents, Chris and Klaus Schneider. I simply could not have asked for better parents. They have supported me in every way imaginable my entire life. They have always encouraged me to reach for the stars while also supporting every decision I make. Finally, I'd like to thank my wife, Katie. She has helped me reach this milestone through unimaginable levels of emotional, intellectual, and physical support. Through the many long nights of writing, debugging code, crunching numbers, analyzing data, and all the other tasks that constitute daily life for a graduate student, she was right there beside me for all of it, helping in every and anyway she could without even a single complaint. I will owe her for a lifetime for all she has done to help me get to where I am today; luckily, I have all that time with her to do so.

Contents

List of Figures

List of Tables

Chapter 1

Introduction

In the field of physics, the most meaningful research and significant progress is made when theorists, computationalists, and experimentalists all contribute and collaborate on a topic. When the balance of attention to a given topic is uneven between these groups, there are always open questions to be explored. One such topic is that of shock-wave-induced species diffusion (or species separation) in multi-ion-species plasmas, the study of the mechanisms that drive transport of charged and neutral particles when a shock-wave propagates through a plasma due to the large gradients in plasma parameters that are present at the position of a shock-front. A substantial amount of work by theorists and computationalists to predict and understand these phenomena has been accomplished, but there has been appreciably less work performed by experimentalists on the topic. Perhaps one reason for this could be the spatial and temporal scales of the real world situations where these effects have an impact, which tend to be either very small and fast, or extremely large and slow, both of which tend to be difficult to work with for an experimentalist.

The objective of this work is to develop the ability to experimentally study these complex phenomena, but on spatial and temporal scales that are more easily accessible and diagnosable in a laboratory setting. This is attempted using a device called a plasma-armature railgun, an electromagnetic plasma-jet accelerator that has been shown to be a great test-bed for consistently accelerating plasma jets to high-Mach-number. In this work, we use a railgun to collide a jet of plasma into a stagnant background plasma, producing a shock-wave

propagating through a multi-ion-species plasma than can be used for the future study of species separation.

1.1 Shock-waves in Plasmas versus Fluids

1.1.1 Shock-wave Propagation in a Neutral Fluid Mixture

A shock-wave is a very small region in a fluid within which the properties of the fluid change drastically. This occurs when an object travels through a fluid at a velocity higher than the speed of sound. The sound speed, a_0, in any given fluid depends on the fluid's molecular weight, M, temperature, T, and ratio of specific heat capacities, γ and is given by

$$a_0 = \sqrt{\gamma k_B T / M}. \tag{1.1}$$

The Mach number, $\mathcal{M}$ which is given as

$$\mathcal{M} = \frac{v_0}{a_0} \tag{1.2}$$

is the ratio of the object speed, v_0, to the sound speed.

To begin to understand how a shock-wave can drive separation in a mixture of fluids, consider the classic gas dynamics problem in which the instantaneous acceleration of a piston to velocity v_p accelerates a shock-wave that propagates through a homogeneous mixture of two gases. The speed of the shock-wave, v_s can be calculated analytically using the Rankine-

Hugoniot relations, and is given by

$$v_s = \frac{\gamma+1}{4} v_p + \left[\left(\frac{\gamma+1}{4} \right)^2 + a_0^2 \right]^{1/2} \tag{1.3}$$

As the sound speed is dependent on molecular mass, M, it will be different for each gas in the mixture, meaning that assuming there are no inter-species collisions, multiple shock-waves traveling at different velocities will propagate for each gas species [4]. Since the shock-wave is essentially a discontinuity in the fluid parameters, including density, the presence of a distinct shock-wave for each fluid separated by some finite distance means that there is no longer a homogeneous mixture of the two fluid species.

Now consider collisions between the two species. The mean free path between the two, the average distance a particle will travel before colliding with another, is given by

$$\Delta_{max} \sim \frac{v_s}{\nu_{12}} \tag{1.4}$$

where ν_{12} is the frequency of collisions between particles of different species. This mean free path is essentially the maximum distance that can exist between the two shock-waves [4].

1.1.2 Shock-waves in Plasmas

A plasma is a quasi-neutral mixture of electrons, ions, and neutral particles that exhibits collective behavior. As opposed to a gas or liquid, the free charged particles in a plasma allow it to carry an electric current and produce magnetic fields. The behavior of plasma

can sometimes be approximated using a fluid model, but plasmas also exhibit behavior that often requires the use of kinetic theory to understand. Like a fluid, under the right conditions, shock-waves can also propagate through plasma, but their structure and the physics necessary to explain them can be very different.

The initial studies of shock-waves in plasma, which were conducted in the 1950s and 60s, were mainly motivated by the desire to understand astrophysical systems such as a charged body traveling through the ionosphere or the interaction between the solar wind and Earth's magnetosphere [5]. This pioneering work by J. D. Jukes as part of the Atomic Energy Research Establishment and Jaffrin and Probstein at the Massachusetts Institute of Technology involved theoretical studies of shock-wave structure in single-ion plasmas as compared to the structure in neutral fluids [5, 6]. In those early works it was predicted that an electric field could be created at the shock front due to the large difference in mean free paths between protons and electrons [5, 6]. In 1993, Vidal *et al.* conducted kinetic simulations of shock-wave propagation in a single-ion-species plasma and compared the results to those from fluid simulations. This kinetic simulation predicted a thicker shock transition region than what was expected based on the fluid simulations, especially at high-Mach-number due to the presence of an electron preheating layer in the kinetic case [7].

In plasma, many mean free paths exist: the ion-ion mean free path, ion-electron mean free path, electron-electron mean free path, and any variations thereof if multiple ion species are present. The order of magnitude of each can vary greatly. For example, the ion-electron mean free path, λ_{ie} is related to the ion-ion mean free path, λ_{ii} by

$$\lambda_{ie} \equiv \lambda_{ii}\sqrt{m_i/m_e}. \tag{1.5}$$

Furthermore, the electrons, which are much less massive than ions, tend to be the main

conductor of heat, whereas viscous effects are determined by the heavier ions, especially at high-Mach-number [4]. This helps explain the results obtained by Vidal *et al.* [7], in which the electron preheating led to a thicker shock-front at high-Mach-number.

1.2 Shock-wave Induced Species Separation in Plasmas

1.2.1 Ion-diffusion in Inertial Confinement Fusion Fuels

One real world scenario that involves shock-wave propagation in multi-ion-species plasmas and is one of the main motivations for this body of work is in a method being explored in an attempt to obtain controlled nuclear fusion known as inertial confinement fusion, or ICF. Nuclear fusion, the process by which small nuclei fuse together to form larger nuclei and release large amounts of energy as a bi-product, has been an active area of research for well over half a century. Achieving large scale controlled nuclear fusion on Earth would essentially solve the globe's energy problems [8].

In ICF, a small, millimeter-scale diameter pellet of fusion fuel surrounded by a plastic ablator is rapidly compressed in about 10 to 20 ns [1], as shown in Figure 1.1. This compression occurs when either the fuel capsule is exposed directly to high-intensity, short-pulse laser energy from all sides (direct-drive ICF) or when laser energy hits a gold hohlraum (also shown in Figure 1.1) which emits X-rays that again hit the capsule on all sides (indirect-drive ICF). In either case, the energy imparted on the exterior of the capsule causes rapid ablation, sending the plastic ablator material shooting radially outward and resulting in a force in the opposite direction that drives the fuel pellet's compression.

The most promising fusion fuel is an equal mixture of two isotopes of hydrogen, deuterium (D) and Tritium (T), as this reaction, given by

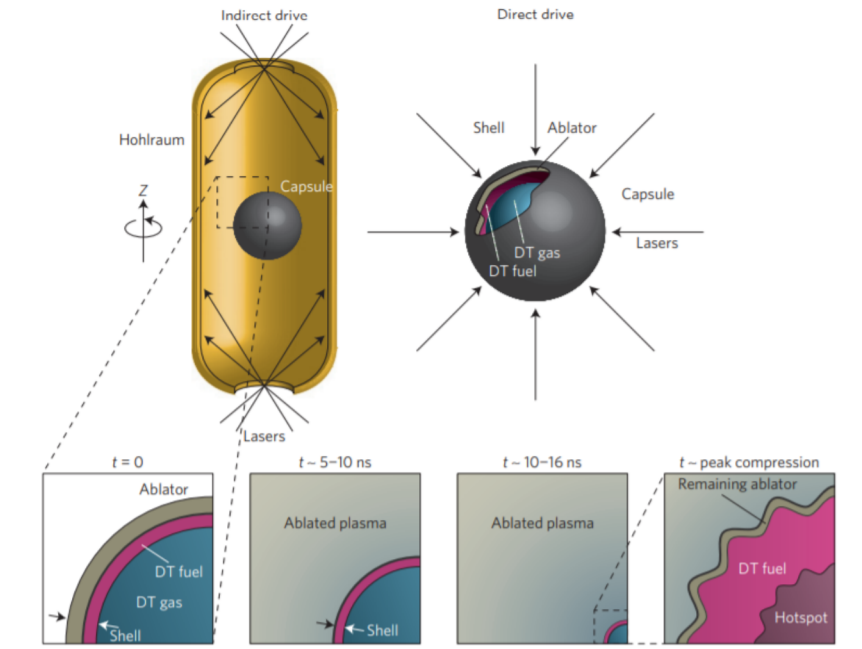

Figure 1.1: Indirect and direct dirve inertial confinement fusion capsule design and compression over time. Image from [1]

$$\mathrm{D} + \mathrm{T} \longrightarrow n(14.1\,\mathrm{MeV}) + {}^{4}\mathrm{He}(3.5\,\mathrm{MeV}) \tag{1.6}$$

has the largest fusion cross-section, producing an alpha particle and a neutron with 14.1 MeV of energy.

While this method remains a promising avenue for controlled fusion research, the neutron yield achieved in experiments has consistently fallen short of that which is predicted by simulation [9]. During an ICF implosion, the rapid ablation of the fuel's outer shell produces a shock-wave that precedes the compression, propagating towards the center of the fuel and then rebounding back outward. Separation of the DT fusion fuel caused by this shock has been suggested as one potential cause for the discrepancy [4, 9].

In 2008, large-scale self-generated electric fields on the order of $\geq$ GV/m were diagnosed in ICF experiments by Li *et al.* [10], and theoretical and computational work done by Amendt *et*

al. suggested that charge separation due to the high mobility of electrons could be the reason [11]. Theoretical work by Kagan and Tang showed how an electric field could drive species separation when ions of different charge-to-mass ratios were present [12]. Other computational studies conducted by Bellei *et al.* in the early 2010s provided support for the possibility that two shock waves could form in a uniformly mixed deuterium, tritium plasma [4, 9]. Kagan and Tang continued to investigate these complex phenomena, and in 2014 they suggested that gradients in temperature could also be a cause of separation in plasma shocks [13].

The result of this body of computational and analytical work is an enhanced understanding of shock-wave induced species separation in a plasma. Diffusion can be driven by gradients present in many parameters, including mass, pressure, temperature, and electrostatic potential. Considering all of these methods of ion diffusion, one can calculate the diffusive ion mass flux, $\mathbf{i}$, which is given for a multi-ion species plasma as [12]

$$\mathbf{i} = -\rho D\Big(\nabla c + k_p \nabla \log p_i + \frac{e k_E}{T_i}\nabla\Phi + k_T^{(i)}\nabla \log T_i + k_T^{(e)}\nabla \log T_e\Big) \tag{1.7}$$

where c is mass concentration, P_i is ion pressure, Φ is electrostatic potential, and T_i and T_e are the ion and electron temperatures, respectively.

Each k value is a dimensionless diffusion ratio that represents the relative strength of each diffusive mechanism. The baro-diffusion and electro-diffusion, k_p and k_E, respectively, are thermodynamic quantities, meaning they can be calculated given local thermodynamic variables and are not dependent on collisionality, whereas the thermo-diffusion ratio, k_T is a kinetic quantity, meaning it depends on a collisional model to calculate.

1.2.2 Shock-heating Effects on Nucleosynthesis in Type-II Supernovae

Another real-world scenario of a shock-wave propagating through a multi-ion-species plasma is a type-II supernova event. A supernova is the end-of-life explosion that occurs for some stars in which most of the star's mass is ejected. Type-II supernovae are distinguished from their type-I counterparts by the presence of hydrogen in their spectra as well as the process by which the explosion occurs. Type-II supernovae occur when a star collapses under the force of gravity, leading to an explosive rebound that sheds the star's outer layers [14].

The initial implosion of the star's core, a multi-ion-species plasma experiencing thermonuclear burn, produces a shock-wave that propagates outward through the imploding plasma. As this shock-wave travels through the core-material, it further drives thermonuclear burn and nucleosynthesis, ultimately producing iron, the element with the lowest binding energy, that then falls back towards the core. Depending on the mass and metallicity of the core, the expanding shock-wave may stop and reverse the collapse in some of the outer, lighter-ion-species core matter, resulting in the explosive shedding of those outer layers and leaving behind a hot neutron star. Other typically more massive stars, on the other hand, may result in a stagnated shock that does not produce an explosion, but instead may continue to collapse, forming a black hole [14, 15, 16].

This driving shock, propagating through the multiple-ion-species core has an effect on the progression of the event, but understanding precisely what conditions lead to each outcome is still an active area of research, and a fundamental understanding of shock-induced ion diffusion is necessary for continued progress. Furthermore, diagnosing a supernova event is very difficult, as there are no warning signs to tell us when one might occur, they are rare enough that so far the closest one to Earth whose remnant has been observed is still

over one-hundred light-years away [17], and the shock-front exists within the star's core, making diagnosis even more difficult. Developing a laboratory experiment where a shock-wave propagating through a multi-ion-species plasma can be controlled and much more easily diagnosed, however, allows us to better understand these complex phenomena on smaller scales and provides insight into the larger astrophysical events.

1.2.3 Experimental Studies of Species Separation

Following the work by Li *et al.* [10] that diagnosed large scale electric fields in ICF implosions, very little experimental work to measure ion separation induced by shock-wave propagation had been conducted until the mid-2010s. Recently, however, there have been a number of experiments that have shown direct evidence of this phenomena. One of these first experimental studies was done by Hsu *et al.* and Joshi *et al.* where plastic capsules filled with a mixture of deuterium and argon gas were imploded. Time-resolved X-ray spectroscopy data in those experiments showed direct evidence of changing argon atom fraction during the implosion [18, 19, 20]. In other experiments by Rinderknecht *et al.*, laser beams are used to drive an ablator that launches a shock-wave into a gas-filled tube containing a mixture of hydrogen and neon, resulting in the presence of two ion distributions. A cold background of hydrogen and singly-ionized Neon formed one distribution and a second distribution of hot hydrogen plasma was measured ahead of the shock-front [21]. Most recently, Byvank *et al.* performed experiments where they observed species separation at a shock front formed by the oblique merging of supersonic plasma-jets containing a mixture of argon and helium plasma in which the lighter helium plasma diffused further than the heavier argon plasma, and where the distance between their stopping lengths agreed roughly with theory [22].

This recent effort to measure ion diffusion and species separation in experiment has been

a great step forward for the community, as validation of the computational and analytical models of the various diffusion mechanisms has begun. This work, however, is by no means complete. With the exception of the work by Byvank *et al.* [22], the experiments conducted have still been on scales that are difficult to diagnose. The remainder of this body of work presents an experimental apparatus built and experimental campaigns conducted to produce shock-waves in multi-ion-species plasma where the thickness of the shock-structures is on the order of centimeters and exists on the order of microseconds. Conducting experiments on these scales can provide great insight into these mechanisms to add another level of understanding atop the work that has been done to date.

1.3 Remaining Content in this Dissertation

The remainder of this dissertation is broken up as follows. Chapter 2 discusses the design and development of a small, plasma-armature railgun and the experimental research platform necessary to accelerate high-Mach-number plasma-jets into vacuum. A full-suite of diagnostics implemented to characterize the resulting plasma-jets is also presented. Chapter 3 details the results from an experimental campaign to estimate plasma parameters of the accelerated jets at varying propagation distances in order to assess the suitability of the accelerator to study centimeter-scale plasma shock-structures. Chapter 4 presents a second experimental campaign where collisions between plasma-jets are induced, and the structures observed during the collisions are diagnosed. Chapter 5 concludes the work presented and provides potential avenues for future work or improvements.

Chapter 2

Experimental Apparatus

This chapter gives an overview of the experimental facility used for all the experiments discussed in Chapters 3 and 4 and details the design and construction of the plasma-armature railgun used to accelerate plasma jets.

2.1 Experimental Facility

All experiments took place in the Experimental Plasmas and Propulsion Laboratory (EPPL) at Virginia Tech's Center for Space Science and Engineering Research (Space@VT). The EPPL was developed concurrently with the development of the experimental apparatus discussed in Section 2.2; therefore, much of the facility's capabilities could be tailored specifically towards the needs of that apparatus. While this was the case, a deliberate effort was made to ensure that the EPPL's capabilities would satisfy not only the experiments discussed in this work but also a broad range of pulsed-power, spacecraft propulsion, and plasma science experiments, all while putting an emphasis on intuitive system operation, control and safety. This chapter details those capabilities at the time that this work was published.

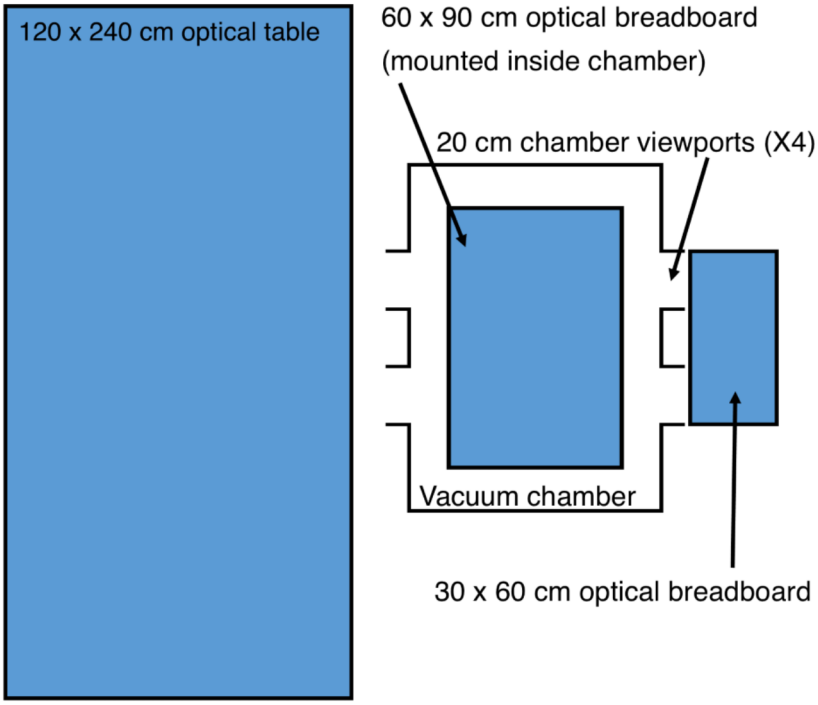

Figure 2.1: To-scale, top-view schematic of vacuum chamber laboratory showing center cross-section of cylindrical vacuum chamber and four view-ports at that cross-section and three optical tables and breadboards available for diagnostic setup

2.1.1 Vacuum Chamber and Diagnostic Access

The main test-bed in the EPPL is a 0.76 m^3, 1.2 m long cylindrical vacuum chamber. The chamber features eight 30 cm view-ports for diagnostic access and is sandwiched between an 8 x 4 ft optical table on one side and a 24 x 12 in optical breadboard on the other. In addition, a custom mount was created to place a second optical breadboard inside the vacuum chamber. All three of these diagnostic mounting tables are shown, as well as their position relative to the vacuum chamber in Figure 2.1. In addition to the four 30 cm view-ports for diagnostic access shown in Figure 2.1, there are four additional view-ports of identical size, two mounted on the top of the chamber and two on the bottom in the same relative configuration as the four shown.

To pump down the chamber, an oil-sealed rotary vane rough pump first brings the pressure in the chamber down to $\sim 50\,\mathrm{mTorr}$ in 60 minutes. Then, a cryopump takes the pressure inside the chamber down to an ultimate pressure of $\sim 200\,\mathrm{nTorr}$.

2.1.2 Data Acquisition and Control Systems

The primary data acquisition unit for the laboratory is an 8-channel National Instruments PXIe 5105 oscilloscope with 60 MHz bandwidth, 60 MSa/s sampling rate, and 12-bit resolution. Two additional Keysight Technologies oscilloscopes, one a 4-channel unit with 200 MHz bandwidth, 2 GSa/s sampling rate, and 8-bit resolution and the other a 2-channel unit with 100 MHz bandwidth, 2 GSa/s sampling rate, and 8-bit resolution acquisition, are also available.

The nature of pulsed-power experiments often means that precise timing of different aspects of an experiment is essential. In the EPPL this is done using a Stanford Research Systems DG645 digital delay generator with 4 channels that deliver 5V TTL pulses with $< 25\,\mathrm{ps}$ jitter.

The National Instruments oscilloscope and digital delay generator as well as many auxiliary systems are all controlled using a single program written in National Instrument's LabVIEW. Where possible, laboratory systems are controlled via optical fibers to protect users and equipment from any high-voltage present in an experiment and reduce electromagnetic interference (EMI) often present in pulsed-power systems. Data acquisition and control electronics are all housed in a Hammond RF enclosure to further protect the electronics and reduce EMI.

2.1.3 Safety

In any lab setting where high-voltage is a necessary part of experimentation, putting in place a series of safety measures is essential to protecting apparatus operators. To this end, a series of high-voltage interlocks were put in place. First, a series of 3 relays were connected between the two external interlock pins on the back of the high-voltage power supply, a Spellman SL600 which provides voltages up to 20 kA. These three relays include a reed switch connected to the lab door that is only closed if the door itself is also closed, a second relay controlled through LabVIEW and therefore easily accessible to an apparatus operator, and finally a physical red button switch located on top of the rack where the high-voltage power supply is located that can be easily pressed by the operator of the high-voltage supply. If any of these three relays are triggered, the supply of high-voltage is immediately cut off and the operator cannot operate the power supply until all three relays are returned to their normally closed position. In addition, since a safety requirement for using the high-voltage supply is that only trained operators may be present in the room when the high-voltage supply is on, a red light was mounted outside of the lab door that turns on whenever the high-voltage supply is on, warning any other researchers not to enter the room at that time.

2.2 Linear Plasma-armature Railgun

In order to utilize the capabilities of the facility discussed in Section 2.1 for scientific exploration and academic research, a small, linear plasma-armature railgun was designed as the foremost experimental apparatus for use in the EPPL facility. Simply stated, the railgun was chosen as an inexpensive, reliable means of producing and accelerating jets of plasma to high-Mach-number within the vacuum chamber, allowing for the study of a wide range of plasma physics topics. This chapter details the design and operation of that accelerator as

well as the reasons for which design decisions were made.

2.2.1 Railgun Design and Construction

Design of the plasma-armature railgun was guided by previous work done on plasma-armatures [23, 24] and by early versions of the railguns used in the Plasma Liner Experiment [25, 26, 27]. In addition, a few design requirements and performance specifications were considered during the design process. First, given the size of the facility, the device itself had to be smaller than most plasma railguns. Another main consideration in designing the accelerator was to set collision parameters in the resultant jets such that any shock structures present in a jet collision would be on the scale of centimeters, a spatial scale conducive to more easily probing and examining jet parameters before, within, and after a shock wave. Based on previous studies of merging supersonic plasma jets [25, 28, 29, 30], the gun would need to produce jets with a velocity between 10 and 20 km/s, electron number densities of at least $10^{13}\,\mathrm{cm}^{-3}$, and ion temperatures below 3 eV. Finally, the gun was designed to be modular, meaning that as many components as possible could be removed and replaced easily, allowing for the easy change of materials and geometries of the main parts of the accelerator or the replacement of components if one wore down or was damaged.

The final design for the accelerator, a series of computer renderings of which are shown in Figure 2.2, consists of two 102 mm rail electrodes sandwiched between two ceramic insulators that set the distance between the two electrodes and give the accelerator a rectangular bore cross-section that is 3.2 mm tall and 5 mm wide. Each electrode is screwed into place and compressed against a main bus bar and bus bar extension piece. The two main bus bar pieces are glued in place within a rear plastic housing component using a vacuum compatible and sealing epoxy called Torr Seal. The assembled rear part of the gun, including the two

electrodes, ceramic insulators, bus bar extensions, rear plastic housing, and two main bus bars, slides into a second front plastic housing piece. The seam between these two housing pieces are sealed with a single fluorocarbon rubber O-ring that is compressed when the two pieces slide together and two stainless steel screws pass through the rear housing piece and screw into tapped holes in the front housing component. This entire assembly is screwed in place using five long stainless steel screws that extend through both plastic body pieces into blind tapped holes in an ISO-200 vacuum flange. The muzzle of the railgun extends through a rectangular-shaped hole drilled into the center of the flange. A second O-ring is used to seal the railgun to this flange.

Since only the two main bus bars and rear plastic housing part are permanently sealed together, the rest of the gun can be easily disassembled. As a result, as long as the electrode assembly (rail electrodes, ceramic insulators, and bus bar extensions) does not change, the individual components within the assembly can be altered in any way. This meets one of the fundamental requirements for the gun design, allowing for the testing of different geometries and component materials without the added expense and time required to machine an entire accelerator from scratch.

In fabricating the accelerator, all the pieces originally machined for the railgun were used throughout the experiments discussed in the remainder of this work; therefore, the geometry did not change from what is shown in Figure 2.2 and has been presented in this chapter. The two housing pieces were machined from a PEEK (polyether-ether-ketone) plastic which was chosen for its high temperature resistance, strength, and rigidity as compared to other plastics. The bus bars were machined from a chromium-copper alloy which has the high electrical-conductivity of pure copper but is much easier to machine. The insulators were machined from an aluminum-nitride and boron-nitride mixture, a ceramic that offers high strength and very low porosity, making it great for vacuum applications. In addition, this

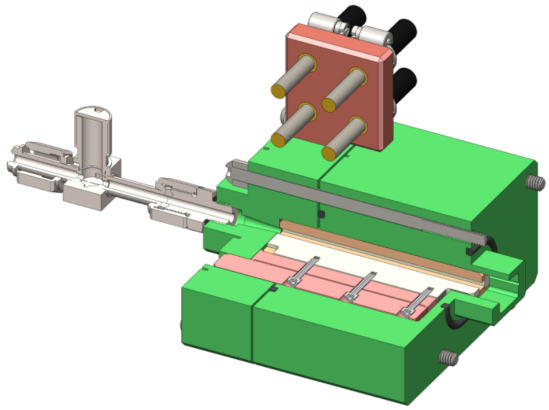

(a) Quarter-section view

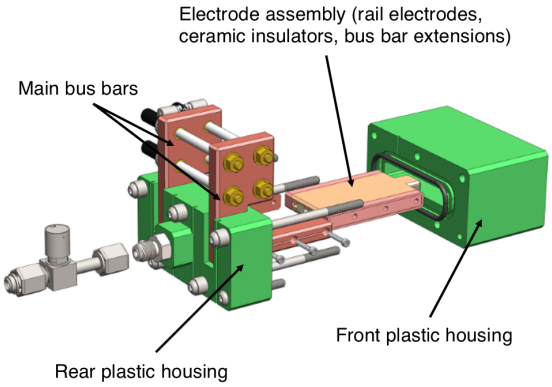

(b) Exploded view showing assembly process

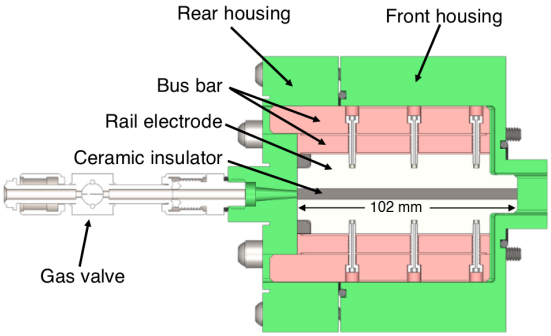

(c) Top-view cross-section schematic

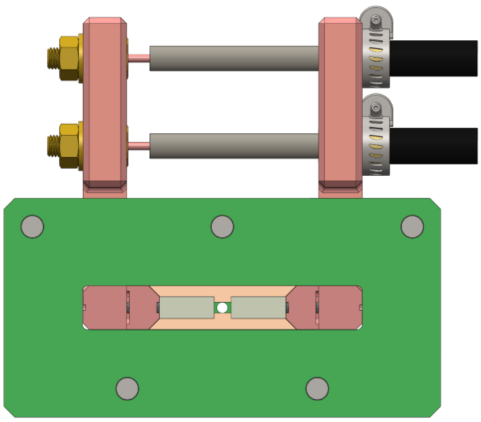

(d) Front-view cross-section schematic

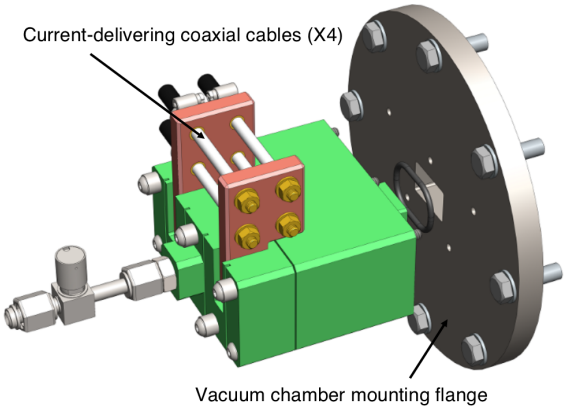

(e) Exploded view showing how railgun is mounted to a custom vacuum chamber flange

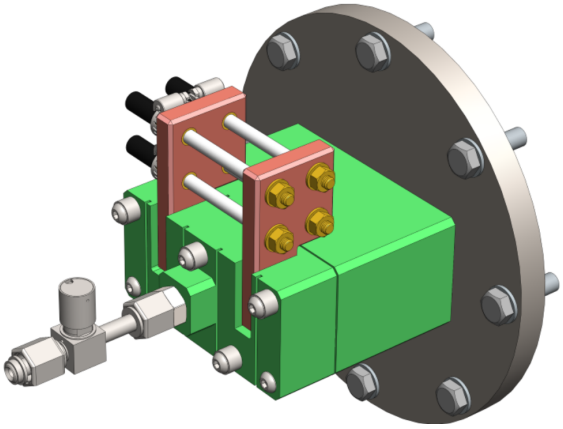

(f) Fully assembled railgun

Figure 2.2: Three-dimensional renderings of the accelerator

ceramic has excellent machinability, allowing for the inclusion of detailed and thin geometric features that would hold up well to the extended and frequent use of the accelerator. Finally, two sets of rail electrodes were machined, one from a 55 % tungsten, 45 % copper alloy and the other from a 75 % tungsten, 25 % copper alloy. A tungsten-copper alloy was chosen for the excellent electrical properties of copper and the great strength and erosion-resistant properties of tungsten.

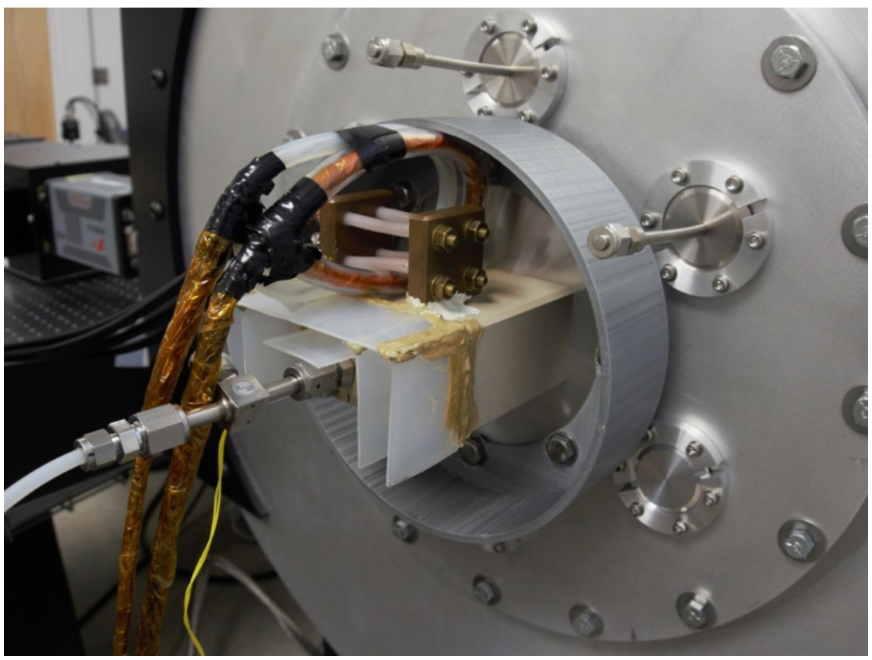

Figure 2.3: Railgun mounted to vacuum chamber door

Figure 2.3 shows the assembled railgun attached to the vacuum chamber's door. The accelerator is attached such that the center axis of the chamber is collinear with the center of the bore of the gun. This axis, which is defined as the bore-sight-, or z-, axis of the railgun will be used throughout this work to establish position within the chamber relative to the accelerator, begins at the muzzle of the gun at $z = 0$ and extends with positive value into the chamber.

2.2.2 Gas Valve

The railgun is gas-fed with pure argon via a stainless steel Parker Series 99 fast-actuated solenoid valve that attaches to the back of the gun through an adapter that screws into a tapped hole in the railgun rear housing component and seals with a small fluorocarbon O-ring. A tapered hole which can be seen in Figures 2.2a and 2.2c directs gas into the bore of the gun. An optical fiber-triggered LCR driver circuit developed in-house supplies a single slightly under-damped current pulse, shown in Figure 2.4, to the valve with $\approx 2\,\mathrm{ms}$ pulse width. This driving current pulse opens and closes the poppet within the solenoid valve quickly, allowing only a small amount of gas to enter the breech of the gun.

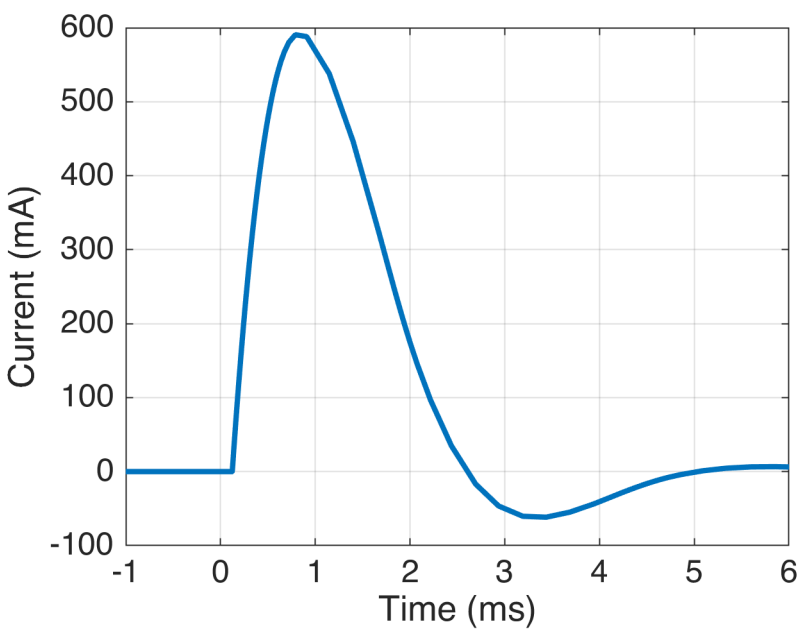

Figure 2.4: Current pulse delivered to gas valve via custom LCR driver circuit

Pressure rise tests were conducted to evaluate the consistency of the puff valve operation and determine the amount of argon gas being puffed into the gun when the line was pressurized to 350 and 700 kPa, the two values of line-pressure used throughout this work. In this test, the railgun and solenoid valve were mounted to the chamber just as they would be during normal

railgun operation. The vacuum chamber was pumped down and tests were conducted by recording the pressure within the chamber just before and just after the valve was triggered. Using this method with 350 kPa pressure in the valve's upstream line, it was inferred that 5.7 ± 0.10 mg of gas was injected into the breech of the gun and with 700 kPa, 11.1 ± 0.94 mg of gas was injected.

2.2.3 Pulse-forming Network

Power is delivered to the railgun by an LC pulse-forming network (PFN) of high-voltage Sylac-style capacitors. A PFN is a method of combining capacitors and inductors such that when the discharge current pulse from each capacitor is summed, the result is a single square wave pulse of desired width and peak current.

The pulse forming network for the railgun was designed such that the quarter period of the discharge current pulse would roughly match the plasma's time-of-flight between the railgun's breech and muzzle. For this accelerator, a pulse width of about 10 to 15 μs was desired. To achieve this discharge, a circuitry modeling software was used to tune the capacitance and inductance characteristics of the pulse-forming network. Available for use in the PFN were a number of 1.3 μF and 100 μF capacitors. Inductance was tuned by altering the geometry of the bus-work used for the electrical connection between all the capacitors.

The final design, shown in Figure 2.5, consists of a parallel connection between six, 1.3 μF capacitors connected in parallel and two, 100 μF capacitors connected in series, for an equivalent capacitance of $\approx 58\,\mu$F. The custom designed bus-work was water-jet cut from 6061-aluminum, chosen for its high electrical conductivity and machinability. Multiple sheets of polypropylene (PPE) totalling 1/8" thick act as the dielectric barrier between the hot and ground plates of the PFN. The capacitor bank can be charged up to a maximum of 22 kV,

limited by the voltage rating of the two 100 μF capacitors.

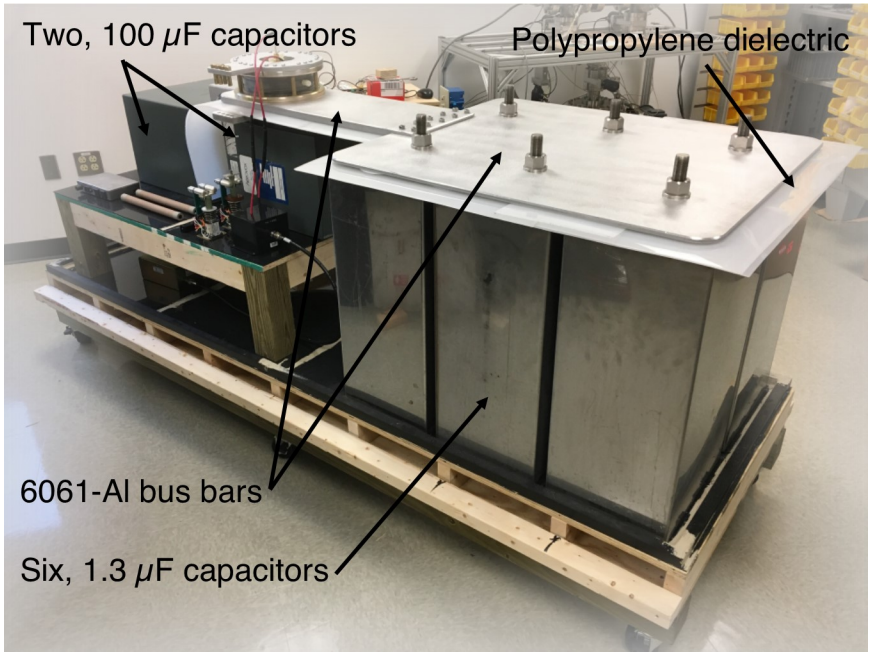

(a) Partially assembled PFN showing capacitors, bus-work, and dielectric material

(b) Fully assembled PFN with polycarbonate enclosure and discharge stick in place

Figure 2.5: Final design for the railgun's pulse-forming network (PFN)

The PFN sits on a wooden cart with six caster wheels that is just skinny enough to fit

through a standard doorway. The top of the cart is covered in a layer of nylon plastic and a series of nylon rods with a 2.5×2.5 cm square cross section are mounted around the perimeter of the cart to form a lip. This nylon, which is chemically resistant to the mineral oil that fills the capacitors, protects the wood of the cart and the floor from damage in the event of any oil leakage. A polycarbonate (PC) enclosure, shown in Figure 2.5b, with a removable lid and latching access panel on one side of the enclosure for accessibility sits on top of the cart so that no operator can accidentally get close enough to the capacitors when charged to receive an electric shock.

2.3 Diagnostics

2.3.1 Rogowski Coil

A Rogowski coil is a toroid-shaped magnetic field diagnostic used to estimate the magnitude and period of high-speed current pulses. When wrapped around a conductor, as shown in Figure 2.6, a signal is induced in the Rogowski coil that is proportional to the rate-of-change of the current flowing through that conductor. The coil is constructed by forming a solenoid and then bending the solenoid such that the ends nearly meet to form a toroid with a return wire traveling through the center, also shown in Figure 2.6.

The coil is a simple application of two of Maxwell's equations. The first, the Maxwell-Ampère law, can be used to describe the magnetic field, $\mathbf{B}$, produced parallel to the axis of the torus due to the current, i, flowing through the center of the toroid as

$$\oint_C \mathbf{B} \cdot d\mathbf{l} = \mu_0 i \tag{2.1}$$

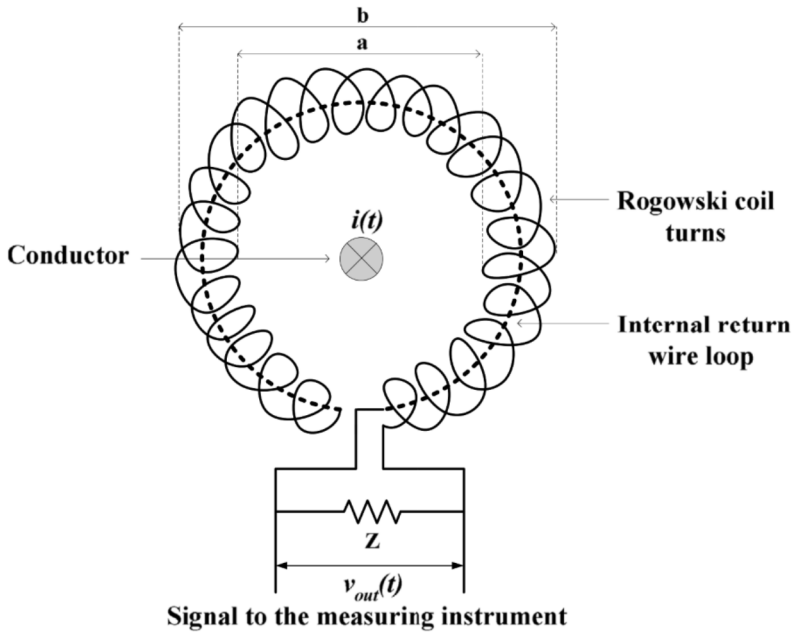

Figure 2.6: Rogowski coil schematic, image from [2]

where $\mathbf{l}$ is the circumference of the toroid. Then, Faraday's law describes the electric field, and subsequent current, induced in the Rogowski coil by the changing flux of magnetic field flowing perpendicular to the coil's windings. In integral form, Faraday's law is given by

$$\oint_C \mathbf{E} \cdot d\mathbf{l} = -\int_S \dot{\mathbf{B}} \cdot d\mathbf{s} \tag{2.2}$$

where S is the surface enclosed by loop C. Finally, assuming constant cross-section area, A, for each winding and an even spacing between every winding, the voltage induced in the Rogowski coil, $u(t)$ is given by

$$u(t) = \frac{A}{s}\mu_0 \frac{d}{dt} i(t) \tag{2.3}$$

where s is the number of windings per unit length in the coil [2]. The current flowing through the wire of interest can then be found by integrating the voltage signal picked up by the coil, a process which is often done using an analog integration circuit but which was found to be easier and more convenient to do digitally.

There are a number of great properties of a Rogowski coil. First, the coil picks up a signal due to current flowing through any part of the inside of the toroid, independent of distribution; therefore, precise placement of the coil around the current-carrying body is unnecessary, making setup and placement for experiment simple. Also, by altering the number of windings, or turns, in the solenoid, the spacing between each turn, and the cross-sectional area of each turn, the signal amplitude induced in the Rogowski coil can be controlled based on the expected rate of change of current to be measured. Finally, as with all magnetic diagnostics, the inherent standoff between the current-carrying body and the diagnostic provides an added layer of safety, especially for the pulsed-power experiments for which these diagnostics are used, where high-voltage and large-magnitude currents are present.

Figure 2.7 shows the coil fabricated in-house for use with the railgun. The coil was designed such that the signal induced in the coil would be around 5-10 V based on the expected current pulse produced by the railgun's PFN. The coil wraps around the four current-carrying coaxial cables in between the ground and hot bus bars that extend from the railgun's body.

2.3.2 Two-chord Interferometer

A two-chord, Mach-Zehnder, heterodyne, quadrature, and open-air interferometer was designed and used to infer electron number densities of the plasma jets accelerated with the railgun. An interferometer is a laser diagnostic that measures index of refraction of a medium by passing a coherent light source through that medium and comparing the resulting signal

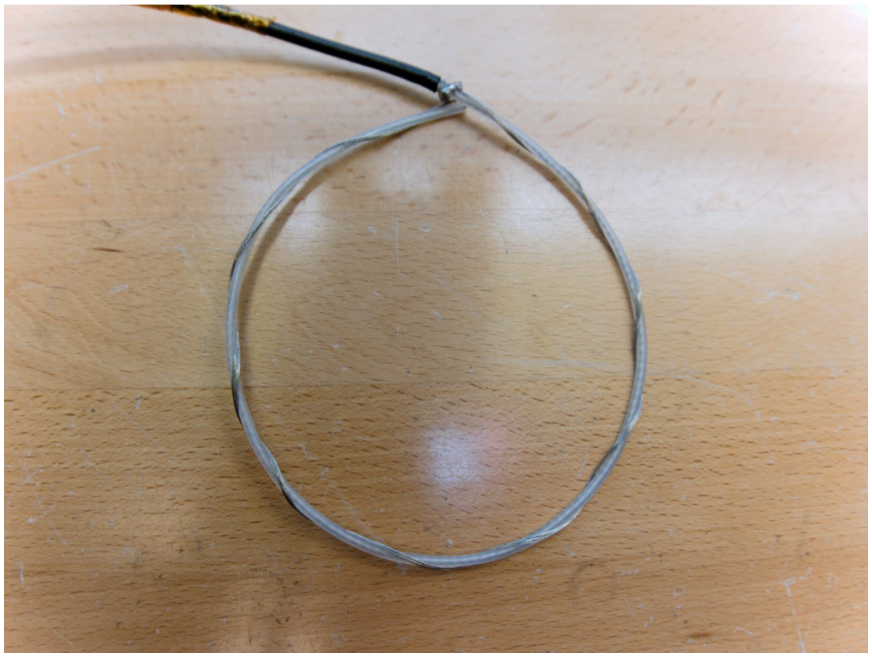

(a) Rogowski coil without dielectric covering

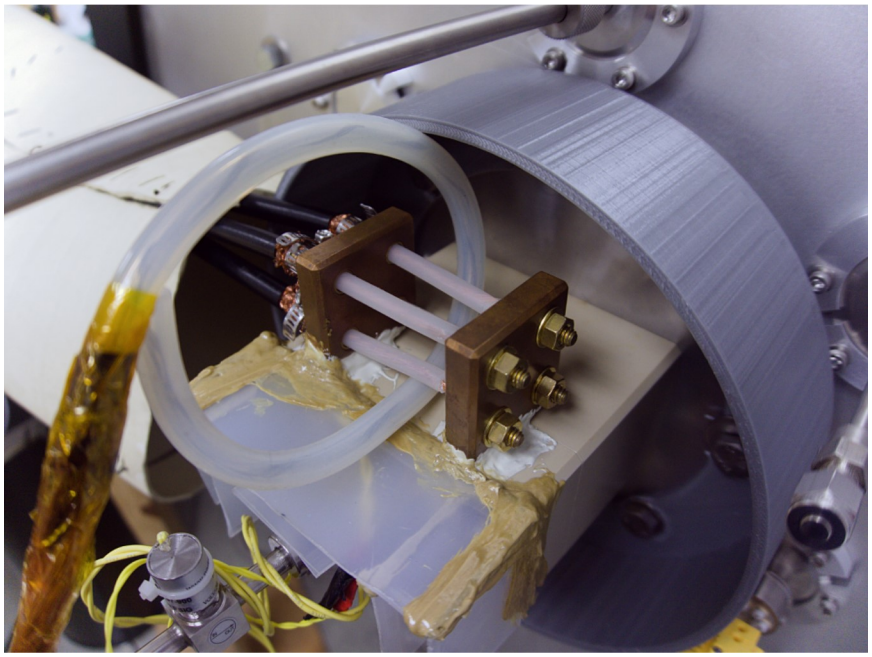

(b) Rogowski coil mounted around current-delivering coaxial cable inner electrodes in testing configuration

Figure 2.7: Rogowski coil images

with that of another, otherwise identical beam, that does not pass through the medium. Figure 2.8 is a simple schematic showing this principle as it would be used to measure index of refraction of a plasma. The schematic shows optics in the Mach-Zehnder configuration, where a different beamsplitter is used for splitting and recombining the beam, as opposed to the Michelson configuration, which uses just one beamsplitter.

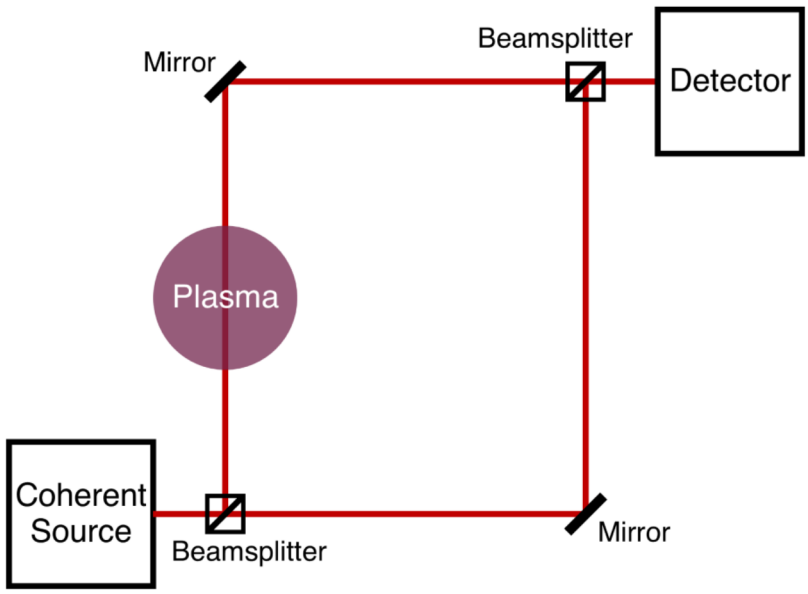

Figure 2.8: Basic Mach-Zehnder Interferometer Schematic

The beam that travels through the plasma, called the probe beam, undergoes a phase shift relative to the second beam, called the reference beam, due to the difference in index of refraction of the medium that the probe beam passed through as compared to that of the reference beam, resulting in an interference pattern when the two beams are recombined. In a plasma, this phase shift is due mainly to free electrons. The index of refraction, N, due to free electrons in a plasma is defined as

$$N = \frac{ck}{\omega} = \sqrt{1 - \frac{n_e e^2}{\epsilon_0 m_e \omega^2}} \tag{2.4}$$

where n_e is the electron number density of the plasma and ω is the frequency of the laser-light passing through the plasma. Since the frequency of the laser-light once a laser is chosen is a known constant, index of refraction is solely dependent of number density.

The change in phase shift, $\Delta\phi_e$ due to free electrons is given by

$$\Delta\phi_e = \frac{-e^2\lambda}{4\pi\epsilon_0 m_e c^2} \int n_e d\ell \tag{2.5}$$

where $d\ell$ is the length of plasma the probe beam passes through.

Our interferometer was designed as an open-air, quadrature, and heterodyne system loosely based on an interferometer designed as a diagnostic for the Plasma Liner Experiment [31]. An open-air interferometer simply refers to a system where the laser-light travels through air and is tuned and directed using mirrors for its entire path length, as opposed to a fiber-coupled device, which while more expensive is typically easier to work with, as it uses optical fibers to direct the laser-light for as much of the beam path as possible. In a heterodyne interferometer, when the coherent light source is split into a probe and reference beam, the reference beam's frequency is up-shifted by some known and constant value. This is done using a device called an acousto-optic modulator (AOM). In this setup, the coherent light source is a Model 1122 P Lumentum 2 mW, 632 nm linearly polarized HeNe laser with long coherence length. The AOM used in this setup is an IntraAction ATM-801A1 powered by an IntraAction ME-801 RF driver that shifts the reference beam by 80 MHz. After the

two beams recombine, they are captured using a 150 MHz bandwidth Thorlabs PDA10A photodetector. From there, the signal passes through an MCV Microwave BCL80-40-A1 bandpass filter centered on 80 MHz to remove high-frequency noise and signal components and low frequency or constant DC components. The signal is then processed using an IQ demodulator (Pulsar IDO-04-412) which uses a reference signal from the AOM's RF driver to split the interference signal and shift one of the resultant signals by a quarter-phase. This signal processing technique, in which a sinusoidal signal is broken up into an in-phase component, $S(t)_I$, and a component that is $\pi/2$ out of phase, also called the quadrature component, $S(t)_Q$, is a powerful tool, as it removes any sinusoidal wave amplitude dependence from the final signal. Finally, before reaching the data acquisition unit, the two output signals from the IQ demodulator each pass through a 6 MHz lowpass filter to remove the 80 MHz carrier frequency that had been applied by the AOM. Figure 2.9 details this setup for one chord of the interferometer. The second chord uses duplicates of all the electronics shown in the figure with the only exception being that the same laser and AOM are used for both chords. A beamsplitter is used on each of the beams that exit the AOM, creating two probe beams and two reference beams.

The phase shift due to the plasma can be calculated from the two digitized signals as

$$\tan\phi(t) = \frac{S(t)_Q}{S(t)_I}. \tag{2.6}$$

2.3.3 Fast Photography

In order to visualize plasma-jets moving at velocities of many kilometers per second with any temporal resolution, a standard camera will not suffice. The shutter in these cameras,

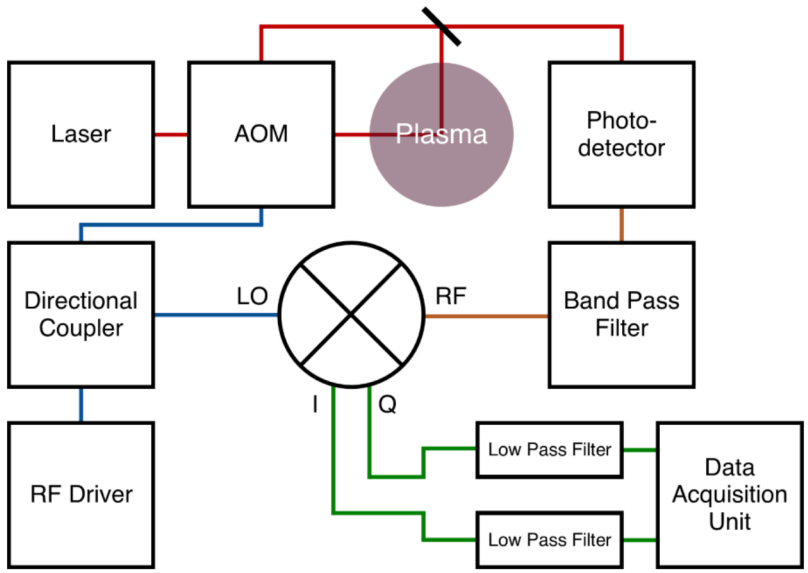

Figure 2.9: Optics and electronics layout for a single chord of the interferometer

the mechanical device that physically blocks or exposes the camera's sensor to light, simply cannot move fast enough to capture a "freeze-frame" image of an object moving at that velocity. To overcome the limitations associated with moving mechanical components, a camera with an electronic shutter must be employed.

One device with this ability used to take low gate time images of the accelerated plasma-jets is an intensified charge-coupled device (ICCD), shown in Figure 2.10. Incident light first hits a negatively charged electrode called a photocathode that emits an electron when hit by a photon. These emitted electrons then travel through a microchannel plate, an array of tubes with a strong electric field applied from one end of each tube to the other, that multiplies each electron that passes through the plate into a cloud of electrons. Finally, these electrons hit a phosphor screen that works much like the photocathode but in reverse, emitting a photon for each electron that hits the phosphor, before hitting the camera's sensor. Through these series of devices, the number of photons hitting the sensor is greatly multiplied, but the relative

location of each photon is maintained, producing an amplified version of the same incident image on the camera sensor. Since there are no moving components in the intensifier design, very low sensor exposure times, or gate times, are possible by simply cutting off power to each component. In addition, the amount of intensification can be easily controlled, by changing the strength of the electric field across the microchannel plate.

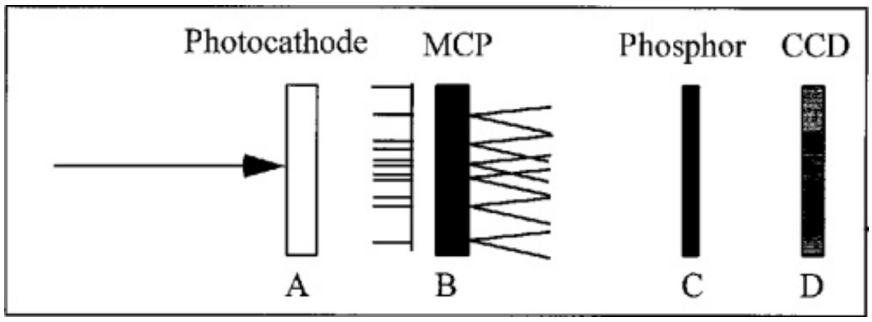

Figure 2.10: ICCD schematic, image from [3]

The camera used to image the plasma jets is a Princeton Instruments PIMAX 4 1024i ICCD with a 1024 x 1024 pixel array square sensor. The 16-bit PIMAX camera is equipped with a broad-spectrum photocathode (200-900 nm) and is capable of taking images with gate times as low as 3 ns.

During experimentation, the camera mounts to the top of the vacuum chamber to a custom designed mount constructed from 80/20 strut material and featuring four degree-of-freedom motion to give visual access through either of the vacuum chamber viewports atop the chamber. The mount and the chamber are shown in Figure 2.11.

2.3.4 High-resolution Spectroscopy

In its simplest form, a spectrometer is an instrument that separates light based on wavelength. A common spectrometer is the Czerny-Turner spectrograph, shown in Figure 2.12a. In this configuration, light that enters the spectrometer through the entrance slit is first

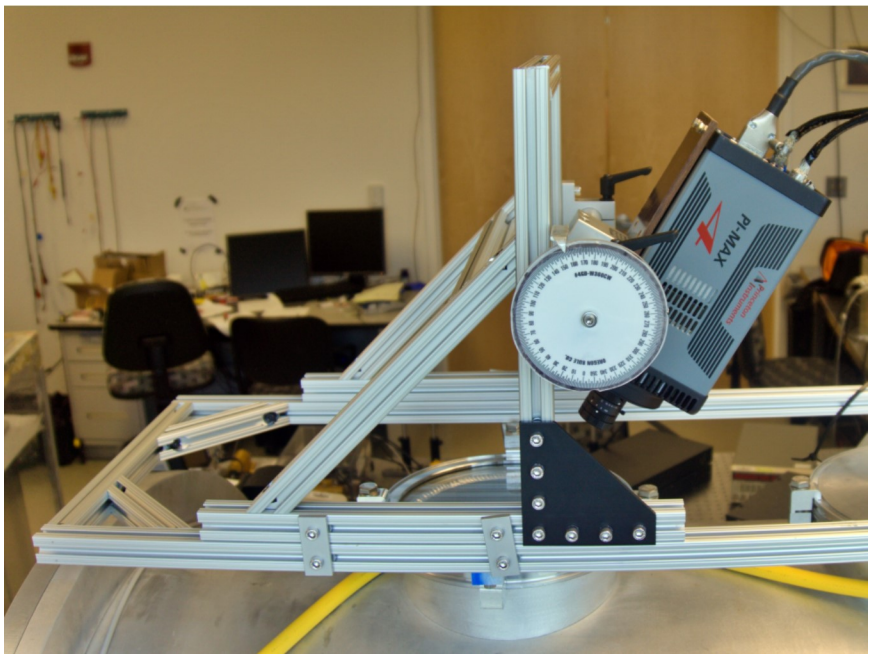

Figure 2.11: PIMAX 4 ICCD camera mounted to custom 80/20 structure atop vacuum chamber

collimated using a plano-concave lens. This collimated light hits the diffraction grating, a reflective surface with grooves whose spacing determines at what angle light of a specific wavelength will be reflected, as shown in Figure 2.12b. This grating separates light spatially based on wavelength. Finally, the separated light hits another plano-concave mirror that focuses the light onto the focal plane of the spectrometer.

The spectrometer used is an Acton Standard Series SP-2758, 750 mm focal length high-resolution imaging spectrograph. The spectrometer was used for plasma-emission survey spectroscopy, where light emitted from the plasma is captured to help determine which ion species and ionization stages exist within the plasma. The detector used with the spectrometer is the same image-intensified CCD camera that was discussed in Section 2.3.3.

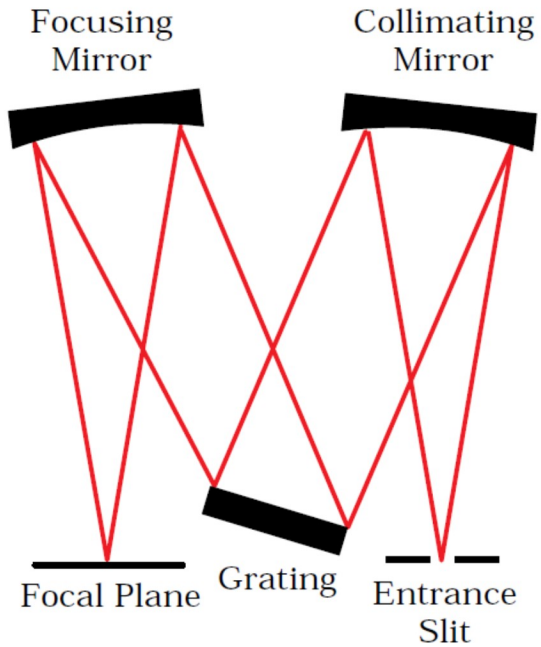

(a) Czerny-Turner spectrometer schematic, image from [32]

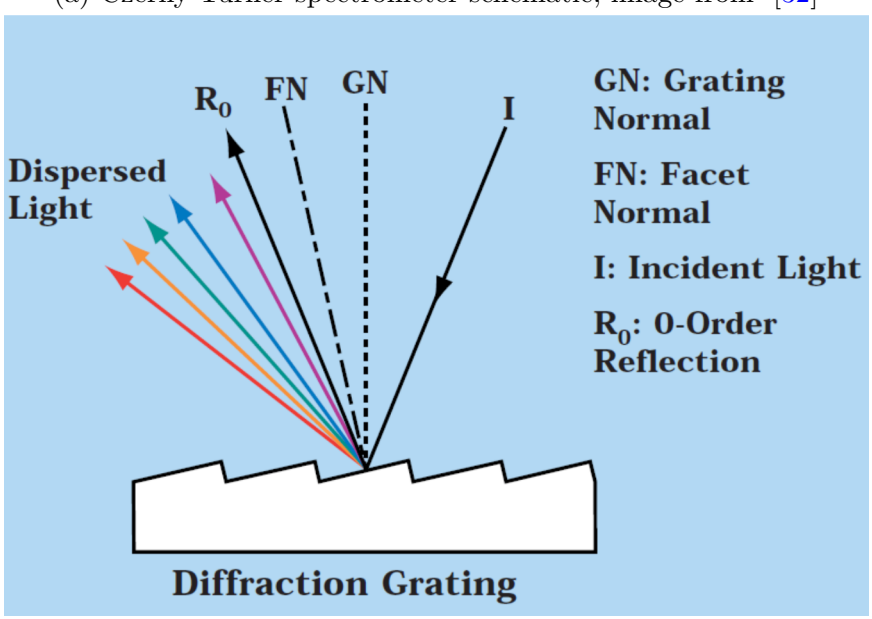

(b) Diffraction grating schematic, image from [33]

Figure 2.12: Spectrometer schematics

Chapter 3

Unobstructed Single-Jet Propagation Experiments

The first set of experiments performed using the linear plasma-armature railgun and suite of diagnostics built to probe the resultant plasma jets was a two-stage campaign. The goal of the first stage was to find the ideal gun settings to maximize gun performance. Upon finding this setting, experiments were performed to characterize the plasma-jets at multiple locations within the chamber at different distances away from the muzzle of the gun. This campaign acts as a foundation for the work presented in Chapter 4 and for any future work done using the railgun.

3.1 Experimental Setup

The 55 % tungsten, 45 % copper alloy electrodes were used for all the results presented in this chapter. Pure argon gas was puffed into the gun in all experiments as well. The plasma-jet's path within the chamber was unobstructed except for the optical breadboard mounted inside the chamber at 18 cm below the bore-sight axis. This breadboard was used for interferometer optics, allowing for precise control of where the interferometer probe beam intersected the bore-sight axis of the gun while keeping the probe beam perpendicular to that axis.

Figure 3.1 shows a schematic of the diagnostic setup used for the experiments presented

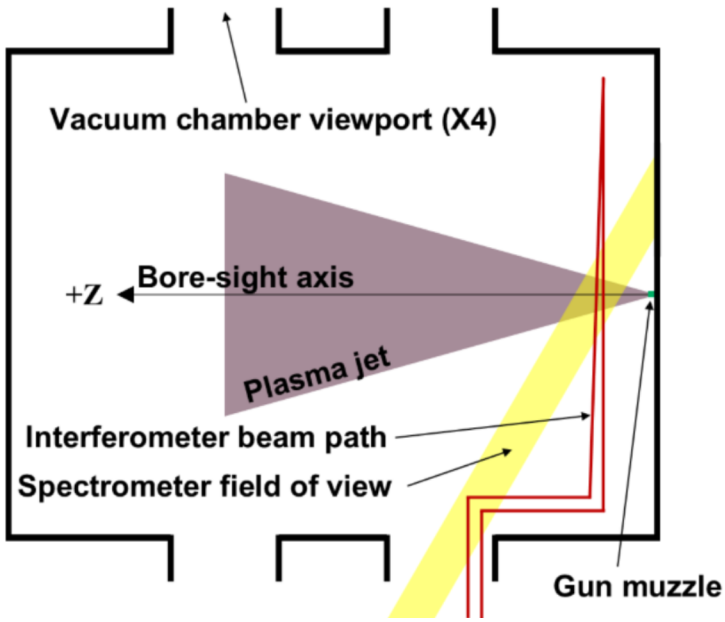

Figure 3.1: To-scale top-view cross-section schematic of vacuum chamber at the chamber's center axis showing diagnostic viewing chords and approximate plasma-jet trajectory.

in this chapter. The interferometer was used in a double-pass configuration, in which the probe beam passed through the plasma twice, the first was perpendicular to the bore-sight axis and the second was at a very small angle relative to the first such that both chords intersected the bore-sight axis at essentially the same distance from the gun. Also, only a single chord version of the interferometer discussed in Section 2.3.2 was used for all the results presented in this chapter. These tests were done before upgrading the interferometer to the two-chord version discussed previously. The functionality and parts used in this version of the interferometer are all the same as discussed in Section 2.3.2. An optical system with a 7.6 cm objective lens was designed and built for use with the high-resolution spectrometer and collected a 7.6 cm diameter beam of collimated light and projected it onto the entrance slit of the spectrometer.

3.2 Finding Ideal Gun Settings

Despite all materials and geometries of the gun being set for all the experiments discussed in this chapter, there still remain several gun parameters that can be set to tune the gun's performance. This section discusses the experiments conducted to find the set of these parameters that would maximize gun performance. The main metrics used to assess gun performance were interferometer-inferred line-integrated number density and the presence of singly-ionized argon as compared to other impurity species in the plasma, estimated by comparing the intensity of spectral lines of each species within the plasma.

The first and possibly most important gun parameter to set was the timing delay between when the capacitor bank discharge was initiated and when the gas-puff valve (GPV) was triggered. Because the poppet inside the solenoid valve blocking the flow of gas is $\approx 10\,\mathrm{cm}$ upstream of the breech of the gun, a delay needs to be applied between the gas valve's actuation and the capacitor bank discharge to allow time for the gas to travel to the breech of the gun. Ideally, peak electric current would flow through the gun's electrodes right as the densest argon gas reached the back of the accelerator's rails. The hope in this case is that the energy from the capacitor bank goes to ionizing and accelerating mainly the argon gas as opposed to impurity material ablated from the gun housing, ceramic insulator, or electrodes. If timing was off such that the electric potential was applied either before the gas reached the breech of the gun or after the densest gas left the bore of the gun, then the expectation would be that a higher proportion of impurity species would compose the resultant plasma-jets. With the PFN trigger time defined as $t = 0$, the gas puff valve trigger time was varied first at $300\,\mu$s intervals between -300 and $-2100\,\mu$s and then at $100\,\mu$s intervals between -1600 and $-2000\,\mu$s based on the results of the first scan.

Another gun setting to tune was the pressure of argon gas puffed into the railgun. Limited

by the maximum pressure rating of the solenoid valve, the line pressure of the gas was set to either 350 or 700 kPa. Finally, the PFN was charged to either 10 or 15 kV. Stored energy in a capacitor, E, is given by

$$E = \frac{1}{2} C_{eq} V^2 \tag{3.1}$$

where C_{eq} is the equivalent capacitance of the PFN and V is the voltage the bank is charged to. Recall, as discussed in 2.2.3, that the PFN has an equivalent capacitance equal to $\approx 58\,\mu$F. At 10 and 15 kV, this corresponds to a total stored energy of 2.9 and 6.5 kJ, respectively. While this increase in stored energy could aid gun performance initially, it also poses a concern that the rate at which the plasma-facing gun components erode and wear down could increase.

3.2.1 Finding Ideal Gas Valve Timing

Finding the ideal GPV timing relative to the PFN discharge was the first objective of this experimental campaign. Before running the railgun with a range of GPV timings, however, the current pulse across the rails, estimated from data collected with the Rogowski coil, was compared for the 10 and 15 kV PFN charge voltage cases to a tuned circuitry model, shown in Figure 3.2. The PFN delivers a $\approx 30\,\mu$s period under-damped current pulse with a peak amplitude of 90 and 135 kA for the two cases, respectively. This PFN performance is more under-damped than was anticipated when the PFN was designed, although the initial pulse width, $\approx 15\,\mu$s, matches the pulse-width desired (see Sec. 2.2.3). This discrepancy most likely due to the high-inductance of the $100\,\mu$F capacitors, the only parameter that was unknown when the PFN was first designed. The modeled current pulse shown in Fig 3.2

was the result of tuning that inductance such that the period of the simulated current pulse would match the observed pulse shape. As predicted by RLC circuit dynamics, increasing the voltage only affects the current amplitude, and does not affect the period of the current pulse. Since this is the case, it can be assumed that the ideal GPV delay time will be the same for both PFN charge voltage cases.

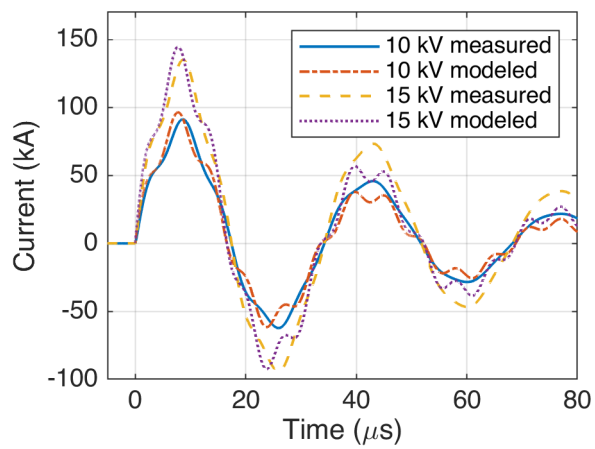

Figure 3.2: Mean PFN current pulse inferred from Rogowski coil data for 10 and 15 kV charge voltage cases as compared to modeled current.

To find the ideal GPV timing, a scan of delay times between the PFN discharge and puff valve trigger time was performed and plasma-jet parameters were compared. Since $t = 0$ is defined as the time at which the PFN was triggered for all experiments in this work, puff valve trigger time is always negative, representing how long before the PFN discharge began the solenoid valve was triggered. To assess gun performance, the interferometer probe beam and spectrometer optics were positioned to intersect the bore-sight axis of the gun at $Z = 10\,\text{cm}$. Figure 3.3a shows the line-integrated density measured using the interferometer for the low-resolution scan of timings. Based on this scan, it was clear that the high-pressure front of argon gas reached the breech of the gun at some point at least $1500\,\mu\text{s}$ after triggering the valve, as there was a very large spike in peak line-integrated electron number density between the $-1500\,\mu\text{s}$ and $-1800\,\mu\text{s}$ cases that was sustained at $-2100\,\mu\text{s}$.

Using this result, a higher-resolution scan was performed between -1600 and $-2000\,\mu$s at $100\,\mu$s intervals with at least three shots taken at each of these timing delays, providing average jet parameters for each time value to achieve a more accurate performance estimate, as well as to assess the repeatability of the result at each time. Figure 3.3b shows the peak line-integrated electron number density plus or minus one sigma standard deviation for each delay time. At $-1900\,\mu$s, the peak density is highest; however, standard deviation is also high, suggesting that either the $-1900\,\mu$s case or $-2000\,\mu$s case (for which average peak density was slightly lower but standard deviation was better than the $-1900\,\mu$s delay time) may be ideal. When comparing this result to the average spectral data for the same set of shots, it is clear that the $-1900\,\mu$s delay time is ideal. Figure 3.3c compares the average peak intensity for three of the strongest Ar-II lines and one impurity line. At $-1900\,\mu$s the intensity of each Ar-II line is at its peak, suggesting that the most argon is being ionized at that delay time.

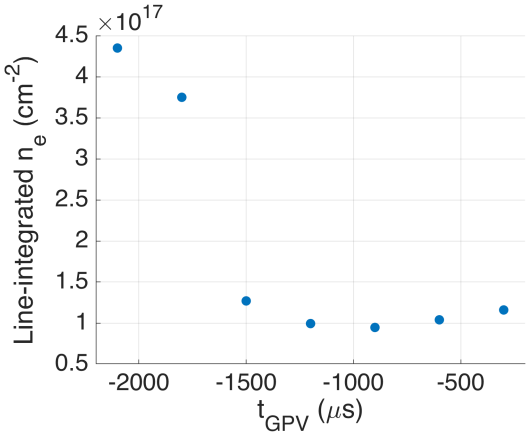

(a) Comparing line-integrated electron number density for a broad scan of gas-puff valve (GPV) timing, all data points for shots taken at 15 kV PFN charge voltage and 700 kPa argon gas

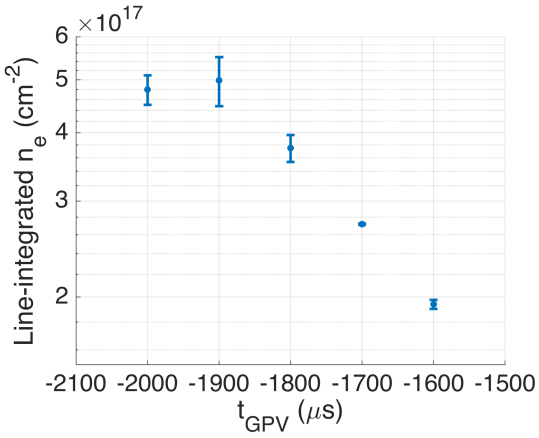

(b) Fine-tuning GPV timing based on results from 3.3a, mean line-integrated n_e plus or minus one sigma standard deviation shown for each time, all data points for shots taken at 15 kV PFN charge voltage and 700 kPa argon gas

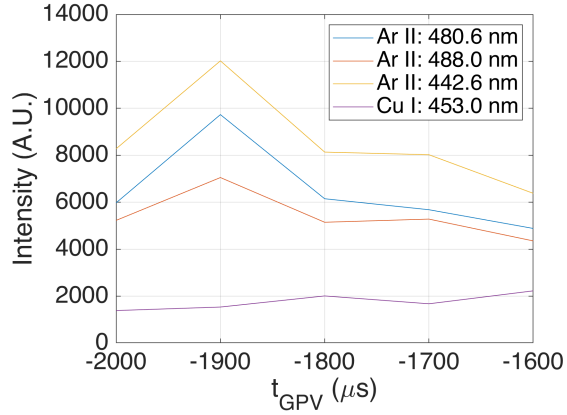

(c) Comparing spectral intensity of singly-ionized argon and an impurity for varying GPV timings

Figure 3.3: Finding the ideal puff valve timing

3.2.2 Finding Ideal Gun Pressure

Using $-1900\,\mu$s GPV time delay for all shots, the line pressure of the argon gas and PFN charge voltage were set to either 350 and 700 kPa and either 10 and 15 kV, respectively, to see how the plasma-jet parameters were affected. Figure 3.4 shows the results. Increasing the pressure from 350 to 700 kPa had a large effect on line-integrated electron number density, as the density nearly doubled for the 10 kV case and nearly tripled for the 15 kV case. The effect of pressure was not as pronounced in the spectral data. At 10 kV, increasing the pressure had very little effect, suggesting that the increase in density seen for this case was due either to an increased amount of neutral argon or other impurities not captured with the spectrometer for this set of shots. At 15 kV, there was a noticeable increase in argon intensity when pressure was increased, but again the effect was not as great as seen in the line-integrated density data.

The effect of increased PFN charge voltage correlated well between the interferometric and spectral data sets. At 350 kPa, increasing from 10 to 15 kV had very little effect on either the line-integrated density or Ar-II intensity; whereas, at 700 kPa, the intensity of all the Ar-II lines and the peak magnitude of line-integrated electron number density increased substantially. The Cu-I impurity intensity did not change much for any case. Overall, using 700 kPa argon gave the best results; therefore, $-1900\,\mu$s GPV timing and 700 kPa argon was used in the gun for the remainder of the experiments discussed in this work.

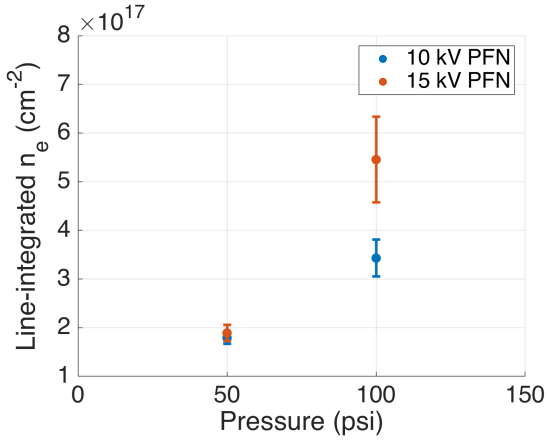

(a) Comparing line-integrated electron number density for varying argon gas line pressures and PFN charge voltage, GPV timing was at $-1900\,\mu$s for all shots

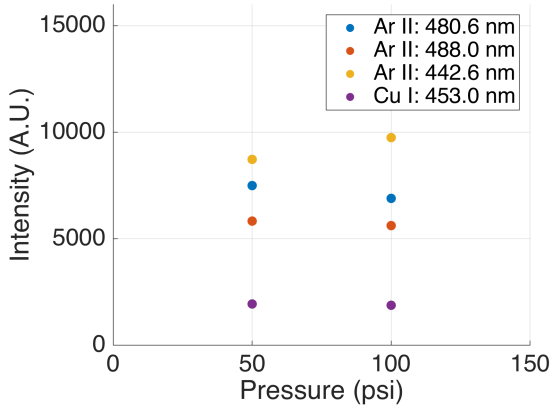

(b) Comparing spectral intensity of singly-ionized argon and an impurity for varying argon gas line pressures at 10 kV PFN charge voltage, GPV timing was at $-1900\,\mu$s for all shots timings

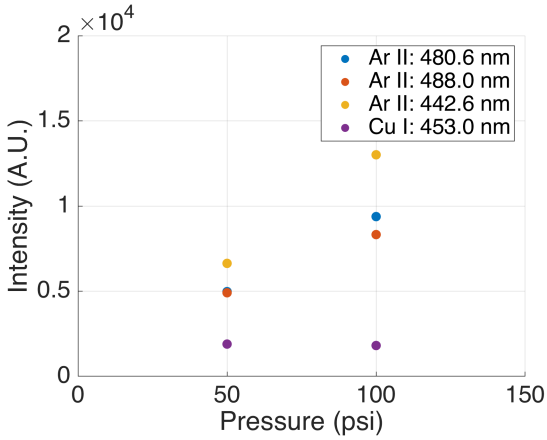

(c) Same as Figure 3.4b but for 15 kV PFN charge voltage

Figure 3.4: Comparing gun parameters for varying PFN charge voltage and argon gas line pressure

3.3 Plasma-jet Characterization

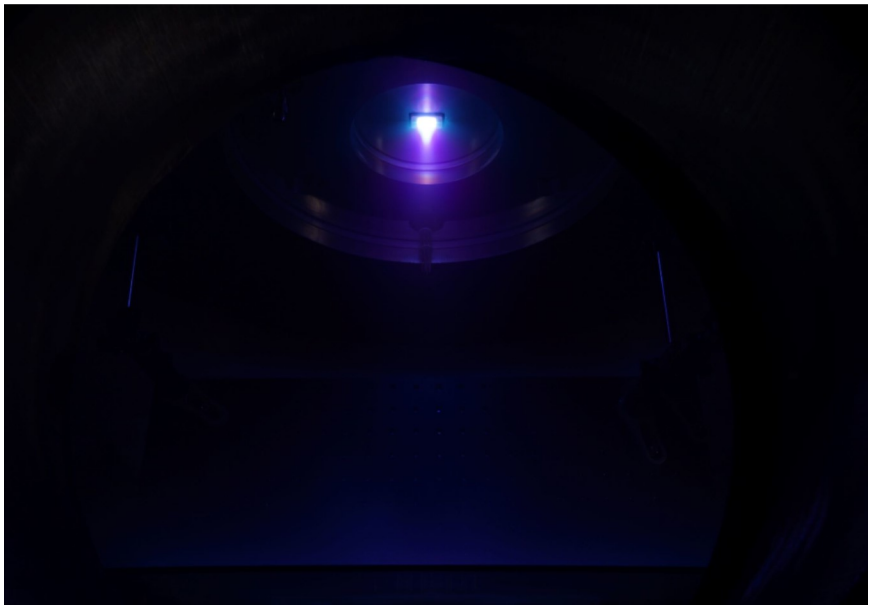

(a) 10 kV PFN charge voltage

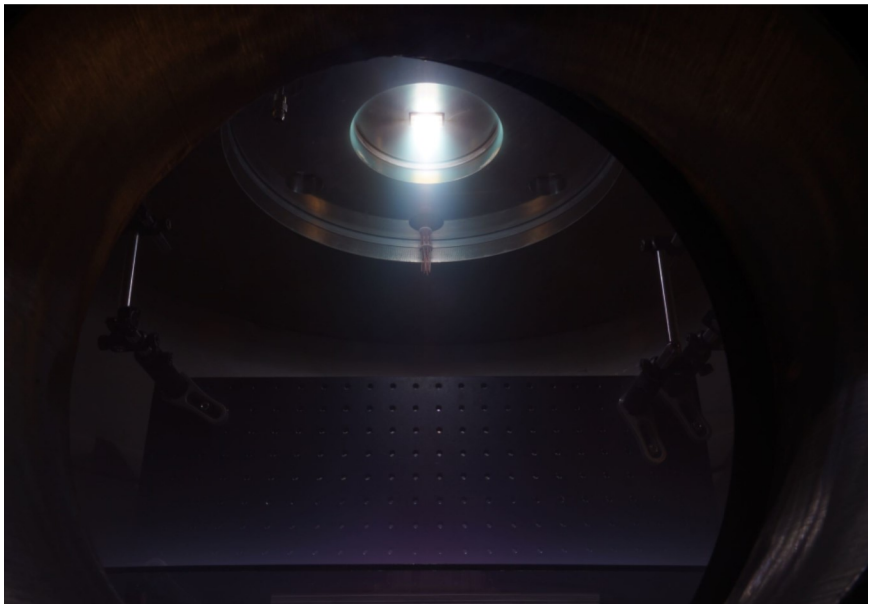

(b) 15 kV PFN charge voltage

Figure 3.5: Long exposure photograph of plasma leaving barrel of gun and propagating into the vacuum chamber. The jet's velocity direction is out of the page and down.

After determining the ideal argon pressure and gas puff timing relative to the pulse-forming

network's discharge, 700 kPa and $-1900\,\mu$s, respectively, an experimental campaign was conducted to fully characterize the plasma-jets accelerated into the vacuum chamber via the linear plasma-armature railgun. The only gun parameter that was changed during this campaign was the PFN charge voltage, which was set at either 10 or 15 kV. Similar to the previous campaign, the jet was completely unobstructed except for the breadboard mounted inside the chamber. The single-chord interferometer and high-resolution spectrometer optics were set up to intersect the bore-sight axis of the gun at one of three locations: $z = 10.2$, 20.3, or 40.6 cm in order to understand how the plasma-jet characteristics evolved as the jet propagated into the chamber.

3.3.1 Jet Composition

While the experiments just presented to tune the railgun performance ensured that the plasma jets accelerated by the gun would contain close to the highest ratio of argon to impurities possible, the composition of the jets likely still includes a non-negligible amount of impurity material from the plasma-facing railgun components. This material mixes with the argon when it is ablated from the railgun's internal structure as the jet accelerates down the bore of the gun. To estimate the proportion of argon to impurity species by mass present in the accelerated jets, the pressure rise in the vacuum chamber just following each shot was recorded and compared to the pressure rise measured when gas was puffed into the chamber without discharging the capacitor bank. The result of this test, which showed that there is no statistical difference between the argon mass concentration between the two PFN charge voltage cases, was that the jets contain $48.0 \pm 4.3\,\%$ argon by mass.

Figure 3.6 shows a typical time-integrated, visible-range spectrogram taken of the plasma at $z = 10.2$ cm using the compact Thorlabs spectrometer. The wavelength of the high-

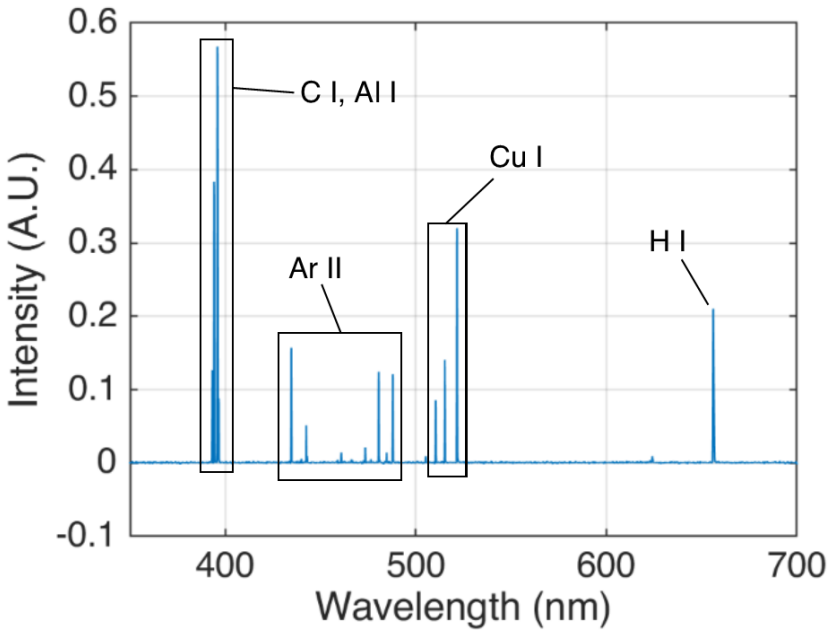

Figure 3.6: Typical visible-range, time-integrated spectrogram of plasma at $z = 10.2\,\mathrm{cm}$ used to identify species contained in accelerated jets, the main wavelength range where singly-ionized argon and the most prominent impurities appear is labeled

est intensity spectral peaks in spectrograms such as this one were compared to the NIST Atomic Spectra Database [34], to help identify which species produced them. The wavelength ranges where singly-ionized argon and a few of the more prominent impurities are typically observed are also highlighted in the figure. Using this method of analysis, the impurities that contribute most to this visible-range spectrum include hydrogen, copper, carbon, and aluminum.

3.3.2 Temperature

Spectral data was used to estimate plasma jet temperature using a technique known as the ratio method. In this technique, assuming optically thin conditions and that the plasma is in local thermal equilibrium (LTE), the ratio of intensities between two spectral lines from

the same species and ionization state is given by [35]

$$\frac{I_1}{I_2} = \frac{g_1}{g_2}\frac{A_1}{A_2}\frac{\lambda_2}{\lambda_1}e^{\left[-\left(\frac{E_1-E_2}{kT}\right)\right]} \tag{3.2}$$

where I is intensity, g is the statistical weight of the transition's upper energy level, A is the transition probability, lambda is the wavelength, E is the upper energy level of the transition given in eV for the two spectral lines, and T is the plasma temperature.

Figure 3.7 shows a typical time-integrated spectral plot taken with the high-resolution Princeton Instruments spectrometer in the wavelength range where singly-ionized argon is most prominent. The two singly-ionized argon lines used to estimate temperature, at $\lambda = 460.96$ nm and $\lambda = 487.99$ nm are labeled in the figure. Many other Ar II lines were present in each shot; however, these two lines were chosen for the large difference between the upper energy level, E, of each transition. Choosing two lines with a large difference in E produces the most accurate estimation, as any error in measured intensity has less of an affect on the temperature calculated. The value of E and of the remainder of the spectral transition constants were gathered from the NIST Atomic Spectra Database [34].

In actuality, the accelerated plasma-jets are most likely not in local thermodynamic equilibrium. This is based on other plasma-jet sources which produce jets with similar parameters [25]. Since this is the case, a detailed analysis of jet temperature is saved for Chapter 4, where a more precise method of estimating temperature is used. For this analysis, temperature is necessary only to estimate plasma jet collision parameters and penetration lengths relevant to collisional jet experiments; therefore, an average temperature using the method described above was calculated for the entire set of shots. Using this method, average plasma temperature calculated via the ratio method across all gun parameters and diagnostic set-

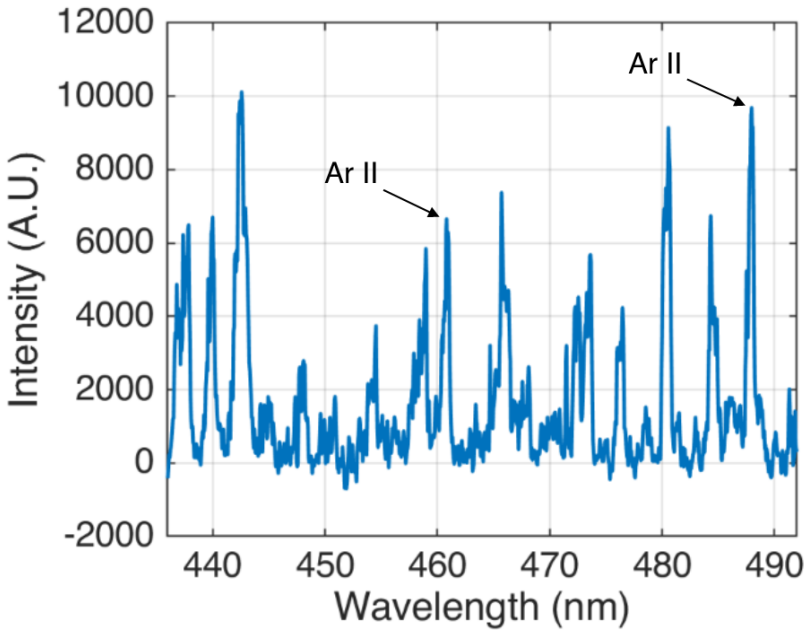

Figure 3.7: Binned spectral data for shot 408 with labels on the two singly-ionized argon lines used for temperature estimation in each shot. $Z = 10$ cm and $V_{PFN} = 15$ kV for this shot.

tings is $T = 2.0 \pm 0.9$ eV.

3.3.3 Density and Jet Profile

Plasma density was inferred based on a combination of line-integrated electron-number density measured with the interferometer and jet widths estimated using low gate time, visible-spectrum images of the plasma. The qualitative progression of jet profile is represented in Figure 3.8, which displays normalized traces of the mean density trace averaged over five to ten shots at each bore-sight axis measurement location for the two PFN charge voltage cases. The sharp rise, narrow width, and rapid fall of the signal spike in these traces suggest that the plasma has left the gun as a cohesive mass that has a distinct leading and trailing edge and is somewhat thin. Short-exposure image-intensified photographs of the plasma

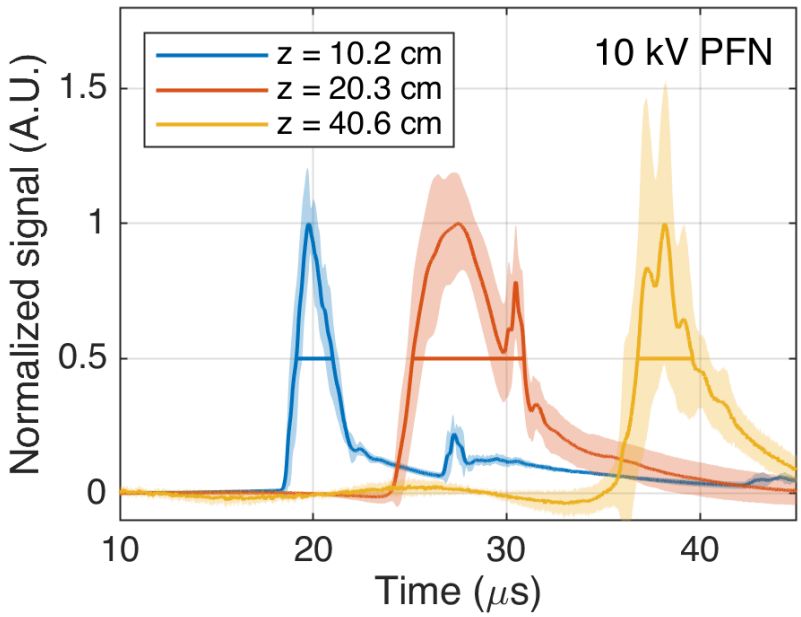

(a) 10 kV PFN charge voltage

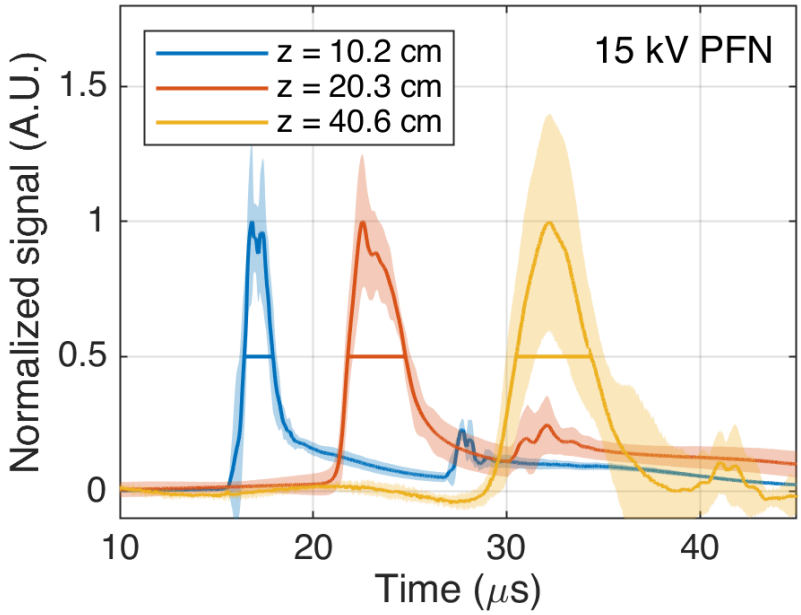

(b) 15 kV PFN charge voltage

Figure 3.8: Normalized and averaged interferometer phase shift signals versus time with plus or minus one sigma standard deviation. FWHM of the average signal is also shown and was used to calculate average jet thickness.

support this qualitative description. Figure 3.9 shows one such gray-scale image (3 ns gate width, f/8 aperture, $t = 15\,\mu$s after the gun was fired) of the plasma propagating into the chamber. This image was taken with the center axis of the camera's viewing chord directly perpendicular to the bore-sight axis of the gun; therefore, the velocity vector of the jet in the image is upwards along the plane of the page. As suggested based on the normalized interferometer traces in Figure 3.8, the jet appears to be thin, with a distinct leading and trailing edge based on the rapid change in intensity from the image background to plasma jet.

Low gate time images of the plasma, all using the same viewing chord as shown in Figure 3.9a, were used to estimate jet width and thickness as a function of z-axis position of the jet's leading edge. Calculating lengths in the horizontal plane at the bore-sight axis of the chamber based on images is done by mapping holes in the breadboard inside the chamber to the horizontal plane at the z-axis and then to pixel coordinates on the iCCD image. Since the camera was positioned such that the center axis of the camera's viewing chord was normal to and intersected the bore-sight axis of the gun, this process was relatively simple.

Figure 3.10 shows a side-view schematic detailing how this mapping was obtained. The figure shows the relative position between the iCCD, the bore-sight axis of the gun, and the optical breadboard mounted inside the chamber. Points *p1* and *p2* in the figure correspond to the same pixel on the iCCD's sensor. Since the center viewing axis of the camera is perpendicular to the bore-sight axis, the ratio of distances *d2* to *d1* is equal to the ratio of the distance from the iCCD to the breadboard to the distance from the iCCD to the bore-sight axis plane. This is shown in Figure 3.10 for distances along the z-axis but the same holds true for distances in the direction in and out of the page in the schematic.

For a given image, the jet thickness was first estimated by user-defining the pixel column roughly at the center of the jet and then binning intensity for twenty columns on either side

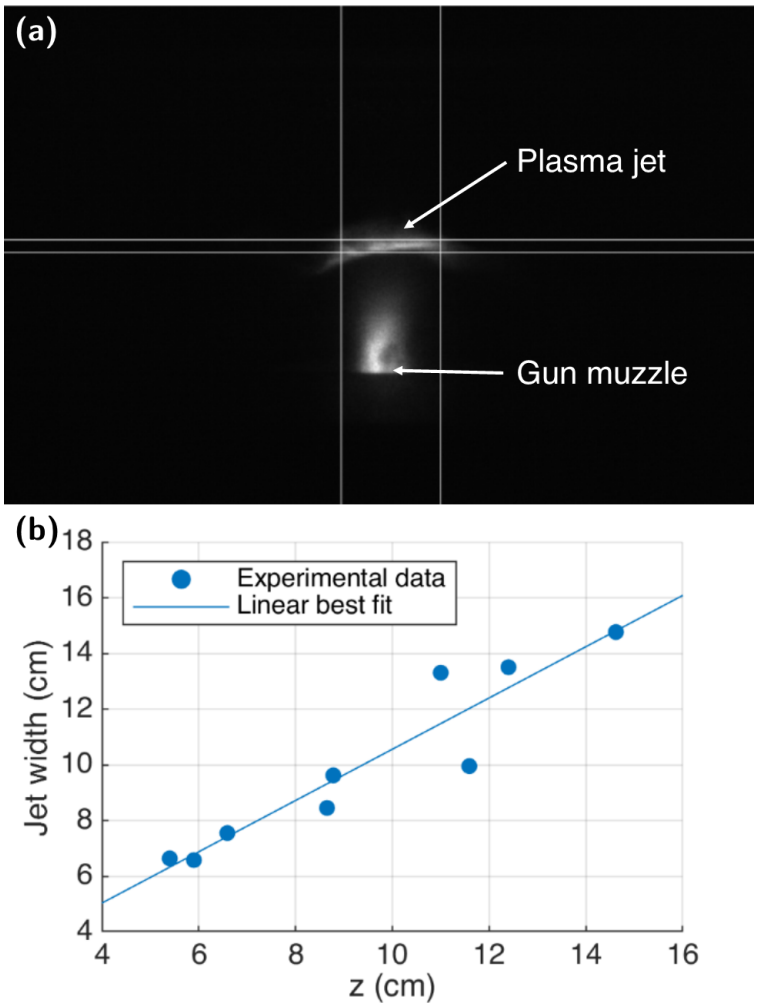

Figure 3.9: (a) Image-intensified, VIS-range spectrum, gray-scale image of plasma-jet taken with 3 ns integration time, f/8 aperture, at $t = 15\,\mu$s. The velocity vector of the jet is directly upwards along the surface of the page. (b) Scatter plot of experimentally estimated jet widths as a function of z-axis leading edge location and linear line of best fit.

of the chosen jet center column. The full-width, half-maximum (FWHM) of the line-out of that binned region was then defined as the jet thickness. Jet width was then estimated by binning the pixel rows corresponding to the jet thickness and taking the FWHM of the line-out of that binned region as the jet width. Figure 3.9a shows two vertical and two horizontal white bars denoting the jet width and thickness calculated for that image using this method. This was repeated for all PIMAX images taken using this camera view and

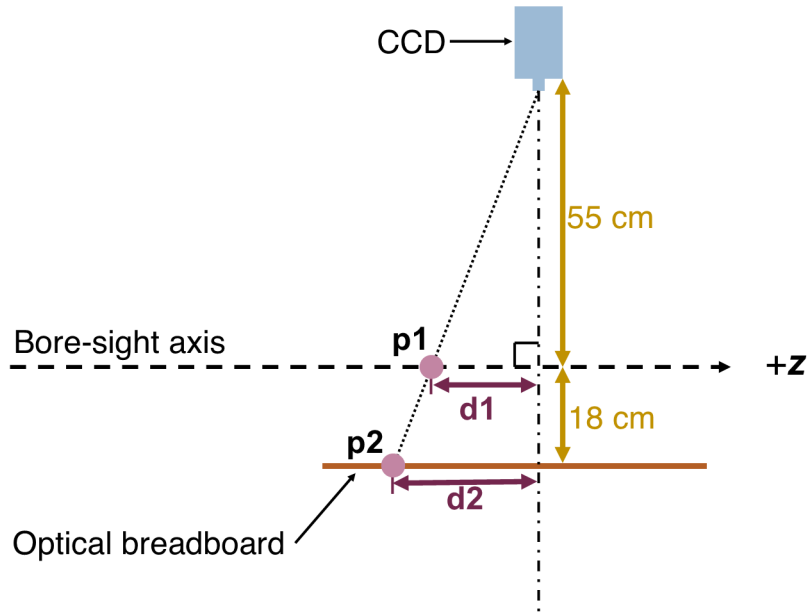

Figure 3.10: Side-view schematic of iCCD camera position relative to bore-sight axis and optical breadboard showing how jet lengths at the horizontal z-axis plane were estimated using a grid of holes in the optical breadboard mounted inside the chamber.

Figure 3.9b shows a scatter plot of each of the individual jet width estimates as well as a linear line of best fit. That best fit line was used as the estimate of jet width as a function of z-axis position and is given by

$$w = 0.92z + 1.37 \tag{3.3}$$

where z is the distance along the bore-sight axis to the leading edge of the jet and w is the width of the jet at the leading edge location, both in centimeters.

Figure 3.11 compares the peak electron number density for both the 10 and 15 kV PFN charge voltage cases at each distance along the bore-sight axis, as discussed previously. For the 10 kV case, the average peak jet density decreases from 1.6×10^{16} to 1.7×10^{15} to

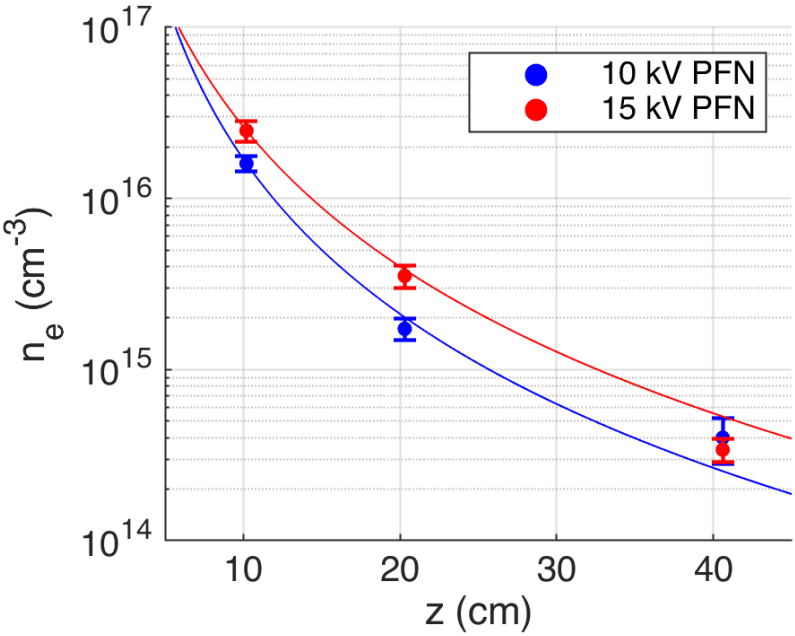

Figure 3.11: Average electron number density with one sigma standard deviation error bars comparing PFN charge voltage and interferometer chord position. The line superimposed onto the plot shows a semi-analytical prediction of jet density assuming adiabatic expansion and using the 10.2 cm experimental measurement as a reference point.

$4.0 \times 10^{14}\,\mathrm{cm}^{-3}$ from $z = 10.2$ to 20.3 to 40.6 cm, respectively. For the 15 kV case, the average peak jet density decreases from 2.5×10^{16} to 3.5×10^{15} to $3.4 \times 10^{14}\,\mathrm{cm}^{-3}$ from $z = 10.2$ to 20.3 to 40.6 cm, respectively. Jets are being accelerated into a chamber with very high vacuum level ($< 1\,\mu$Torr), where it is expected that the collision rate between the jets and background molecules in the chamber are low enough such that any deceleration is negligible; therefore, the reduction in jet density as a function of z-axis position should correlate roughly with the adiabatic expansion of a gas in vacuum. Figure 3.11 also displays a semi-analytical prediction of jet density assuming expansion under these conditions, which approximately matches measured density.

In order to approximate jet thickness, full-width half-maximum (FWHM) of the interferometer phase-shift signal spike in each shot was measured and averaged. In order to visualize this process, the FWHM of each average interferometer phase-shift trace is also plotted in Figure 3.8. The average velocity for each PFN charge voltage case shown in Table 3.1 was used along with the average FWHM time calculated from the phase-shift traces to predict average jet thicknesses. For the 10 kV PFN charge voltage case, jet thickness was estimated as 2.4, 7.2, and 3.4 cm and for the 15 kV case, jet thickness was estimated as 2.6, 5.6, and 7.6 cm for the $z = 10.2$, 20.3, and 40.6 cm locations respectively. This estimation of jet thickness done using interferometer phase-shift data is compared to the jet thickness estimation done using fast-camera images in Figure 3.12. Each plot point for the fast-camera images data-set represents thickness calculated for an individual image, whereas the plot points for the interferometer cases are the average thicknesses estimated for that chord position and PFN charge voltage case. For the 10.2 cm interferometer chord position, the same region where fast-camera images of the jet were taken, the jet thicknesses inferred using each method roughly agree given the shot to shot deviation in fast-camera image estimates. Overall, the interferometer method resulting in a slightly larger thickness than the average

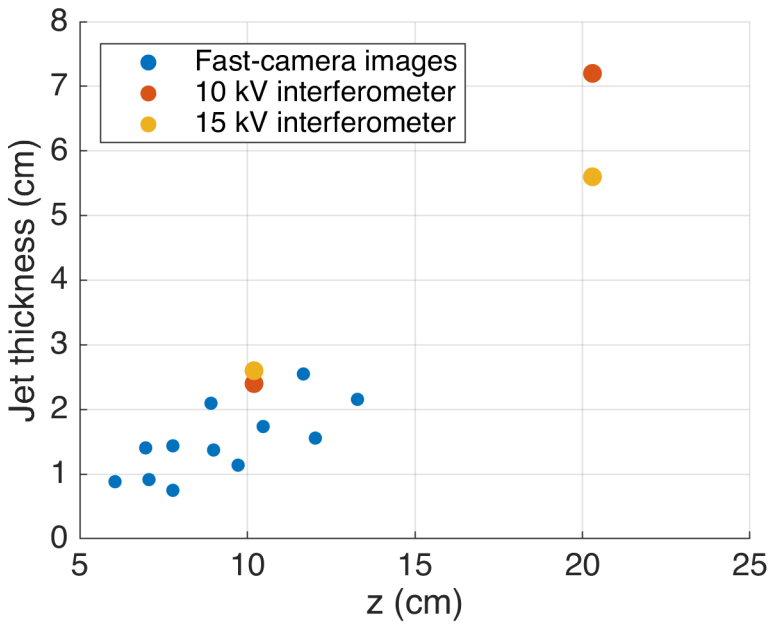

Figure 3.12: Scatter plot comparing the jet thickness versus z-axis position estimated using fast-camera images and using interferometer phase-shift data.

thickness obtained using fast-camera images.

3.3.4 Velocity and Mach Number

The bulk plasma jet velocity was determined by considering the time the peak in interferometer phase shift signal occurred at each location along the gun's bore-sight axis for the 10 and 15 kV PFN charge voltage cases. In order to produce a robust time-of-flight based calculation of velocity using the single chord interferometer, a jet velocity was calculated for every possible combination of two shots with the same PFN charge voltage and different bore-sight axis measurement location. A single average jet velocity and standard deviation for each of the two PFN charge voltage cases, shown in Table 3.1, was then calculated from each set of binary-shot velocity predictions. Using this estimate of jet velocity and assuming a plasma temperature of 2.0 eV (see Sec. 3.3.2) and pure argon plasma jets, Mach number,

$\mathcal{M}$, of the jets defined as [36]

$$\mathcal{M} = \frac{u_0}{\sqrt{\gamma \bar{Z} \frac{k_B T_e}{\bar{m}_i}}} \tag{3.4}$$

where u_0 is the bulk plasma jet velocity, γ is the adiabatic index, $\bar{Z}$ is the mean charge state, $\bar{m}_i$ is the average ion mass, T_e is the electron temperature, and k_B is the Boltzmann constant, was estimated and is also displayed in Table 3.1.

Table 3.1: Comparison of the time of peak interferometer phase shift signal for changing PFN charge voltage and interferometer probe beam position, estimated jet velocity based on that peak time, and plasma Mach number for each PFN charge voltage case

V_{PFN}(kV)	Z(cm)	$t_{\phi_{max}}(\mu s)$[1]	V_{jet}(km/s)	$\mathcal{M}$
10	10.2	22.1 ± 0.60		
10	20.3	29.8 ± 1.50	14.5 ± 3.9	5.1 ± 1.4
10	40.6	44.4 ± 4.02		
15	10.2	18.3 ± 0.27		
15	20.3	24.0 ± 0.60	19.7 ± 2.6	7.0 ± 0.9
15	40.6	34.1 ± 1.38		

It is important to point out here that the presence of a second jet being accelerated from the railgun is observed in the normalized and averaged density traces in Figure 3.8. That second jet is the smaller amplitude peak that follows the first, specifically in the $z = 10.2$ and 20.3 cm chord positions. This second jet, which is not fully characterized in this chapter appears to be traveling at a higher velocity than the first jet, based on the difference in arrival time between interferometer chord positions as compared to the first jet. This velocity is estimated and discussed in more detail in Sec. 4.2.2. Since the velocity in the second jet is faster than the first, it appears to catch up to the first jet and the two are indistinguishable by the time the jets pass the 40.6 cm chord position. This second jet affects and explains

the very high jet thickness calculated using the interferometer traces at the 20.3 cm chord position for the 10 kV PFN charge voltage case. The question as to whether this second jet affects the velocity of the first jet also arises, since average velocity for each PFN charge voltage case was calculated using all three chord positions. To make this comparison, the jet velocity for both PFN charge voltage cases was calculated between the 10.2 and 20.3 cm chord position cases given the average time of peak interferometer signal for those two chords and compared to the average velocity reported in Table 3.1. For the 10 kV case, velocity between the first two chord positions is 13.2 km/s and for the 15 kV case, velocity is 17.8 km/s. In both cases, this velocity is $\approx 90\%$ of the average velocity listed in Table 3.1. This suggests that the arrival of the second jet to the first may accelerate the first jet slightly, but not to a degree that greatly affects the jet parameters.

3.3.5 Collision Parameters Relevant to Study of Colliding Jets

Using the estimate of plasma temperature above as well as the jet velocity and density data presented in previous sections, it is possible to estimate plasma collision parameters, such as ion-ion collision rate and ion penetration length, to help understand this collisionality as it pertains to the study of merging or colliding plasma-jets. Similar to other experimental plasma jets of similar parameter space, it is found that the ion-ion collision rate assuming counter-streaming ions is the limiting factor for ion penetration in this experiment's jets [29]. This collision rate, $\nu_s^{i|i'}$, is calculated in the fast approximation as [37]

$$\frac{\nu_s^{i|i'}}{n_{i'} Z^2 Z'^2 \lambda_{ii'}} \approx 9.0 \times 10^{-8} \left(\frac{1}{\mu} + \frac{1}{\mu'} \right) \frac{\mu^{1/2}}{\epsilon^{3/2}} \tag{3.5}$$

where the Coulomb logarithm, $\lambda_{ii'}$ is given by

$$\lambda_{ii'} = 43 - \ln\left[\frac{ZZ'(\mu+\mu')}{\mu\mu'\beta_D^2}\left(\frac{n_e}{T_e}\right)^{1/2}\right] \tag{3.6}$$

where the field particle parameters are represented by a prime, Z is the mean charge state, μ is the average ion to proton mass ratio, ϵ is the test particle kinetic energy, β_D is fractional velocity compared to the speed of light defined as $\beta_D = v_D/c$, c is the speed of light, n_i and n_e are the ion and electron densities, respectively, and T_e is the electron temperature. Units are cgs and ϵ and T_e are in eV. Jets were assumed to be 100 % argon and $Z \approx 1$ for this estimation. In addition, the hypothetical jet collision geometry considered is a jet exiting the railgun's bore and colliding with a stagnant plasma of equal temperature and density; therefore, ϵ is calculated using the velocity calculated in Section 3.3.4 and the test and field particle parameters are all equal. Finally, the ion penetration length is given by [29]

$$\lambda_i^s \approx \frac{v_{rel}}{4\nu_s^{i|i'}}. \tag{3.7}$$

Table 3.2 gives collision rates and ion penetration lengths calculated based on estimations of density for each given shot, average velocity based on PFN charge voltage, and average electron temperature for the entire data set. The ion penetration length, λ_i^s, listed in the last column is expected to be of similar spatial scale to the thickness of an ion shock wave under the same condition [29]. Altering the PFN charge voltage and z-axis location where the measurement was taken greatly affects the collision parameters. Based on the ion penetration length, which is close to or greater than a centimeter somewhere between $z = 20.3$ and $z = 40.6$ cm, for both charge voltage cases the gun is producing jets in the range that will

allow for the study of shock structures that have thicknesses on the order of a centimeter, matching the performance goal set when initially designing the accelerator.

Table 3.2: Range of repeatedly-achievable plasma collision parameters based on the data presented in this chapter.

V_{PFN} (kV)	z (cm)	$\nu_s^{i\|i'}$ (s^{-1})	λ_i^s (cm)
10	10.2	1.2×10^7	0.030
10	20.3	1.5×10^6	0.24
10	40.6	3.8×10^5	0.96
15	10.2	8.0×10^6	0.062
15	20.3	1.3×10^6	0.39
15	40.6	1.5×10^5	3.6

3.3.6 Ion Spatial Distribution in Pre-shocked Jets

Finally, an important experiment that must be conducted before any attempt to identify separation of ion species induced by a plasma shock can be conducted is to determine whether the unobstructed jets have a homogeneous mixture of ions or if there is any separation occurring before any collision event. To conduct this study, a large plate of polycarbonate was placed inside the chamber, obstructing the jet path (see more details on this plate in Sec. 4.1.1, where this obstruction is a crucial part of inducing jet collisions). The high-resolution spectrometer's optical lens was then positioned to look at the impact point between the plasma jet and the obstruction. When each species in the plasma hit the polycarbonate, it becomes brighter during that collision process. Reducing the integration time of the spectrometer to few- or sub-microsecond time-scales made it possible to find the time that this occurred for each species, and to compare the results to see if any species seemed to be outrunning or lagging behind the bulk of the jet.

It is important to note here that in between the campaign to characterize the unobstructed

plasma jets that has been discussed in this chapter up to this point and the campaign to assess the ion mixture in the unobstructed jets discussed in this section, a discovery was made that running the railgun at 15 kV caused significant damage to internal gun components. All damaged components were repaired except the electrodes, which were replaced with a second pair of identical geometry, machined from a 75 % tungsten, 25 % copper alloy. Recall the first pair was a 55 % tungsten, 45 % copper alloy. Experiments following this switch were done and no significant change to the jet parameters presented up to this point was seen. From this point on, however, a determination was made not to run the railgun at charge voltages above 10 kV to reduce further damage to the accelerator. Many hundreds of shots have been taken since this swap and no damage or erosion has occurred that has led to a reduction in gun performance.

For these tests experiments to diagnose ion distribution within the unobstructed plasma-jet, 700 kPa argon gas line pressure and $-1900\,\mu$s gas puff valve timing was used for all shots, the same parameters used to characterize the plasma parameters for the unobstructed jet previously. In addition, the polycarbonate was mounted at $z \approx 20$ cm for all shots.

Figure 3.13 shows a plot of normalized intensity of spectral lines from a number of species and ionization states as a function of time. The spectral lines that are plotted here represent the most prominent line from each species typically captured. The width of each plot point is equal to the integration time used on the CCD to capture the spectra for that shot, which has also been accounted for when creating this plot such that the intensities of shots with different integration times can be compared fairly. The peak intensity for each spectral line correlates to the time the bulk of that species impacted the polycarbonate.

Note that the range of times plotted and where data was acquired covers both the first and second jet to leave the gun. Based on the interferometer trace for the 10 kV PFN charge voltage case at $z = 20$ cm the first jet should arrive at the polycarbonate between around

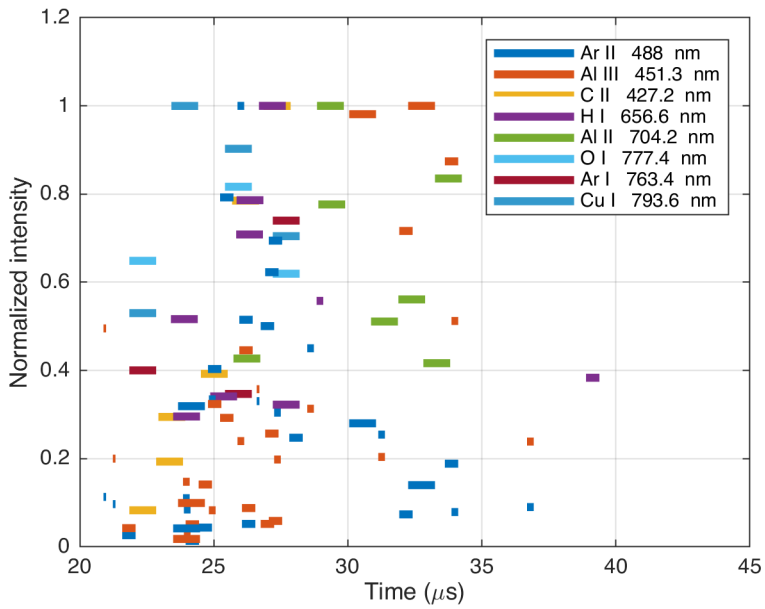

Figure 3.13: Plot of normalized intensity of spectral lines from the most prevalent species in the plasma jet as a function of time, the width of each data point is equal to the integration time used for that shot

the 28 μs time and the second jet around the 31 μs time. To estimate ion distribution in the first jet, the data points acquired at times greater than 30 μs were discarded and the delay time of peak intensity was estimated as the arrival time for each species and is listed in Table 3.3. Figure 3.14 plots that arrival time as a function of atomic weight and color codes the data-bar for each species based on ionization state. The length of the vertical bar of each plot point is equal to the spectrometer integration time used for that shot, just as was the case for the horizontal bars in Figure 3.13.

The data presented in Table 3.3 and in Figure 3.14 show that some separation of species within the unobstructed jet may be present. About half the species have peak intensity between 26 and 28 μs, whereas the neutral carbon, argon, and copper arrive closer to 24 μs and the singly-ionized aluminum arrives at 29 μs. It could be plausible that the lighter ion species with higher mobility outrun the heavier species, but based on Figure 3.14, there is no

Table 3.3: Species arrival time based on spectral data for the first jet

Species	$t_{arrival}$ (μs)
H I	23.4 - 24.4
C II	26.9 - 27.9
O I	23.4 - 24.4
Al II	28.9 - 29.9
Al III	26.0 - 26.5
Ar I	23.4 - 24.4
Ar II	25.9 - 26.1
Cu I	23.4 - 24.4

clear correlation between arrival time and atomic weight. In this result, the neutral species arrive sooner than either singly- or doubly-ionized species, although more data should be obtained to determine whether or not this is a pattern. As a whole, the shot-to-shot jitter in arrival time, which based on interferometer data at $z = 20.3\,\text{cm}$ is about 2 - 3 μs, could also account for much of the measured delay.

The results plotted in Figure 3.13 can also provide some qualitative evidence to describe the difference between the composition of the first and second jet. At the time when the second jet to the leave the railgun is expected to arrive, $\approx 30\,\mu$s, the singly- and doubly-ionized aluminum is higher intensity than the argon lines. This suggests that the second jet is composed of a high proportion of impurities to argon than the first, which makes sense given that the timing of the gas puff to the gun was tuned based on jet parameters and argon presence in the first jet alone.

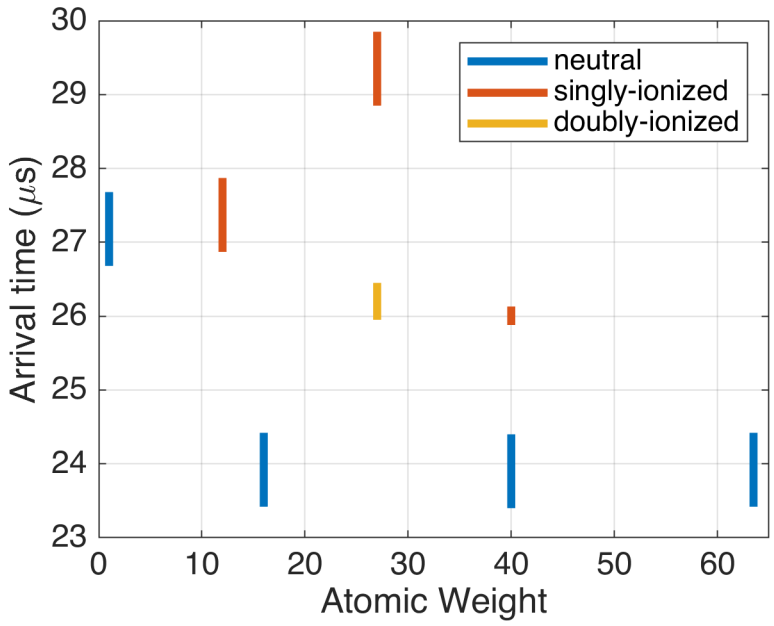

Figure 3.14: Species arrival time as a function of atomic weight and ionization state (each vertical data bar length is equal to the integration time used to capture spectral data during that shot

Chapter 4

Obstructed Jet Experiments

Chapter 3 discussed results from an effort to characterize the plasma jets accelerated using the railgun and explore the viability of using the jet source to study shock-driven species separation. In both the 10 and 15 kV PFN charge voltage cases, it was shown that the ion penetration length, which is expected to be similar in spatial scale to the shock thickness in jet collisions [29], was on the order of a few millimeters around $z = 20\,\mathrm{cm}$. This chapter presents a campaign conducted where collisions between jets were induced in an attempt to produce a shock wave with centimeter-scale thickness, forming the strong basis upon which an experimental validation of the various ion-species separation mechanisms can be conducted.

4.1 Experimental Setup

When the accelerator was being developed, visions for jet interaction or collision experiments saw a second railgun mounted to the chamber such that when fired simultaneously, the jets would either hit head-on or at a right angle dependent on where the two accelerators were mounted, similar to the types of experiments that had been and are currently being conducted as part of the plasma liner experiment (PLX) [28, 29, 30, 38]. While this setup certainly would have allowed for the study of multi-ion species shock structures and other interesting phenomena, the overhaul involved in adding a second railgun including building

and finding the space for a second pulse-forming network (PFN), adding the control and auxiliary systems needed to operate two accelerators, and characterizing and tuning the timing of the two jet sources made developing an alternative method of conducting such experiments appealing.

4.1.1 Method of Inducing Jet Collisions

Ultimately, an experimental setup that would allow the study of plasma-jet collisions using the single accelerator that had already been designed and characterized was developed. This solution takes advantage of the under-damped nature of the current pulse delivered to the railgun from the PFN, which as discussed previously, causes multiple jets to accelerate from the muzzle of the gun during each shot. To induce jet collisions, a $40 \times 40\,\mathrm{cm}$, $6\,\mathrm{mm}$ thick clear sheet of polycarbonate was mounted inside the vacuum chamber perpendicular to the accelerator's bore-sight axis (see Figure 4.1) to the optical breadboard that was already mounted inside the chamber. Acting as a rigid obstruction to the propagating plasma jets, when the first jet to exit the gun's bore reached the polycarbonate, it would stagnate, producing a background plasma that subsequent jets accelerated from the railgun would collide with. Although this configuration is slightly different from what was envisioned when estimating collision parameters in Sec. 3.3.5, based on the wide range of collision parameters estimated, it was expected that this method of inducing jet collisions would still be able to produce jets with centimeter-scale shock structures.

4.1.2 Improvements to Diagnostics and Diagnostic Access

In addition to adding the polycarbonate sheet inside the chamber, another major change was made to the experimental configuration for this campaign. As mentioned in Sec. 3.1 and

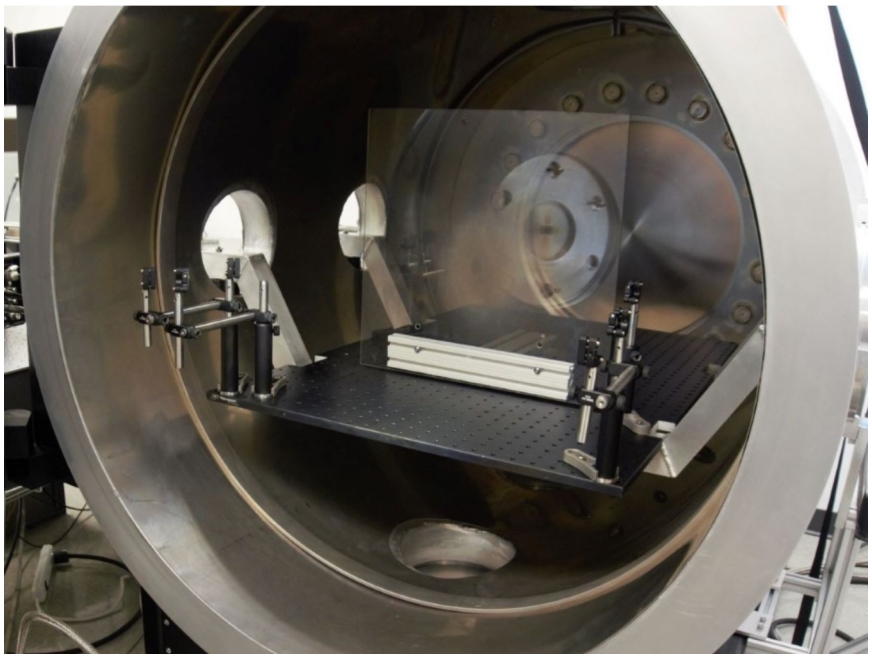

Figure 4.1: 40×40 cm, 6 mm thick piece of clear polycarbonate mounted to optical breadboard inside chamber

shown in Figure 3.1, due to the placement of the eight, 30 cm viewports around the chamber, diagnostic access to the gun bore is difficult at bore-sight axis positions less than $z \approx 40$ cm. Based on the analysis of expected collision parameters done in Sec. 3.3.5, the ideal position to obtain centimeter-scale shock structures is below that $z = 40$ cm location, making any detailed diagnosis of jet or shock structures in that location very difficult, especially when the polycarbonate sheet, which further reduces diagnostic access, is mounted close to the gun bore. In order solve this issue, a large vacuum flange was designed to essentially move the railgun further into the chamber. Figure 4.2 shows two photographs of the flange with the railgun mounted; the top photograph shows the flange on the inside of the vacuum chamber door and the bottom shows the flange and railgun from the outside of the chamber when the door is closed.

Figure 4.3 shows a schematic of the vacuum chamber with this added flange, which moves the location of the railgun bore forward 33 cm along the bore-sight axis. Neither the way in

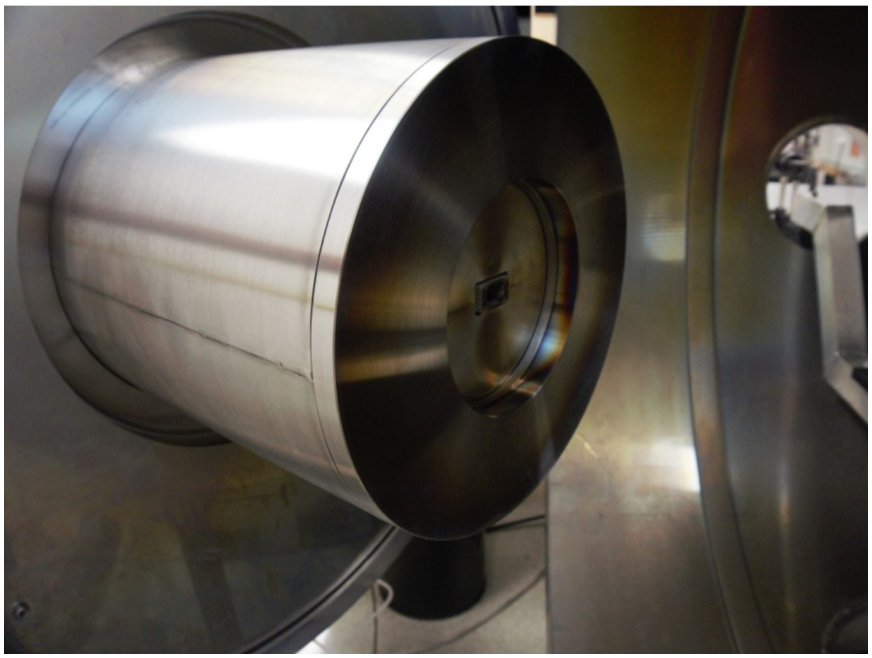

(a) Extension flange mounted to open vacuum chamber door

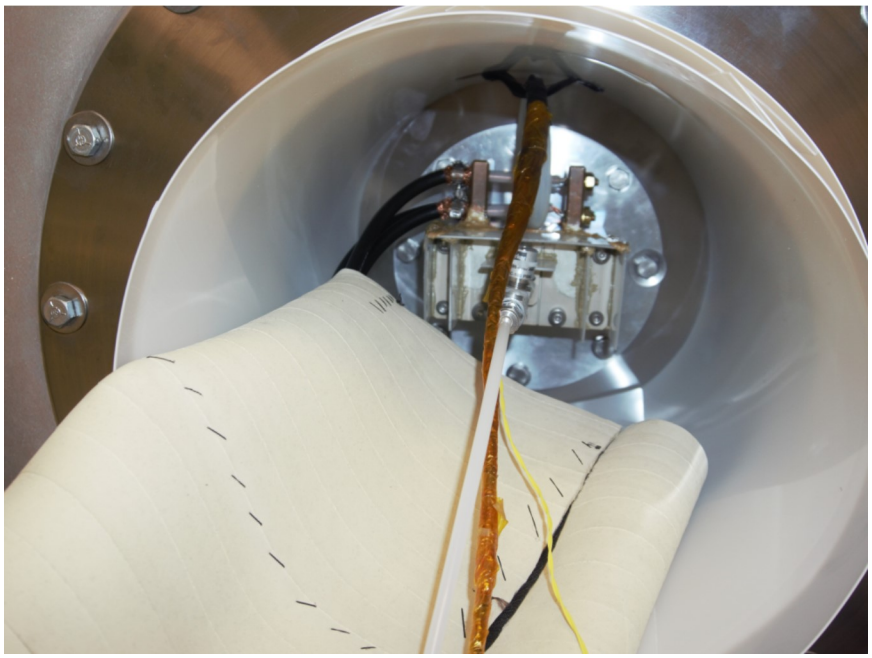

(b) Railgun mounted to extension flange

Figure 4.2: A top-hat-shaped flange replaces a blank port on the door of the vacuum chamber to provide better diagnostic access to the area directly in front of the railgun's bore.

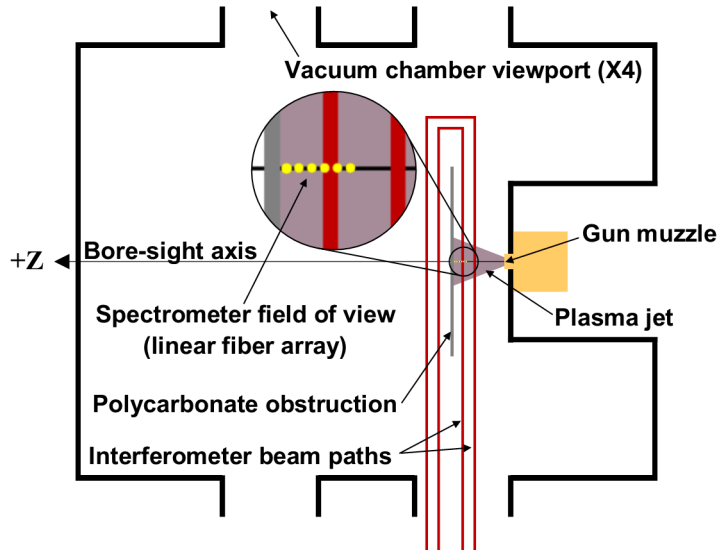

Figure 4.3: Scaled, top-view cross-section schematic of vacuum chamber with added flange designed to move the railgun further into the chamber to provide enhanced diagnostic access to the area close to the gun bore; also shown is the polycarbonate obstruction mounted inside the chamber and the general diagnostic placement

which the gun is mounted to the chamber nor any of the other systems that attach to the gun are altered from the original setup by adding this flange.

Figure 4.3 also details a few other changes made between when the unobstructed jet experiments of Chapter 3 were conducted and when the experiments presented in this chapter took place. A second chord was added to the Mach-Zehnder, heterodyne with quadrature interferometer. This two-chord system still used the single 4 mW linearly-polarized HeNe laser and 80 Mhz acousto-optic modulator (AOM) listed in Sec. 2.3.2. To create a second probe and reference beam, a 50:50 (reflection:transmission) plate beamsplitter (Thorlabs BSW04) is used to split the two beams that exit the AOM. A second Thorlabs PDA10A photodetector is used to capture the recombined second chord, and copies of all the RF electronics used for the first chord are used for the second chord as well, with the only exceptions being the IQ demodulator (a SigaTek model QD51A10 which has identical characteristics to the model used for the first chord) and low-pass filters used to filter out the 80 MHz (two 15 MHz

Thorlabs model EF526 low-pass filters were used for the second chord). While the decision to use the same laser for both chords effectively halves the potential signal-to-noise ratio (SNR) that can be obtained using the interferometer, the SNR obtained in experiment is still more than adequate in capturing even the finest details in the phase shift traces using the two-chord system.

In addition to the second interferometer chord, improvements in the high-resolution spectrometer diagnostic were also made. Prior to this experimental campaign, spectrograms captured using this diagnostic were time-integrated over the entire shot and spatially integrated over a 3" length along the z-axis. In order to be able to capture temporally and spatially integrated spectral data, the single fiber optic cable used to project light emitted from the plasma onto the entrance slit of the spectrometer was replaced with a fiber optic bundle consisting of seven, 200 μm core diameter multimode fibers in a linear array (Thorlabs BFA200HS02). The same lens system described in Sec. 2.3.4 was used for the experiments presented here, but the lens was mounted atop the vacuum chamber, illuminating each fiber in the array with collimated light from within a small-diameter, vertical column that intersects the bore-sight axis of the gun, as shown in Figure 4.3. This fiber bundle allows for capturing spectral data with millimeter-scale spatial resolution and 10s-100s of nanosecond temporal resolution.

The length along the z-axis that each fiber in the array was illuminated by was determined in a two step process using a neon spectral calibration lamp and an 8×8 array of programmable LEDs. In the first step, the neon calibration lamp was used to determine which rows of pixels in the iCCD's sensor were illuminated by each fiber in the bundle. This lamp, which was a long narrow pencil-style bulb, was positioned such that the axis of the lamp was aligned with the bore-sight axis of the railgun and placed right up against the polycarbonate, such that it would illuminate all fibers in the array simulatenously and with relatively even brightness.

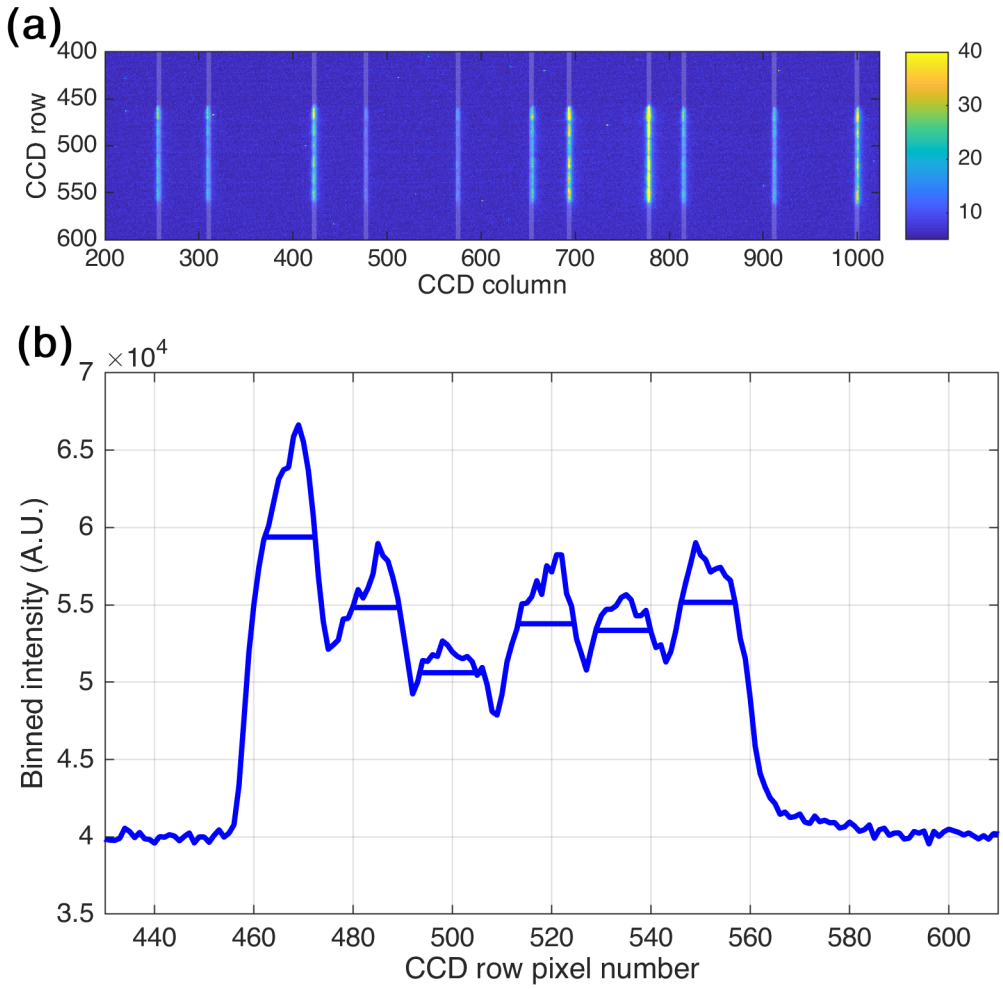

Figure 4.4: (a) False color iCCD image of neon spectral lamp illuminating the fiber-optic bundle, columns that were binned to create the line-out shown below are denoted by transparent white vertical bars. (b) Line-out of binned spectral intensity showing six peaks, representative of each fiber in the array; also shown are horizontal bars denoting the FWHM of each peak used as the CCD pixel range illuminated by each fiber.

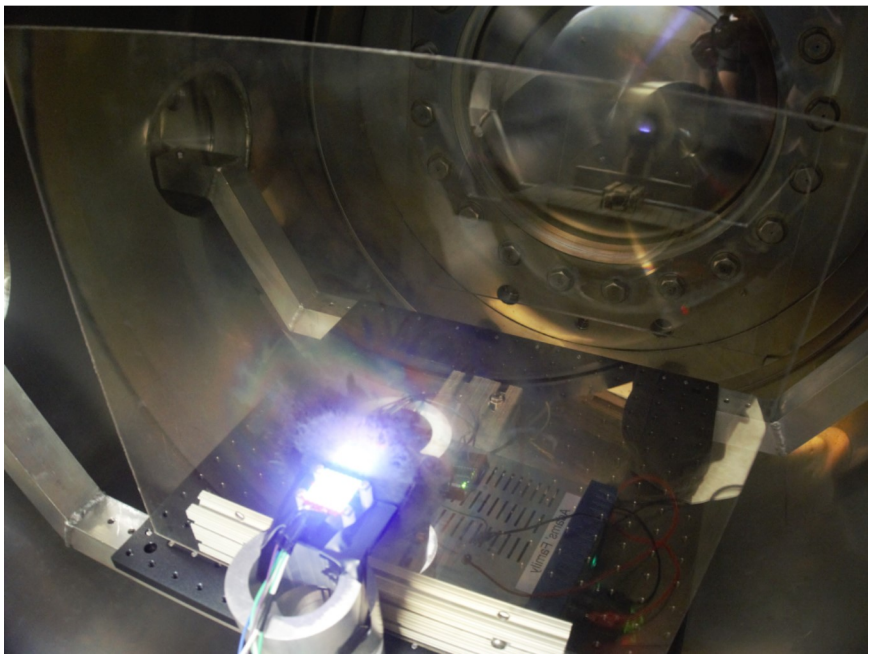

Figure 4.5: A small array of programmable LEDs used to characterize and align the spectrometer optics and fiber array is mounted in the chamber

Figure 4.4 shows a typical spectral image in false color of the neon lamp as well as a line-out of binned intensity used to map each fiber to the iCCD image. Sub-figure 4.4b was created by binning columns where spectral lines appeared, as shown in sub-figure 4.4a by the transparent white vertical bars, and plotting binned intensity for the range of rows the entire fiber array illuminated. This method of binning reduced the amount of background noise present in the line-out. The peaks in the resulting line-out in Figure 4.4b represent each fiber in the array. The exact pixels that each fiber illuminated was determined by taking the full-width, half-maximum (FWHM) of each peak, where the half-maximum was defined as the mid-point between the maximum individual peak intensity and the average of the two local minima on either side of each peak. For the first and last fiber, only the single local minimum separating that fiber from the adjacent fiber was used. This process was repeated for many spectral images covering the full visible spectrum wavelength range and an average mapping of fiber number to iCCD pixel row range was estimated.

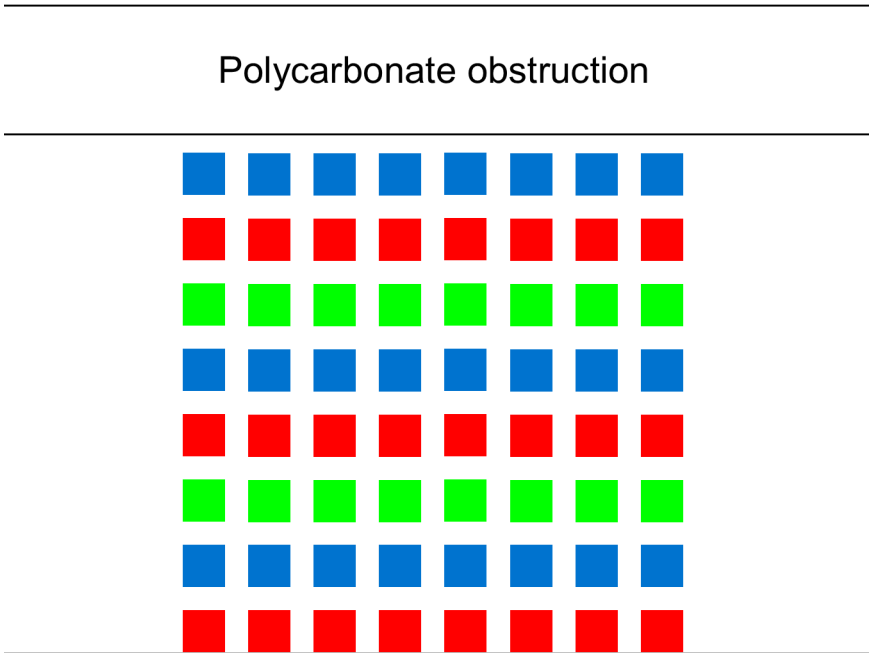

Figure 4.6: Top-down view schematic of 8×8 LED array used to map the fiber-optic bundle viewing chord within the chamber showing the color sequence used during characterization

In the second step, that range of pixel rows representing each fiber was mapped to a z-axis position range using an 8x8 array of programmable LEDs. Figure 4.5 is a photograph of this array during one such characterization and Figure 4.6 shows a top-down schematic of the LED array position relative to the polycarbonate obstruction and the color sequence used during characterization. All pixels in each row were programmed to a single color and the color of each row was alternated between red, green, and blue. By moving the LED array along the z-axis while viewing a live image of the spectral output, it could clearly be seen when each LED row illuminated the fiber most intensely, representing the location along the z-axis where the LED array was aligned with the center of that fiber's viewing chord. The distance between the LED and the polycarbonate was then measured. This was repeated for each fiber in the bundle and the results were used to calculate the distance between each fiber center's intersection with the z-axis.

Table 4.1 shows the results of this analysis. For both polycarbonate obstruction positions,

listed is the position along the bore-sight axis that illuminated each fiber. Note that for the 12 cm case (see Sec. 4.2 for explanation of the two obstruction position cases), only six fibers are listed. This is because after completing the experiments for that case, it was discovered that one of the fibers was not illuminated due to the positioning of the lens system. This problem was fixed and all seven fibers were properly illuminated for the 17 cm case.

Table 4.1: Spectrometer viewing chord by fiber along the bore-sight axis for both obstuction location cases

Obstruction position (cm)	Fiber number	Viewing chord z (cm)
12	1	11.49-11.82
	2	11.09-11.42
	3	10.68-11.01
	4	10.27-10.60
	5	9.87-10.20
	6	9.46-9.79
17	1	10.97-11.20
	2	10.69-10.92
	3	10.41-10.64
	4	10.13-10.36
	5	9.86-10.09
	6	9.58-9.81
	7	9.30-9.53

Finally, to have confidence that each fiber was being illuminated only by light within the z-axis range listed in Table 4.1, a characterization of cross-talk or bleed between adjacent fibers was conducted. This analysis was done by covering all but one of the rows in the 8×8 LED array with black electrical tape, such that only eight pixels, all of the same color, were exposed. Since the size of each individual LED (2×2 mm) is slightly smaller than the z-axis range illuminating each fiber (≈ 3.3 mm for the 12 cm obstruction case and ≈ 2.3 mm for the 17 cm case), when the row of LEDs is centered on a single fiber, that fiber should be the only one illuminated. If that is the case, and the adjacent fibers are not illuminated, the bleed is no greater than the difference in size between the LED side length and fiber z-axis

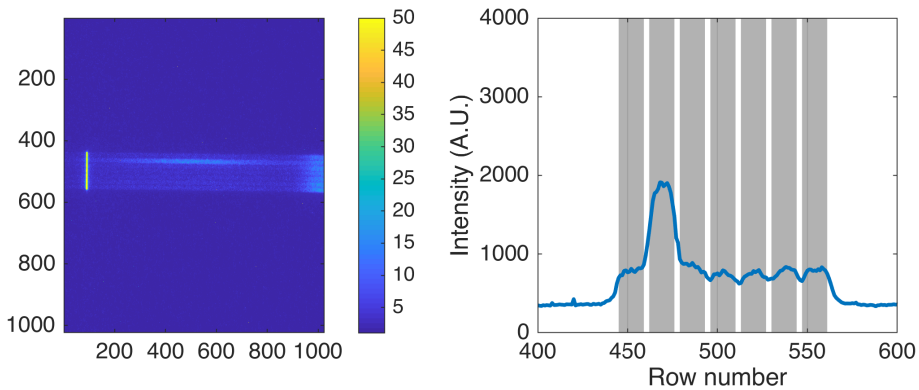

Figure 4.7: Spectral image of 8×8 LED array with just one row of LEDs exposed (left) and plot of binned intensity showing each fiber's CCD row coverage as gray vertical bars (right) used to characterize fiber-to-fiber cross-talk

coverage length.

Figure 4.7 shows a characteristic plot of that cross-talk analysis in which one row of blue LEDs was exposed and centered on the second fiber. Columns 200 - 800 were binned and a line-out of that binned intensity is shown in the figure on the right. Also shown in that line-out are gray transparent vertical bars that represent the CCD pixel rows illuminated by each fiber. The line-out shows that there is very little, if any, intensity above the typical background intensity for the two adjacent fibers to the one being purposefully illuminated. In this case, the cross-talk is sufficiently low such that the fiber array in this setup can be used to confidently obtain spatially-resolved spectral data in experiment.

4.2 Characterizing Jet Collisions

Jet collision experiments were conducted with the polycarbonate placed at $z = 12$ and $z = 17\,\text{cm}$. Each shot can be broken up into 5 components or stages: (S1) the first jet to leave the gun propagating unobstructed towards the polycarbonate, (S2) the stagnated jet or background plasma that is a result of the first jet colliding with the polycarbonate, (S3)

the second jet to leave the gun propagating unobstructed towards the polycarbonate before impacting the stagnated first jet, (S4) the collision between the second jet and stagnated first jet background plasma and any shock structure that forms as a result, and (S5) any time after the second jet/shock wave has impacted the polycarbonate. These five components will be referenced to clarify the analysis and discussion to follow. Note that not much analysis is done to S5, but it is defined here to clarify the end of S4.

For the two polycarbonate positions, a series of shots was first taken with the PIMAX iCCD camera mounted atop the vacuum chamber viewing perpendicular to the bore-sight axis. These shots were used to qualitatively observe the collision and any shock-structures produced, as well as to quantify the location along the z-axis and time of each component of the shot. After this, the iCCD camera was used with the high-resolution spectrometer, and the spectrometer lens was mounted atop the vacuum chamber and positioned to look at the area that would capture all five components of the shot. Figure 4.8 shows the top of the vacuum chamber for both configurations.

4.2.1 Shot Evolution and Geometry

Figures 4.9 and 4.10 show false-color, logarithm-scale images of jet evolution for both polycarbonate positions. A background image is also given to orient oneself and shows the location of the gun muzzle and polycarbonate as well as the position of interferometer chords which will be discussed in detail in Sec 4.2.3. The muzzle of the gun is at the bottom of the image and polycarbonate is at the top, so the jet is propagating upwards along the page. The location of the gun muzzle and polycarbonate is also shown with dashed white lines in all the plasma images.

These images show the first four jet components as detailed previously. Sub-figures (b) and

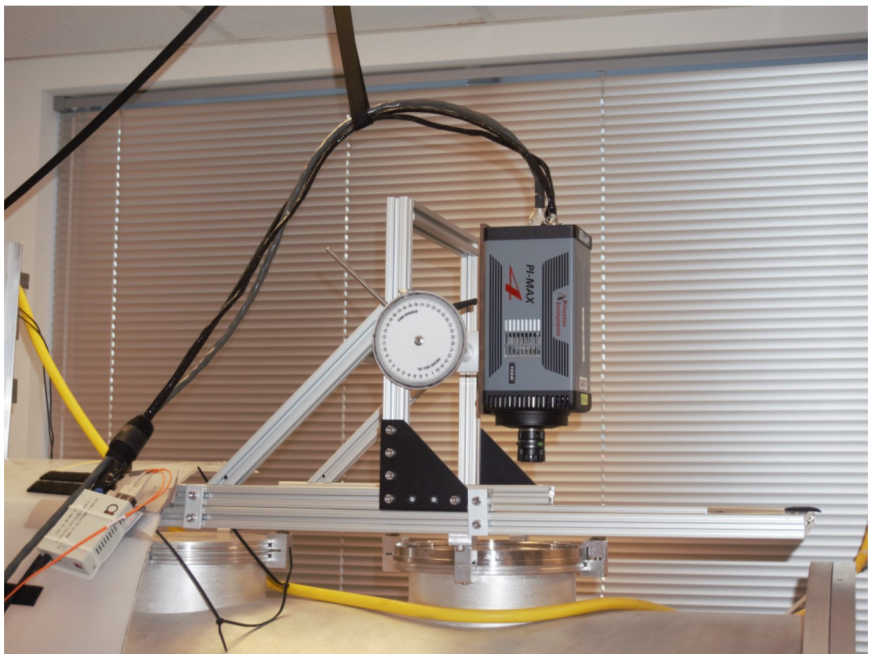

(a) iCCD camera

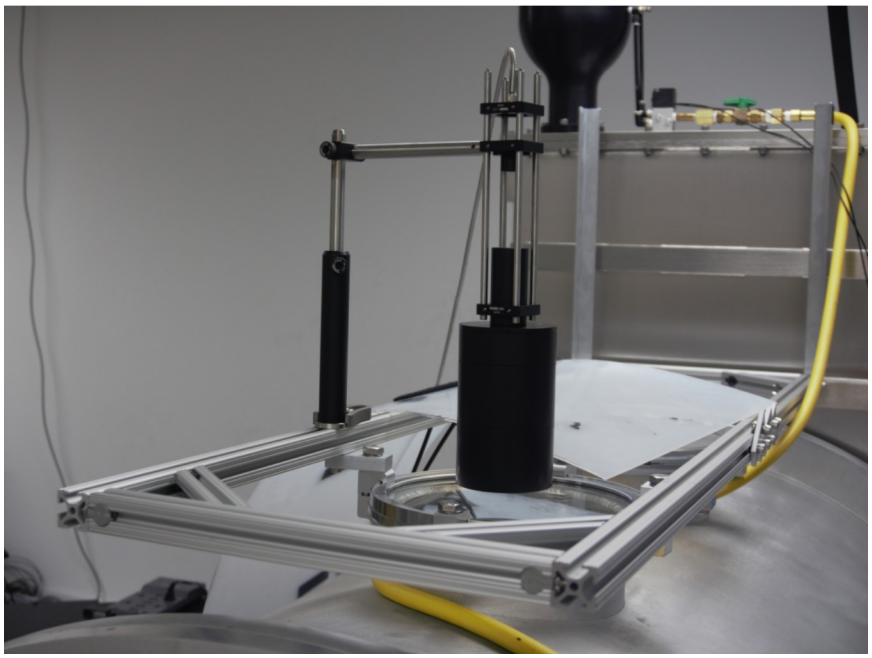

(b) Spectrometer lens

Figure 4.8: Photographs of the iCCD camera and spectrometer lens mounted atop the vacuum chamber for the obstructed jet experiments

(c) in both cases show stage (1), the unobstructed first jet propagating toward the polycarbonate. Sub-figures (d), (e), and (f) in each case shows the second and third component of the shot. The collision between the first jet and the polycarbonate occurs and one can see that stagnated background plasma expand slowly both radially and back towards the gun muzzle. At the same time, the second jet emerges from the gun and propagates towards the stagnated background plasma. Finally, sub-figures (g) and (h) show the 4th stage of the shot, where the second jet has collided with the stagnated first jet, producing a very bright curved "bow-shock-like" structure. This structure continues to propagate forward towards the polycarbonate and sub-figure (h) for both cases show the structure just before it collides with the polycarbonate.

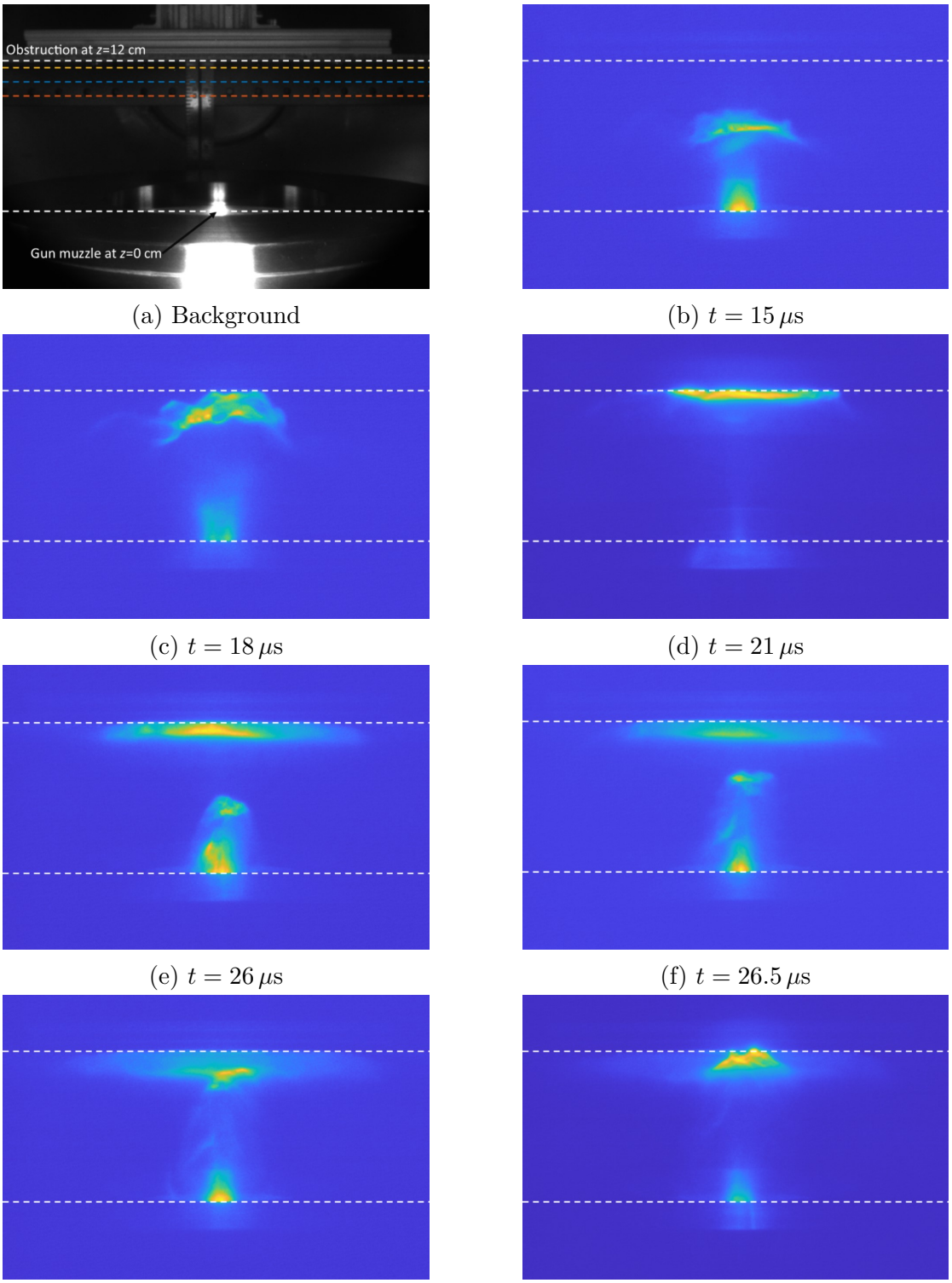

(a) Background (b) $t = 15\,\mu$s

(c) $t = 18\,\mu$s (d) $t = 21\,\mu$s

(e) $t = 26\,\mu$s (f) $t = 26.5\,\mu$s

(g) $t = 27\,\mu$s (h) $t = 27.5\,\mu$s

Figure 4.9: False color, 3 ns gate time, logarithm-scale images showing the progression of a shot when the polycarbonate obstruction was placed at $z = 12$ cm; shots numbers for (b) through (h) are 915, 917, 920, 925, 927, 928, and 931, respectively

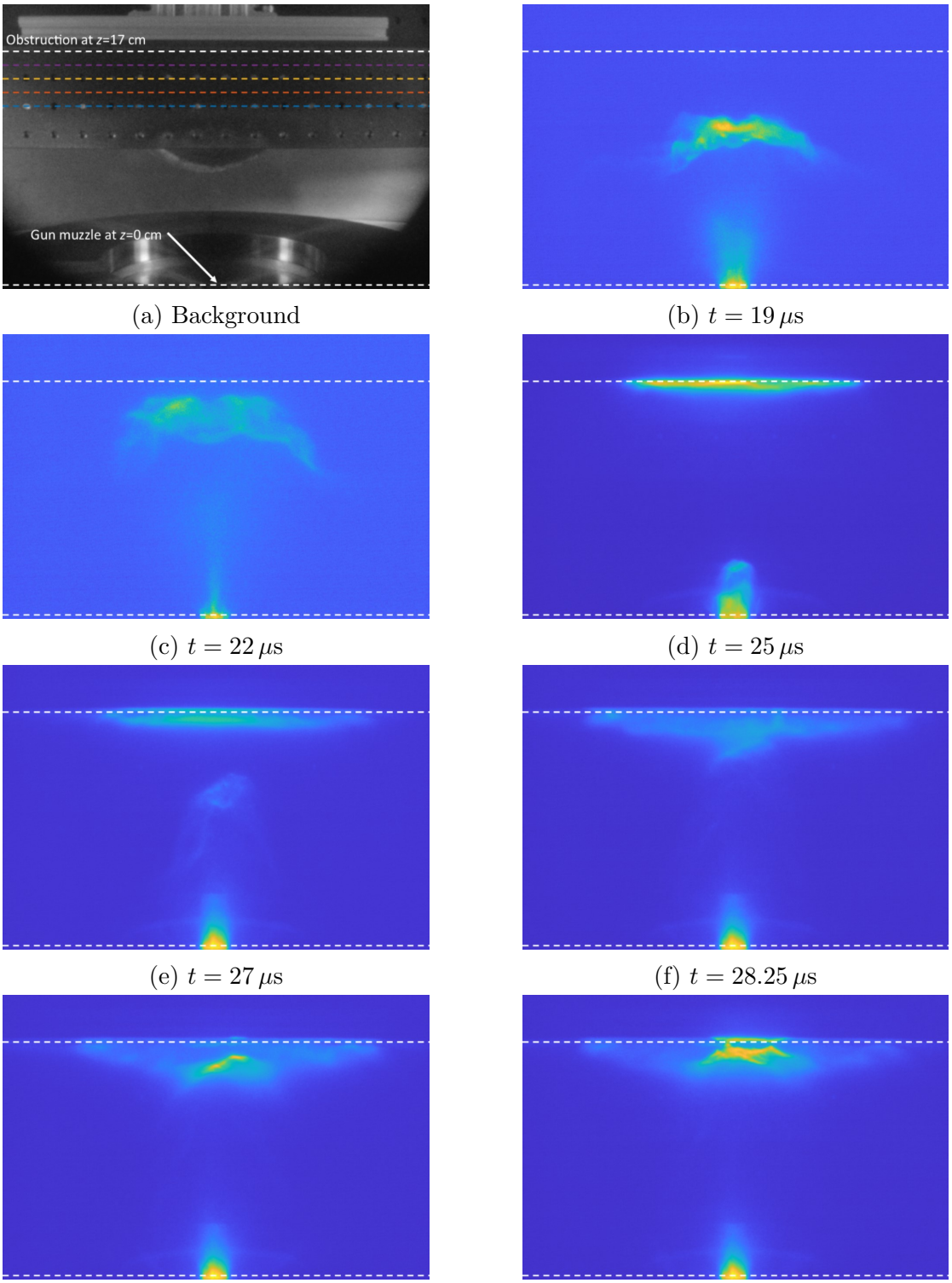

(a) Background (b) $t = 19\,\mu s$

(c) $t = 22\,\mu s$ (d) $t = 25\,\mu s$

(e) $t = 27\,\mu s$ (f) $t = 28.25\,\mu s$

(g) $t = 28.5\,\mu s$ (h) $t = 28.75\,\mu s$

Figure 4.10: False color, 3 ns gate time, logarithm-scale images showing the progression of a shot when the polycarbonate obstruction was placed at $z = 17$ cm; shots numbers for (b) through (h) are 1082, 1085, 1088, 1095, 1098, 1097, and 1106, respectively

A lot can be learned by this qualitative observation of the jet evolution. First, it is evident that the second jet to emerge from the gun is much narrower than the first. Both jets, however, have a flat disk-like profile with the jet width being larger than the thickness. That second jet also appears to be moving with much higher velocity than the first jet. Consider figure 4.10, for example, where the first jet travels a significantly shorter distance in the three microseconds between sub-figures (b) and (c) than the second jet over just another quarter microsecond longer from sub-figures (d) to (f).

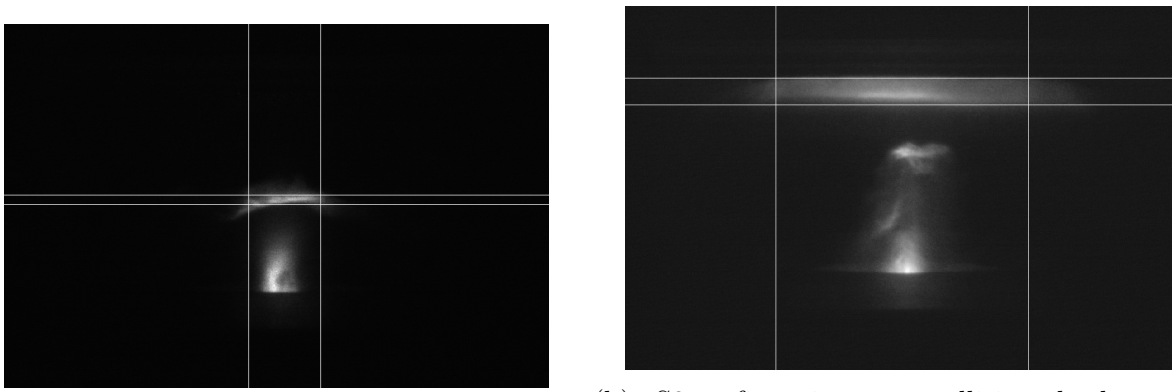

(a) S1: first jet pre-impact, shot 913

(b) S2: first jet post-collision background plasma, shot 927

Figure 4.11: Characteristic grayscale iCCD photographs used to estimate jet width and thickness for each image, white bars denote width and thickness

In order to quantify these observations of jet geometry, the images were analyzed to calculate jet thicknesses and widths as a function of z-axis position or time depending on the component of the shot. For S1, S3, and S4, the jet is traveling at a relatively high velocity along the z-axis; therefore, it makes sense to consider width and thickness as a function of z-axis position whereas the S2 background plasma moves much more slowly and its width and thickness as a function of z is constantly changing; therefore, it makes more sense to consider this stage as a function of time.

Figure 4.11 shows two representative images of this length estimation. Both images were taken with the iCCD in the same configuration as shown in Figures 4.9 and 4.10, top-down

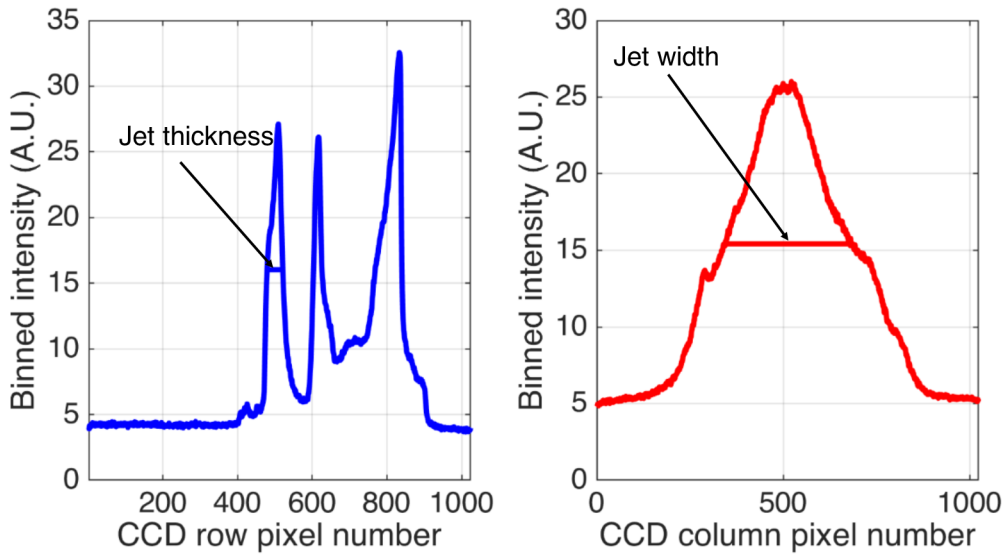

Figure 4.12: Line-outs used to calculate jet thickness (left) and jet width (right) for the first jet post-impact background plasma (S2) for shot 927 as shown in Figure 4.11b

with the railgun bore near the bottom of the image and the polycarbonate obstruction near the top. Jet widths and thicknesses were calculated in these images using the same method described in Sec. 3.3.3, described briefly again for clarity here. The white bars in each image represent the jet thickness and width estimated for that portion of the jet in the image shown. To infer jet thickness, the pixel column closest to the jet center was user-defined, then ten columns to the left and right of that column were binned and a line-out of that binned intensity was taken. The jet thickness estimate was then defined as the FWHM of the peak representing the background plasma in that line-out. The left plot in Figure 4.12 shows this line-out as well as the FWHM thickness calculated for shot 927, the same shot shown in Figure 4.11b. In order to then estimate jet width, the pixel rows contained within the jet thickness that was just inferred were binned and a line-out of that binned intensity was taken. Just as for the the jet thickness, the FWHM of this line-out was defined as the jet width, as shown in the right hand plot in Figure 4.12.

The results of this analysis for all iCCD images taken is shown in Figure 4.13. The scatter

plot points are data points from each iCCD image and a linear line of best fit is plotted on top. Each plot point was calculated using grayscale versions of the iCCD images. Similar to the method of mapping the optical fiber array to the CCD image discussed in Sec. 4.1.2, the thicknesses were calculated by plotting pixel intensity for the CCD column closest to the center of each jet stage and equating the jet thickness to the FWHM of that line-out. Jet width was then calculated by doing the same analysis, but for binned intensity for each row contained within the jet thickness.

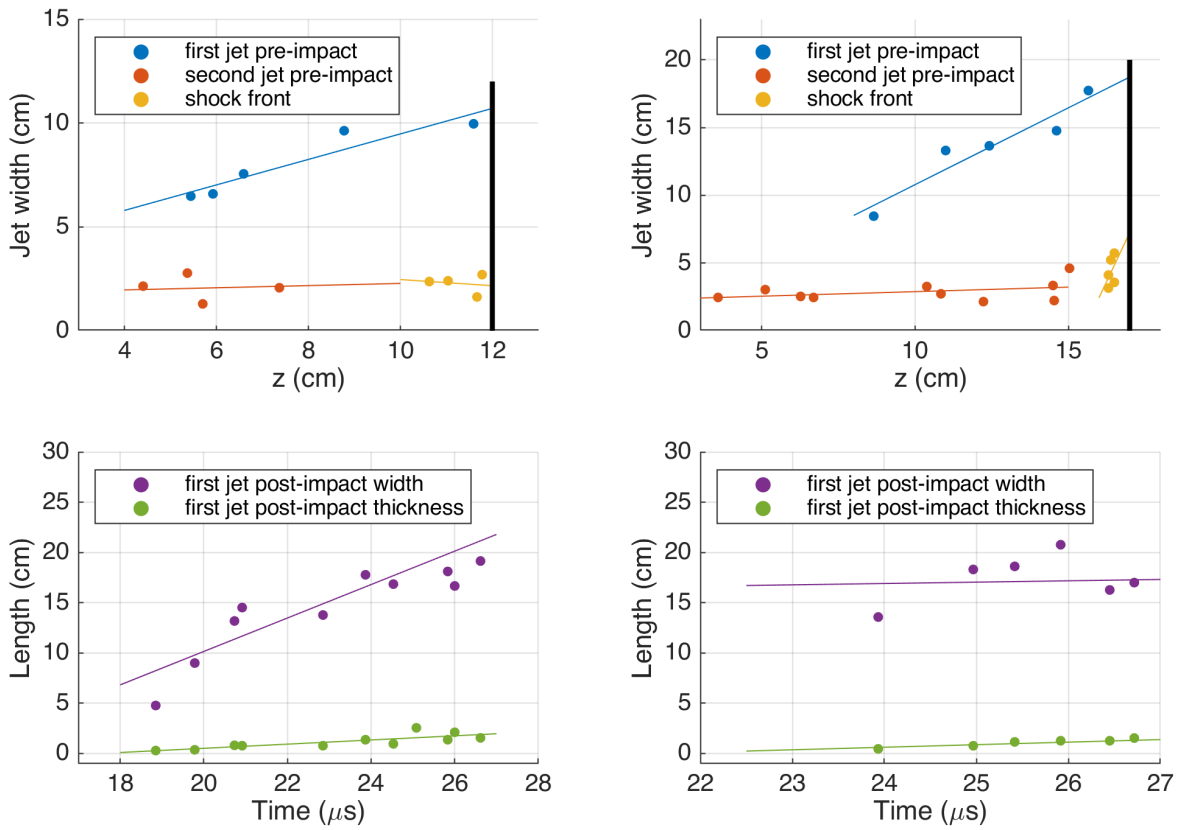

(a) PC at $z = 12\,\mathrm{cm}$ (b) PC at $z = 17\,\mathrm{cm}$

Figure 4.13: Scatter plot of jet widths and thicknesses as a function of z-axis position and time with trend-lines overlaid

4.2.2 Second Jet and Background Plasma Velocity

In Sec. 3.3.4, the velocity of the unobstructed first jet to leave the gun was estimated using the time of peak signal in interferometer traces at different chord intersection positions along the z-axis. Given the method of inducing jet collisions discussed in this chapter, estimating velocity of the unobstructed second jet to leave the gun as well as the velocity of the background plasma following the first jet's impact with the polycarbonate is necessary to calculate collision parameters and compare experimental results to those predicted by theory in later sections.

For the second jet, this estimation was obtained using a similar method described in Sec. 3.3.4, where the time of peak signal for interferometer traces at z-axis intersection distances of 10.2 and 20.3 cm was calculated and averaged, and that average peak signal time was used to calculate an average velocity for the second jet.

Figure 4.14 shows a zoomed-in plot of Figure 3.8a, the normalized average interferometer signal for the 10 kV PFN charge voltage case used in Chapter 3 to calculate velocity of the first jet. Labeled in the figure are the interferometer signal peaks due to the second jet to leave the gun. These peaks occurred at 27.2 μs for the 10.2 cm chord and at 30.5 μs for the 20.3 cm chord, resulting an average velocity for the second jet of 30.8 km/s.

For the background plasma, the z-direction velocity was inferred from iCCD images. A linear line of best fit to describe background jet thickness as a function of time was calculated using iCCD images and is shown in Figure 4.13. The slope of this best fit line in both the 12 and 17 cm obstruction location cases is used as the jet velocity estimate. For the 12 cm case, this corresponds to an average velocity of -2.1 km/s and for the 17 cm case, an average velocity of -2.5 km/s. The relative velocity between the two jets, therefore, is 32.9 km/s for the 12 cm case and 33.3 km/s for the 17 cm case.

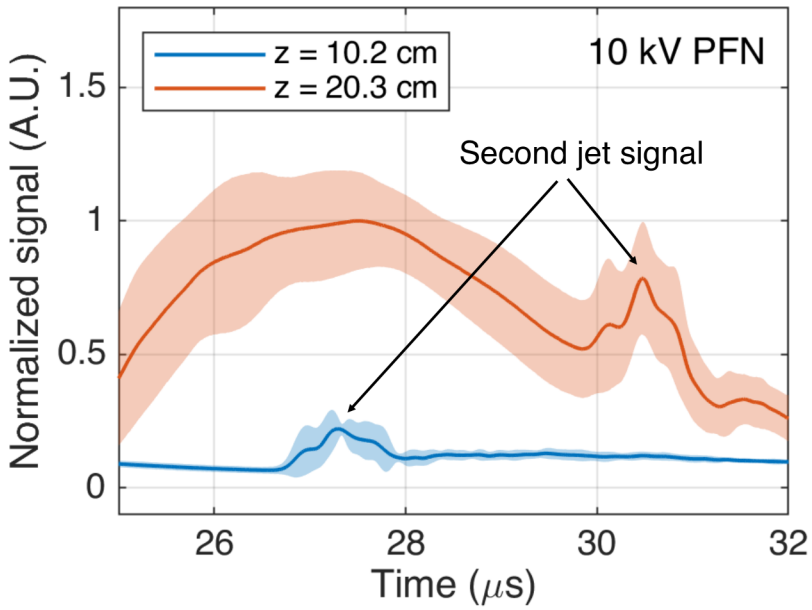

Figure 4.14: Zoomed in view of Figure 3.8a showing peaks due to second jet to leave the railgun.

4.2.3 Electron Number Density

While the bright event seen in the plasma images when the stagnated background plasma and second jet collide is certainly consistent with what would be expected of a shock-wave, the images alone are not proof of this. Interferometer traces provide more insight into the shot progression.

Figure 4.15 shows line-integrated electron number densities inferred from interferometer data at three locations along the z-axis. Sub-figure 4.15b plots the average line-integrated density with plus or minus one sigma standard deviation. Between ten and thirty shots were averaged for each bore-sight axis position. Sub-figure 4.15a shows each individual trace that was averaged to produced the average trace. Recall that the interferometer in this experiment is a two-chord diagnostic; therefore, all the traces shown were not taken for the same set of shots.

These three density traces can be segmented into the same five phases or components of the shot that the images were divided into, and the first four of these have been labeled in Figure 4.15b. Early in time, the first jet passes unobstructed by each chord. The shape of the peak of this first jet is very similar in each trace suggesting that the jet geometry and ionization state is not changing much as the jet travels past those z-axis locations. The time between the peaks is nearly constant, suggesting that the jet is traveling at a constant velocity. At about the 21 μs time the jet collides with the polycarbonate and the next rise that is seen in the $z = 11.4$ cm trace is the stagnated first jet that is slowly moving back towards the railgun's bore. This timing matches that which is seen in the iCCD images where it is also shown that the first jet impacts the polycarbonate at $t = 21\,\mu$s, as shown in Figure 4.9d. The large but more gradual increase in line-integrated density that follows is indicative of the jet expanding radially against the polycarbonate. A little further in time as the background plasma continues to expand, a similar rise occurs in the $z = 10.1$ cm chord.

In the $z = 8.8$ cm chord, however, there is no such rise; instead there is another sharper peak of lower amplitude but similar in structure to the first jet. This is the second jet to leave to gun, and since there was no gradual rise preceding its arrival, this is at a location where the second jet is still traveling unobstructed. Again, this matches what was observed in the iCCD images, as Fig 4.13a shows that the maximum distance away from the polycarbonate the stagnated background plasma is able to expand to before the second jet arrives is around 2 or 2.5 cm in front of the polycarbonate, as indicated by the "first jet post-impact thickness" data points. Finally, in the two chords closer to the polycarbonate a sharp peak is captured in both chords just after the second jet peak appears in the $z = 8.8$ cm chord. Notably, the amplitude of that peak in the blue and yellow traces appears even by eye to be quite a bit larger than the amplitude of the peak in the orange trace. If the plasma density was low such that the second jet simply passed through the background plasma without experiencing

many collisions, one would expect the jump in density measured by each chord to be about the same as that second jet passes. Since this does not appear to be the case, however, the larger amplitude spike indicates that when the second jet reaches the background plasma, it does collide, causing the particles to slow down as a result, leading to an increase in density and, since the jets have been shown to be traveling at high-Mach-number (see Sec. 3.3.4), potentially resulting in a shock-wave.

As with the iCCD images, a very similar jet progression is seen in the interferometer traces when the polycarbonate obstruction is placed at $z = 17\,\mathrm{cm}$, as shown in Figure 4.16. In this case, the $z = 13$ and $z = 14\,\mathrm{cm}$ chords capture the unobstructed second jet, the $z = 16\,\mathrm{cm}$ chord captures the structure that forms after the two jets have collided, and the $z = 15\,\mathrm{cm}$ chord appears to capture the position where the two jets just start to collide.

It is important to note that the x-axis time listed for each plot in Figures 4.15 and 4.16 is time relative to the initial rise in the PFN current pulse, which is defined as $t = 0$. Shot to shot jitter, therefore, affects the mean line-integrated density traces and standard deviation and may affect this qualitative description of the shot progression. So as not to influence this qualitative analysis by this jitter, Figures 4.15a and 4.16a show each individual trace that was averaged to produce the average traces. To quantify the rise in signal due to the expanding background plasma as compared with the rise due to the structure that forms after the two jets have collided, the respective slopes in each interferometer trace were calculated and averaged for the chord position closest to the polycarbonate for each obstruction location case. The rise for the expanding background plasma is $5.8 \times 10^{16} \pm 4.7 \times 10^{16}\,\mathrm{cm}^{-2}/\mu\mathrm{s}$ and $3.2 \times 10^{17} \pm 1.2 \times 10^{17}\,\mathrm{cm}^{-2}/\mu\mathrm{s}$ for the post-collision structure. Averaged over both obstruction location cases, the slope corresponding to the post-collision structure is on average 5.5 times greater than the slope corresponding to the expanding background plasma.

In order to estimate full electron number density, the linear lines of best fit calculated

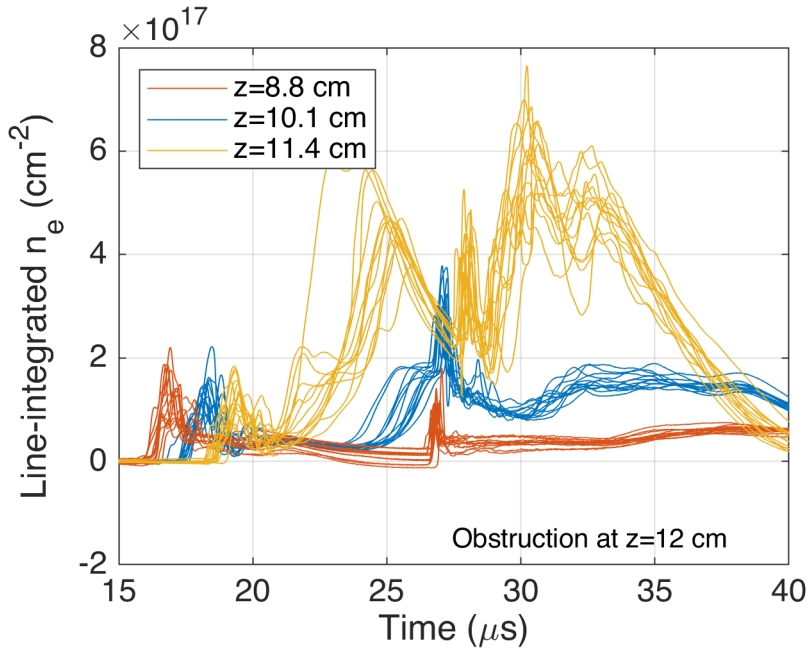

(a) Individual traces

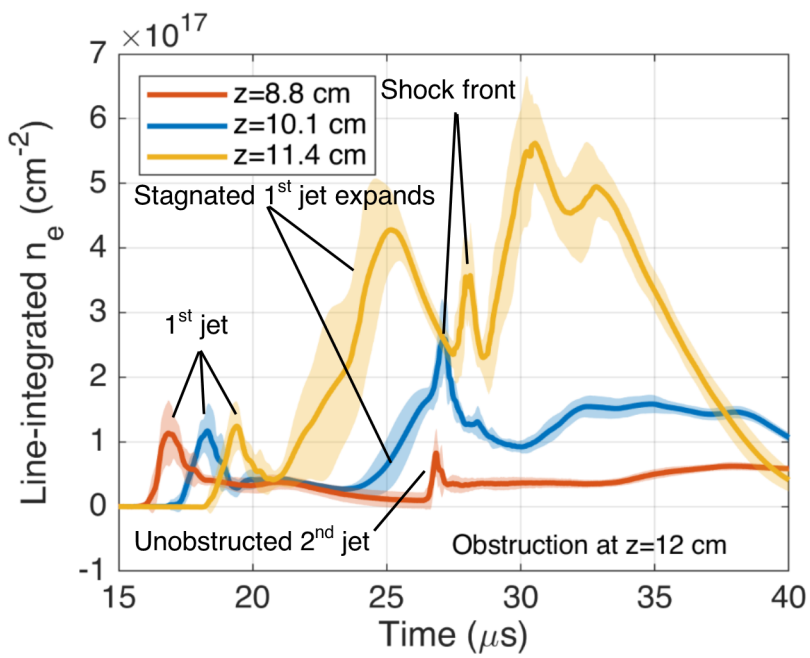

(b) Average trace ± one σ standard deviation

Figure 4.15: Line-integrated electron number density inferred from interferometer data for the case where the obstruction is mounted at $z = 12\,\mathrm{cm}$

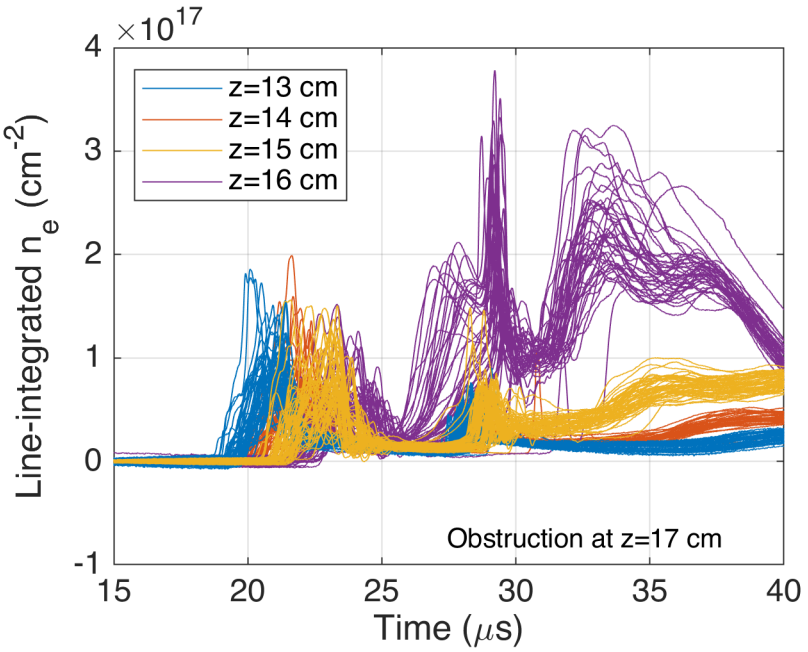

(a) Individual traces

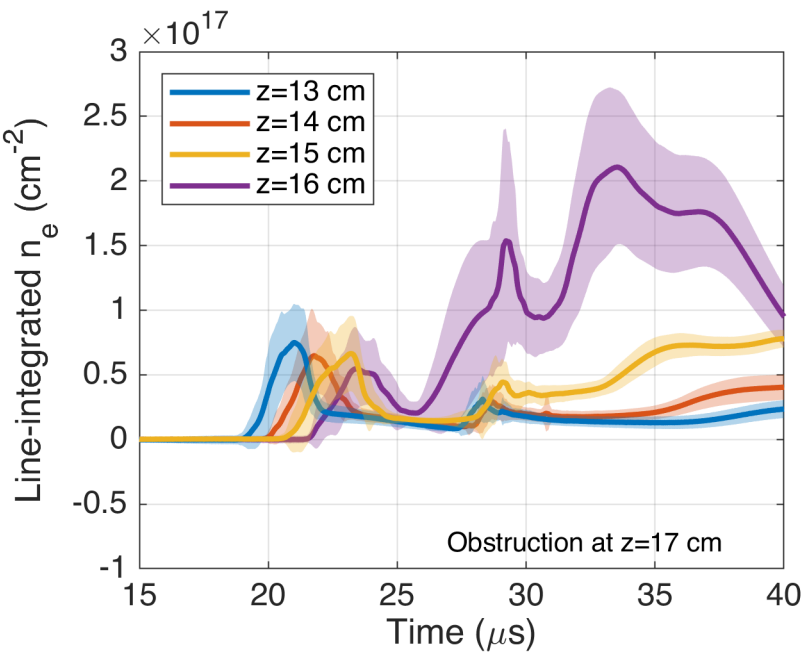

(b) Average trace ± one σ standard deviation

Figure 4.16: Line-integrated electron number density inferred from interferometer data for the case where the obstruction is mounted at $z = 17\,\mathrm{cm}$

from iCCD images and plotted in Figure 4.13 were used to convert line-integrated densities. Tables 4.2 and 4.3 present this analysis. Line-integrated density values for each component of the shot were taken for each individual shot and then averaged to obtain the value in the third column. For jet one, the density was estimated as the maximum value for the first peak in each chord's trace. The background density was measured at the point for each trace just before the sharp peak representative of either the second unobstructed jet or the shock-wave began, and the second jet or shock-wave density was estimated as the maximum value for that second sharp peak in each trace minus the background density. The full electron number densities were then calculated simply by dividing the line-integrated density by the jet width at that z-axis location and time.

Table 4.2: Full electron number densities for the $z = 12\,\mathrm{cm}$ obstruction case

Shot Phase	z (cm)	$n_e\ell$ (cm^{-2})	w (cm)	n_e (cm^{-3})
S1 (jet 1)	8.8	$1.47 \times 10^{17} \pm 4.1 \times 10^{16}$	8.7	$1.69 \times 10^{16} \pm 4.7 \times 10^{15}$
	10.1	$1.39 \times 10^{17} \pm 3.2 \times 10^{16}$	9.5	$1.46 \times 10^{16} \pm 3.4 \times 10^{16}$
	11.4	$1.38 \times 10^{17} \pm 3.2 \times 10^{16}$	10.3	$1.34 \times 10^{17} \pm 3.1 \times 10^{15}$
S2 (background)	8.8	$9.77 \times 10^{15} \pm 1.1 \times 10^{16}$	20.5	$4.77 \times 10^{14} \pm 5.4 \times 10^{14}$
	10.1	$1.72 \times 10^{17} \pm 8.7 \times 10^{15}$	20.9	$8.23 \times 10^{15} \pm 4.2 \times 10^{14}$
	11.4	$2.30 \times 10^{17} \pm 1.9 \times 10^{16}$	22.7	$1.01 \times 10^{16} \pm 8.4 \times 10^{14}$
S3 (jet 2)	8.8	$1.05 \times 10^{17} \pm 2.5 \times 10^{16}$	2.2	$4.78 \times 10^{16} \pm 1.1 \times 10^{16}$
	10.1			
	11.4			
S4 (merged jets)	8.8			
	10.1	$1.42 \times 10^{17} \pm 3.7 \times 10^{16}$	2.5	$5.68 \times 10^{16} \pm 1.5 \times 10^{16}$
	11.4	$1.98 \times 10^{17} \pm 5.1 \times 10^{16}$	2.3	$8.61 \times 10^{16} \pm 2.2 \times 10^{16}$

4.2.4 Temperature, Ionization, and Ion Density

Jet temperature and mean ionization, or $\bar{Z}$, which relates ion and electron number density by $n_i = n_e/\bar{Z}$, were calculated by comparing spectral data captured during experiment to

Table 4.3: Full electron number densities for the $z = 17\,\mathrm{cm}$ obstruction case

Shot Phase	z (cm)	$n_e\ell$ (cm^{-2})	w (cm)	n_e (cm^{-3})
S1 (jet 1)	13	$1.05 \times 10^{17} \pm 3.0 \times 10^{16}$	14.2	$7.39 \times 10^{15} \pm 2.1 \times 10^{15}$
	14	$1.15 \times 10^{17} \pm 3.5 \times 10^{16}$	15.3	$7.52 \times 10^{15} \pm 2.3 \times 10^{16}$
	15	$9.14 \times 10^{16} \pm 3.1 \times 10^{16}$	16.5	$5.54 \times 10^{15} \pm 1.9 \times 10^{15}$
	16	$1.07 \times 10^{17} \pm 2.4 \times 10^{16}$	17.6	$6.08 \times 10^{15} \pm 1.4 \times 10^{15}$
S2 (background)	13	$8.41 \times 10^{15} \pm 1.5 \times 10^{15}$	17.4	$4.83 \times 10^{14} \pm 8.6 \times 10^{13}$
	14	$1.08 \times 10^{16} \pm 1.3 \times 10^{15}$	17.4	$6.21 \times 10^{14} \pm 7.5 \times 10^{13}$
	15	$1.86 \times 10^{16} \pm 1.0 \times 10^{16}$	17.5	$1.06 \times 10^{15} \pm 5.7 \times 10^{14}$
	16	$1.53 \times 10^{17} \pm 1.8 \times 10^{16}$	17.5	$8.72 \times 10^{15} \pm 1.0 \times 10^{15}$
S3 (jet 2)	13	$4.48 \times 10^{16} \pm 1.2 \times 10^{16}$	3.1	$1.45 \times 10^{16} \pm 3.9 \times 10^{15}$
	14	$3.66 \times 10^{16} \pm 8.4 \times 10^{15}$	3.2	$1.14 \times 10^{16} \pm 2.6 \times 10^{15}$
	15	$5.21 \times 10^{16} \pm 1.9 \times 10^{16}$	3.2	$1.63 \times 10^{16} \pm 5.9 \times 10^{15}$
	16			
S4 (merged jets)	13			
	14			
	15			
	16	$1.47 \times 10^{17} \pm 3.7 \times 10^{16}$	3.3	$4.45 \times 10^{16} \pm 1.1 \times 10^{16}$

spectra simulated using PrismSPECT [39]. PrismSPECT is a software that allows the user to set plasma parameters including ion density, temperature, and plasma species composition, and will then calculate the spectrum that a plasma with those parameters is expected to produce as well as the expected mean ionization state. By comparing an experimentally obtained spectrum to one or a set of simulated spectra, this software can be used to help infer plasma parameter values that are difficult to estimate based on experimental data alone. For the railgun experimental apparatus and diagnostic suite, temperature and ionization fraction are two of these parameters that are difficult to estimate. Recall that in Sec. 3.3.2, plasma temperature in the unobstructed jets was inferred using the so-called "ratio method" which required a number of assumptions to be made about the plasma. At the time, this method provided an estimate for average plasma temperature that was adequate for making initial approximations of collisions parameters. Similarly, mean ionization state was

approximated as unity for the estimations of collision parameters done in Sec. 3.3.5 based on the ionization fraction measured in other accelerated plasma-jets with similar parameters [28, 29, 30]. For this experimental campaign, however, more precise estimations are necessary for understanding and evaluating jet collisions.

To estimate plasma temperature and mean ionization fraction using PrismSPECT, an iterative method [25] was used to obtain a range of potential plasma temperatures and associated $\bar{Z}$ estimates. This method is performed as follows: (1) a single ion number density is chosen, and PrismSPECT simulations are run using that density for a range of temperatures; (2) the set of simulated spectrograms is compared to experimental data and temperatures are ruled out based on either the presence of a spectral line in the experimental data that does not appear in all simulated spectrograms or the absence of a spectral line in experimental data that does appear in some of the simulated spectrograms; (3) the average $\bar{Z}$ predicted by PrismSPECT for the remaining range of potential temperature values is used to recalculate ion number density and these steps are repeated until the ion number density used to run the simulation comes close to matching the ion number density calculated at the end of the simulations based on the simulated $\bar{Z}$. In practice, this method required three or four iterations before this condition was met.

In estimating temperature and ionization fraction for the stagnated first jet background plasma, incoming pre-collision second jet, and post-collision plasma, $\bar{Z}$ was always chosen to be unity initially so the value of ion number density set in PrismSPECT for the first set of simulations was equal to the electron number density estimated and shown in Tables 4.2 and 4.3. A range of temperatures at 0.2 eV intervals were chosen to simulate for that single density.

Recall from Sec 3.3.1 that jet composition was estimated to be approximately 50 % argon, 50 % impurities. Using that estimation, plasma composition set in PrismSPECT was 50 %

Ar, 25 % PEEK plastic (gun housing material, $C_{19}H_{12}O_3$) and 25 % gun insulating ceramic (50 % BN and 50 % AlN) by molar fraction. Table 4.4 lists the molar percentage of the jet for each of these elements. Note that although some copper spectral lines have been observed in experimental data, the copper and tungsten composing the railgun's electrodes were not included in the simulation simply because the software license purchased only included atomic models for elements with atomic weight up to and including $Z = 18$(argon). Additionally, a low-temperature atomic model for each element was used in PrismSPECT and simulations were all steady-state, non-local thermodynamic equilibrium (LTE) calculations with a single-Maxwellian electron distribution.

Table 4.4: Jet composition by molar fraction used in PrismSPECT simulations

Element	Molar percentage of jet
Ar	50 %
C	14 %
N	12.5 %
H	8.8 %
B	6.25 %
Al	6.25 %
O	2.2 %

Experimental spectral data used to compare to simulations was collected using the high-resolution imaging spectrograph with the fiber-optic bundle containing seven fibers in an linear array aligned such that each fiber intersected the bore-sight axis at a 90° angle, as described in Sec. 4.1.2. The 300 g/mm grating was used for all shots; therefore, the iCCD sensor collected light within a wavelength range of ≈ 55 nm. Data was collected where the center wavelength of the spectrometer was set to either 350 nm or 460 nm, corresponding to the two wavelength ranges where the most singly- and doubly-ionized argon lines as well as the greatest variety of spectral lines from impurities appeared. A spectrometer entrance slit width of between 10 and 50 μm was used for all shots, and the gate width of the PIMAX

iCCD was between 50 and 200 ns.

Based on the iCCD images and measured jet positions as a function of time and z-axis position as shown in Figure 4.13, spectral images were sorted by fiber and gate time into the five distinct phases of the shot. For example, for the 12 cm case, Figure 4.13a shows that the time after the first jet has impacted the polycarbonate but before the second jet has arrived is between about 18 and 26.5 μs and the furthest away from the polycarbonate that the stagnated plasma has reached on average at the time the second jet arrives is about 1.8 cm in front of the polycarbonate, or $z = 10.2$ cm. By the results listed in Tab. 4.1, this position is measured by fibers one through 4; therefore, to construct an average spectral plot for the stagnated background plasma for the 12 cm case, only shots where the gate time fell between 18 and 26.5 μs were considered, and for those shots the intensities of the CCD were binned only for the pixels that corresponded to the first four fibers. The end result of this process was a single spectrogram to be compared to PrismSPECT simulation results.

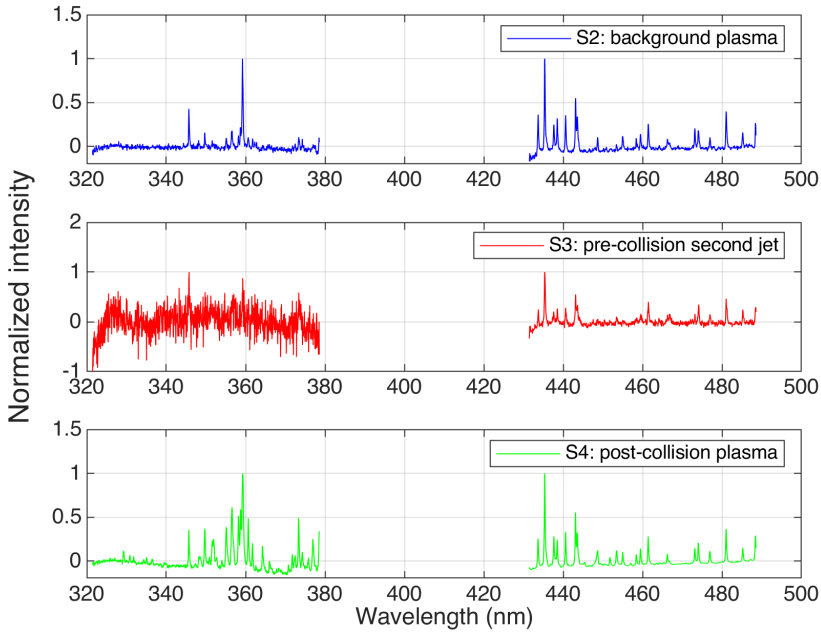

(a) 12 cm obstruction case

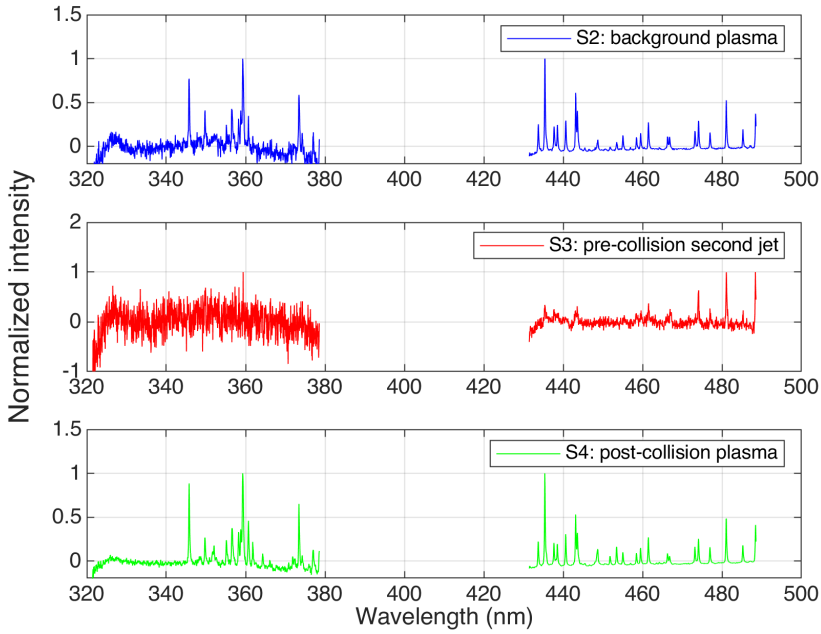

(b) 17 cm obstruction case

Figure 4.17: Normalized average measured spectra for the stagnated first jet background plasma, pre-collision second jet plasma, and post-collision plasma used to compare to Prism-SPECT simulation results to estimate plasma temperature and $\bar{Z}$

Figure 4.17 shows these spectrograms for each polycarbonate obstruction location and each shot phase for which temperature and mean ionization state were estimated. Note that spectral intensity is normalized for this data set since each average spectrogram was not estimated using the same number of shots or with data all using the same slit widths and iCCD gate widths; therefore, comparison of spectral intensity from one shot phase to another or even between the 350 nm and 460 nm center wavelength spectrograms cannot be used to quantify the jets. A few qualitative observations can, however, help interpret or suggest what might be expected from the comparison to simulated spectra. Spectral lines from singly-ionized argon are most present in the mid to high-400 nm wavelength range, whereas doubly-ionized argon lines are more prominent in the mid-300 nm range. Based on the number of spectral lines observed within each range for each jet phase in Figure 4.17, the post-collision plasma appears to contain the most spectral lines in the mid-300 nm range in both polycarbonate obstruction cases, suggesting that the mean ionization state could be higher for that phase than for the other two. If a shock-wave formed when the two jets collide, the expectation would be that ionization fraction would increase due to the shock-wave-induced heating. Note that this qualitative comparison of line emission is not a direct indication of temperature or ionization, as the number of lines of a given species that appear in the spectrum does not correlate to either of those quantities. Line emission occurs when an an excited electron returns to a lower-energy state, releasing a photon at a discrete wavelength with energy equal to the difference between the two states. The qualitative analysis presented for these spectrograms, therefore, is not a definitive result but simply a hypothesis to be either confirmed or refuted through quantitative analysis of line-emission using PrismSPECT.

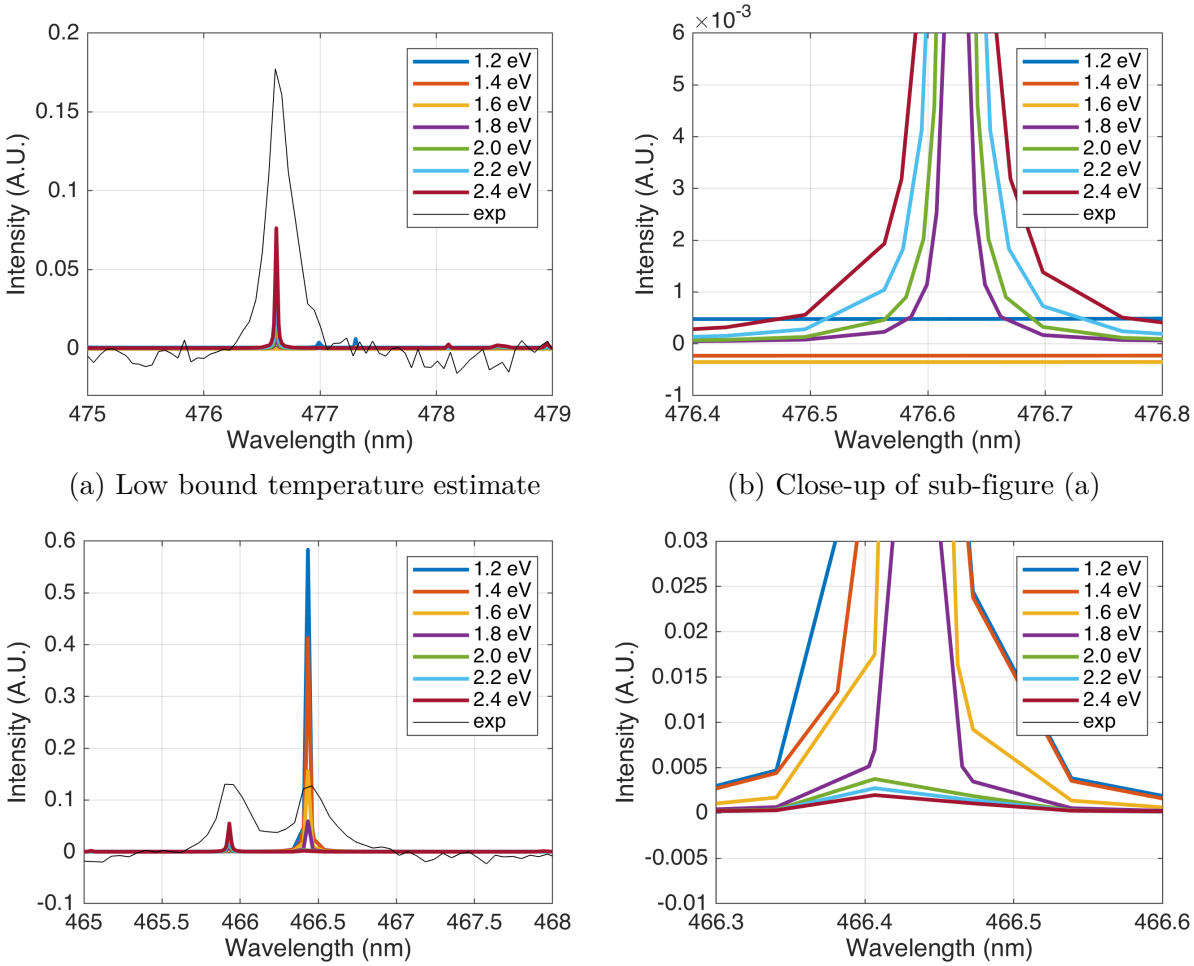

(a) Low bound temperature estimate

(b) Close-up of sub-figure (a)

(c) Upper bound temperature estimate

(d) Close-up of sub-figure (b)

Figure 4.18: Comparison of the average spectrum captured during experiment for the stagnated background plasma for the 17 cm polycarbonate obstruction location and PrismSPECT simulated spectra used to estimate plasma temperature and ionization

Figure 4.18 shows a set of plots comparing the average experimentally-observed spectrum for the stagnated background plasma when the polycarbonate was positioned at 17 cm to a set of spectra simulated using PrismSPECT for an array of plasma temperatures and with density equal to the average ion density estimated for the 16 cm interferometer chord position. The comparison shown is the last iteration of the estimation for this case, where the ion density used for the simulations matched the ion density calculated based on the

ionization state corresponding to the average of the lower and upper bound temperature estimation. This figure is a representative set of plots meant to clarify the method used to obtain a range for temperature and mean ionization state for each segment of the shot as discussed previously in this section. Sub-figures 4.18a and 4.18b show a spectral line from singly-ionized argon that is present in the experimentally-observed spectrum. When compared with the simulated spectra, however, this same line only appears for temperatures above 1.6 eV. As a result, the temperature of the plasma for this case is estimated to be greater than 1.6 eV. In sub-figures 4.18c and 4.18d, a similar comparison is done with a line from singly-ionized aluminum that appears in the measured spectrum. This line only appears in the simulated spectra where temperature is below 2.0 eV. Therefore, for this case, the electron temperature of the stagnated background plasma is estimated as $1.6 < T_e < 2.0$ eV.

Table 4.5: Densities, temperature, and $\bar{Z}$ inferred from PrismSPECT simulations for the 12 cm obstruction case

Shot Phase	z (cm)	n_e (cm^{-3})	T (eV)	$\bar{Z}$	n_i (cm^{-3})
S2 (background)	10.1	8.2×10^{15}	2.2 - 2.8	1.4 - 1.9	5.9×10^{15} - 4.3×10^{15}
	11.4	1.0×10^{16}	2.2 - 2.8	1.4 - 1.9	5.3×10^{15} - 7.1×10^{15}
S3 (jet 2)	8.8	4.8×10^{16}	1.4 - 1.6	0.9 - 1.0	4.8×10^{16} - 5.3×10^{16}
	10.1				4.1×10^{16} - 4.4×10^{16}
	11.4				3.0×10^{16} - 3.3×10^{16}
S4 (shock)	10.1	5.7×10^{16}	2.6 - 2.8	1.8 - 1.9	3.0×10^{16} - 3.2×10^{16}
	11.4	8.6×10^{16}	2.6 - 2.8	1.7 - 1.9	4.5×10^{16} - 5.1×10^{16}

Tables 4.5 and 4.6 present the results of the analysis to determine plasma temperature and $\bar{Z}$ by comparing the measured spectra in Figure 4.17 to spectra simulated in PrismSPECT as well as the full ion number density for each phase of the shot based on that inferred ionization fraction. Note that the second jet densities at the z-axis chord positions where the second jet was no longer expected to be traveling unobstructed were inferred using density from the 8.8 cm and 14 cm chord positions for the 12 and 15 cm polycarbonate obstruction cases

Table 4.6: Densities, temperature, and $\bar{Z}$ inferred from PrismSPECT simulations for the 17 cm obstruction case

Shot Phase	z (cm)	n_e (cm^{-3})	T (eV)	$\bar{Z}$	n_i (cm^{-3})
S2 (background)	15	1.1×10^{15}	1.4 - 1.8	1.0 - 1.1	1.0×10^{15} - 1.1×10^{15}
	16	8.7×10^{15}	1.6 - 2.0	1.0 - 1.2	7.3×10^{15} - 8.7×10^{15}
S3 (jet 2)	14	1.1×10^{16}	1.0 - 1.6	0.3 - 1.0	1.1×10^{16} - 3.7×10^{16}
	15				1.0×10^{16} - 3.4×10^{16}
	16				8.5×10^{15} - 2.8×10^{16}
S4 (shock)	16	4.5×10^{16}	2.6 - 2.8	1.8 - 1.9	2.4×10^{16} - 2.5×10^{16}

respectively, using the same semi-analytic prediction model that was shown to match the free expansion of the unobstructed jets in Sec. 3.3.3.

In both polycarbonate obstruction cases, the temperature and mean ionization inferred for the plasma after the collisions has occurred is greater than either the background plasma or unobstructed second jet. This findings support the hypothesis that something more than just jet interpenetration is occurring when the two jets collide, as this heating and increased ionization would not be expected if that were the case. Next compare the ion density for the three shot phases at the z-axis chord position closest to the polycarbonate, $z = 11.4$ cm for the $z = 12$ cm obstruction position case and $z = 16$ cm for the $z = 17$ cm case. At this location the stagnated first jet background plasma ion density is greatest. If the second jet passed through the background plasma at this z-axis position without experiencing many inter-jet collisions, the peak ion density magnitude would be no greater than the sum of the background density and unobstructed second jet ion density just before that jets merged. On the other hand, if the merging between the two jets did slow down and compress the incoming second jet or produce a shock-wave, one would expect the density at that location to be greater than that summation. Table 4.7 compares ion densities for both polycarbonate obstruction locations and shows the ratio of the density of the shock and the density expected if the two jets were experiencing interpenetration.

For the 12 cm obstruction case, even using the lower bound ion density for the merged jet and upper bound density for the summation results in a ratio greater than unity. This result is strong evidence that a shock-wave is produced for that case. For the 17 cm obstruction case, however, the result is more unclear. The range of ratios, which is much larger than the range estimated for the 12 cm case, varies from what would be expected of jet interpenetration to that expected of a strong shock-wave. This larger variation is most likely due to the decreased signal to noise ratio in both the interferometer and high-resolution spectrometer diagnostics when probing the plasma far away from the gun muzzle where features are less dense and bright. As a result, while the increase in temperature and $\bar{Z}$ for this case suggests that there is collisionality between the two jets and possibly a shock-wave, there is not enough evidence to definitively say a shock-wave is produced for the 17 cm case.

Table 4.7: Comparing ion number density calculations against that expected for interpenetration

z_{PC} (cm)	12	17
$z_{measured}$ (cm)	11.4	16.0
$n_{background}$ (cm^{-3})	5.3×10^{15} - 7.1×10^{15}	7.3×10^{15} - 8.7×10^{15}
n_{jet2} (cm^{-3})	3.0×10^{16} - 3.3×10^{16}	8.5×10^{15} - 2.8×10^{16}
n_{shock} (cm^{-3})	4.5×10^{16} - 5.1×10^{16}	2.4×10^{16} - 2.5×10^{16}
$n_{shock}/(n_{background} + n_{jet2})$	1.1 - 1.4	0.7 - 1.6

4.2.5 Estimates of Thermal Equilibration Time

Up to this point in the analysis, estimates of electron temperature determined with PrismSPECT have been used to help understand the structures that form during jet collisions. In the following sections, these plasma parameters will be used to estimate jet collisionality and determine whether the experimental apparatus and setup is conducive to the study of shock-wave-induced ion species distribution. In those estimates, it is ion temperature as

opposed to electron temperature that affects potential separation. If $T_e \approx T_i$, the jet electron temperatures estimated in Sec. 4.2.4 can be used as a reasonable approximation of ion temperature in those calculations. To assess whether this is the case, the ion-electron equilibration time is estimated for the pre-collision second jet and stagnated first jet background plasma. Thermal equilibration time, τ_{eq} is given by [30, 37]

$$\tau_{eq} = \frac{\bar{\mu} T_e^{3/2}}{3.2 \times 10^9 n_e \bar{Z}^2 \lambda_{ie}} \tag{4.1}$$

where $\bar{\mu}$ is the weighted average ratio of ion to proton mass in the plasma and λ_{ie} is the Coulomb logarithm for ion-electron collisions, which is given by [37]

$$\lambda_{ie} = 23 - \ln(n_e^{1/2} \bar{Z} T_e^{-3/2}). \tag{4.2}$$

τ_{eq} was calculated given the range of temperatures and ionization states listed in Tables 4.5 and 4.6 for the stagnated first jet and pre-collision second jet cases at the $z = 11.4$ and $z = 16$ cm chord positions for the 12 and 17 cm polycarbonate obstruction cases, respectively. $\bar{\mu} = 26.2$ was used for all calculations, calculated given the jet composition listed in Tab 4.4. The estimated thermal equilibration times are given in Tab. 4.8. In all cases, the estimated values for τeq are small as compared to the time-of-flight of the second jet before colliding with the background plasma and the time between the first jet impacting the polycarbonate and being impacted by the incoming second jet. Since this is the case, assuming $T_e \approx T_i$ is a reasonable approximation for the purposes of estimating collision parameters and potential species separation distances.

Table 4.8: Thermal equilibration times

z_{PC} (cm)	12	17
S2 (background plasma)	0.12 - 0.15 μs	0.34 - 0.36 μs
S3 (pre-collision jet 2)	0.12 μs	0.37 - 1.8 μs

4.2.6 Collisionality Estimates and Comparison to Theory

In order to gain additional insight into any shock-structures that form during jet collisions, simple one-dimensional hydrodynamic theory can be used to compare the expected density jump for a normal shock-wave to the density jump measured experimentally. The theoretically predicted ratio between post-shock plasma density, n_2, and pre-shock density, n_1 is given by the Rankine-Hugoniot equation [40] as

$$\frac{n_2}{n_1} = \frac{M^2(\gamma+1)}{M^2(\gamma-1)+2} \tag{4.3}$$

where M is the Mach number and γ is the specific heat ratio. Based on analysis performed in Sec. 4.2.2, relative velocity between the two jets when the collision occurs is $\approx 33\,\mathrm{km/s}$ for both polycarbonate obstruction locations. At this velocity Mach number given by Equation 3.4 can be estimated using $\bar{Z} = 0.9 - 1.0$ and $T = 1.4 - 1.6\,\mathrm{eV}$ for the 12 cm case and $\bar{Z} = 0.3 - 1.0$ and $T = 1.0 - 1.6\,\mathrm{eV}$ for the 17 cm case from Tables 4.5 and 4.6. Mach number given these parameters ranges from 10.6 to 11.9 for the 12 cm case and from 10.6 to 24.4 for the 17 cm case, corresponding to a theoretical density ratio of $n_2/n_1 = 3.88 - 3.90$ and $n_2/n_1 = 3.88 - 3.97$, respectively. In experiment, the ratio of densities, which is estimated as the ratio of the post-shock ion density to the average ion density between the stagnated background plasma and incoming second jet just before the collision ranges from 2.2 to 2.8 for the 12 cm obstruction case and from 1.4 to 3.2 for the 17 cm. In both cases the 1D hydrodynamic prediction is greater than the experimental result. This is somewhat to be

expected [29] as in the three-dimensional geometry of the experiment, material escapes the shock interface radially, leading to a weaker shock than is predicted by 1D theory.

In order to assess whether the experimental setup and apparatus presented here is conducive to the study of shock-wave induced ion species separation, the ion-ion collision rate and ion penetration lengths for different ion species in the pre-collision second jet impacting the stagnated background plasma are estimated using equations 3.5 and 3.7. Recall that the ion penetration length is expected to be on the order of the shock thickness [29]. Ion-ion collision frequency was calculated for collisions between hydrogen, carbon, and argon in the second jet counterstreaming and colliding with the average atomic weight ion species in the stagnated background plasma. Collision parameters for these three ions were calculated because of the large variation in their atomic weights, and their presence in the experimental spectral data. These theoretical values for ion penetration length are listed in Table 4.9. Also shown in Table 4.9 is the average thickness of the structure observed in fast-camera images when the collision occurs for both obstruction locations. This thickness was calculated using the same method used to calculate jet width and thickness discussed in Sec. 3.3.3.

For the 12 cm case, the observed collision structure thickness is close to the theoretical value of penetration length for argon for that case. For the 17 cm case, the observed structure thickness is very similar to that observed in the 12 cm case, which is in between the theoretical penetration lengths for argon and carbon for that obstruction location. In both obstruction location cases, the difference in the theoretical ion penetration lengths between hydrogen, carbon, and argon is on the order of millimeters. For the 12 cm obstruction case, where evidence suggested the probably formation of a shock-wave during the collision, this result suggests that separation between the hydrogen and argon on the order of half a centimeter or greater could be induced. If this is the case, this length scale is large enough to be detected with the diagnostics currently available.

Table 4.9: Comparison of experimental collision structure thickness and theoretical ion penetration lengths

z_{PC} (cm)	12	17
Shock thickness (cm)	0.55 ± 0.21	0.54 ± 0.17
$\lambda^s_{i,H}$ (cm)	1.2×10^{-3} - 1.9×10^{-3}	1.8×10^{-3} - 0.020
$\lambda^s_{i,C}$ (cm)	0.085 - 0.14	0.14 - 1.6
$\lambda^s_{i,Ar}$ (cm)	0.50 - 0.82	0.81 - 9.6

As discussed in Chapter 1, the only other work this author is aware of involving the study of shock-wave induced ion species diffusion in laboratory plasma-jet collisions where the plasma-jet parameters are similar to those created using the experimental apparatus and setup discussed in this work, is the research by Byvank *et al.* [22] at the Plasma Liner Experiment's facility. In that experiment, the oblique merging or two supersonic plasma-jets composed of helium and argon results in a shock-wave that results in a shock-front separation of 0.68 cm. Based on the ion penetration lengths estimated in Table 4.9, this experimentally-observed separation is similar in scale to the separation that could be induced in the jet collisions presented in this work. Given the similarity in the plasma jet parameters before the collision occurs, with notable differences being lower jet density and slower relative velocity for Byvank *et al.*'s jets, the successful observation and diagnosis of separation in experiment in those oblique jet merging experiments validates the conclusion that separation could be measured using the railgun-polycarbonate experiment presented here.

Chapter 5

Conclusion and Future Work

This body of work has discussed the completion of three milestones towards the future study of shock-wave induced ion species separation in plasma-jet collisions. First, a plasma-jet accelerator in the form of a small, linear, plasma-armature railgun was designed and built and a pulse-forming network (PFN) of capacitors was also designed and constructed to power the railgun. Auxiliary systems, including gas delivery to the accelerator, experimental control and timing systems, data acquisition systems, and safety systems were all implemented as well. The accelerator was designed to accelerate jets of plasma to high-Mach-number with plasma parameters conducive to the formation of centimeter-scale structures in plasma-jet collisions. A full suite of diagnostics developed to characterize the resulting plasma-jets was also developed, including a Mach-Zehnder, heterodyne with quadrature interferometer, a high-resolution imaging spectrometer, and fast-photography system.

The second milestone was to characterize the plasma-jets accelerated from the railgun as the expanded in and traveled through vacuum. When measured between 10 and 40 cm away from the muzzle of the gun, jet velocity between approximately 15 and 20 km/s, electron number densities between 3×10^{14} and $3 \times 10^{16}\,\mathrm{cm}^{-3}$, and a plasma temperature around 2 eV were all diagnosed. Given these parameters, jets were accelerated to a Mach number between 5 and 7. Jet composition was also estimated, and jets were found to contain approximately 50% argon and 50% impurities based on pressure rise tests conducted in the chamber. This impurities included mainly hydrogen, carbon, aluminum, and copper based on spectral data.

Based on collision parameters estimated given this parameter range, the formation of several-millimeter to few-centimeter range structures in jet collisions should be possible. In addition to the characterization of this first jet accelerated from the railgun, a discovery was made that multiple jets were accelerated from railgun each time the pulse-forming network of capacitors was discharged due to the under-damped current pulse supplied by the PFN.

The final milestone was to induce plasma-jet collisions and measure the structures that formed when two jets collided to assess (1) whether a shock-wave was produced and (2) whether the plasma-jet parameters and collision structures were conducive to the study of ion-species separation on centimeter scales. Using the single plasma-jet accelerator designed and experimented with up to this point, plasma-jet collisions were induced between a high-Mach-number jet and background plasma by taking advantage of under-damped response of the PFN. A plate of polycarbonate was mounted inside the vacuum chamber such that the first jet accelerated from the gun would impact the polycarbonate and stagnate, producing a background plasma that the second jet to leave the gun's muzzle would impact. In these obstructed jet experiments, multi-chord interferometery and spatially and temporally-resolved spectroscopy was used to characterize the background plasma, pre-collision second jet, and post-collision plasma. Fast-images of the shot progression showed a structure form when the two jets collided. There is reasonable evidence to support the hypothesis that this structure is a shock-wave when the polycarbonate was placed 12 cm away from the gun's bore, and ultimately inconclusive evidence for the case where the polycarbonate was placed 17 cm away. Estimation of collision parameters and comparison to experimentally-observed shock structure thickness suggest that species separation of the order of ~ 5 mm could be induced during the collision.

Overall, the completion of these three milestones and this body of work provides a foundation for the future study of shock-wave induced ion-species separation. Attempts to measure

species separation using this apparatus will be among the first such experiments to study ion-diffusion mechanisms experimentally. This research effort is necessary for validating theoretical studies and computational models developed over the past decade or so to help explain anomalies between simulation and experimental results in inertial confinement fusion experiments as well to help understand the processes involved in astrophysical events such as Type-II supernovae. As this experimental effort moves forward, close attention must be paid to the other experimental work currently being pursued on this topic. Most notably, the experiments being conducted at the Plasma Liner Experiment's facility by Byvank *et al.* [22] and laboratory experiments where collisions between magnetized plasma-jets and clouds of gas are induced by Seo and Bellan [41] should be followed closely as the plasma parameters and spatial and temporal scales are similar to those of the plasma-jets and collisions discussed in this work. Experiments conducted using laboratory plasmas with those similar scale lengths can provide insight into the phenomena and mechanisms relevant to the study of shock-induced species separation that this work precedes.

5.1 Suggestions for Interferometer Improvement

In its present state, the railgun experiment utilizes many powerful diagnostics to characterize plasma parameters within the accelerated jets and the collisions and shocks that form when jets collide. Specifically, the two-chord interferometer, high-resolution spectrometer, and iCCD camera provide the tools to characterize the phenomena seen very well. Over the course of working with the experiment, however, a few suggestions have come to mind that could be implemented relatively easily to improve diagnostic ease of use or enhance the diagnostic's resolution.

The two-chord interferometer has been instrumental in allowing for an increased understand-

ing of what is happening during the jet collisions, and having two chord measurements for each shot takes a lot of ambiguity out of the data and method of analysis (see for example the velocity measurement analysis done in Section 3.3.4 when only a single-chord interferometer was utilized). Upgrading to a four chord diagnostic would provide the same level of improvement again. During the collision experiments obtaining three of four chord positions was done by running the experiment one day with two of the positions, then changing the chord positions and running again the next day. While this method was adequate, a level of uncertainty in the data was added due to human error in positioning the beams and in comparing one set of shots to another independent set. Adding two chords to the interferometer would remove some of these uncertainties.

To accomplish this upgrade, this author would recommend one of two paths. The first would be to essentially duplicate the present setup, add a second 2 mW laser to create the two additional beams (further splitting the laser used now would probably reduce the resolution of all the beams below what would be desired). The second, an admittedly more expensive improvement would be to upgrade the existing laser to a higher power model and consider fiber coupling the optics at least for a portion of the beam paths to (1) provide adequate safety is using a high-powered beam and (2) to make alignment of the four chords much easier. On the data acquisition end, adding two additional beams would not necessitate a large degree of change to the method being used now. Presently, the National Instruments PXIe daq being used has eight channels, four of which are being used for the two-chord interferometer and one which is being used for the Rogowski coil. The Rogowski coil is only being used at this point to determine the shot-to-shot jitter in the spark gap switch, and this data could be just as easily collected using one of the oscilloscopes. This would leave all eight channels of the NI daq available for the interferometer.

An additional improvement which could be made to the interferometer, regardless of whether

it's a two or four-chord system, is to add optics that re-collimate the probe beams just before they enter the chamber. Presently, the beams spread out such that when they pass through the plasma they have a diameter of $\approx 5\,\mathrm{mm}$. As the project progresses and the ability to measure structures on the order of millimeters is desired, this large beam diameter hinders that ability. Adding optics to reduce that beam diameter would greatly improve the spatial resolution of the diagnostic.

5.2 Suggestions for Spectrometer Improvement

Just near the end of this author's time working on the project did the upgrade to a fiber bundle used to carry light from the experiment to the spectrometer take place. This has led to a greatly increased capability to measure spatially and temporally resolved spectra. Additional minor changes to the setup, specifically the optical lens system currently being used, could further improve this ability and increase ease of use of the device. The lens system that is being used was designed for use without any optical fiber, in which spatial resolution was obtained by collimating a 3 inch cylindrical viewing chord down to a chord with diameter equal to the spectrometer's slit height. This design, not dissimilar to the way a camera lens works, would project this spectral image onto the spectrometer entrance slit, maintaining the spatial structure and providing great spatial resolution. In practice, however, this system was difficult to align and tune, and the amount of light that was lost when this large diameter beam hit the entrance slit meant that while spatial resolution may have been great, obtaining adequate signal to noise ratio for low gate time spectral images was very difficult. The lens has been adapted to work sufficiently with a single fiber and with the fiber bundle, but re-evaluating the optical lens setup would be another relatively low-cost means of greater improving the function of that diagnostic, especially as high spatial

and temporal resolution measurement are desired.

Bibliography

[1] R. Betti and O. A. Hurricane. Inertial-confinement fusion with lasers. *Nature Physics*, 12(5):435–448, 2016.

[2] M. H. Samimi, A. Mahari, M. A. Farahnakian, and H. Mohseni. The rogowski coil principles and applications: A review. *IEEE Sensors Journal*, 15(2):651–658, 2015.

[3] A. Frenkel, M. A. Sartor, and M. S. Wlodawski. Photon-noise-limited operation of intensified ccd cameras. *Appl. Opt.*, 36(22):5288–5297, 1997.

[4] C. Bellei, P. A. Amendt, S. C. Wilks, M. G. Haines, D. T. Casey, C. K. Li, R. Petrasso, and D. R. Welch. Species separation in inertial confinement fusion fuels. *Physics of Plasmas*, 20(1):012701, 2013.

[5] M. Y. Jaffrin and R. F. Probstein. Structure of a plasma shock wave. *The Physics of Fluids*, 7(10):1658–1674, 1964.

[6] J. D. Jukes. The structure of a shock wave in a fully ionized gas. *Journal of Fluid Mechanics*, 3(3):275–285, 1957.

[7] F. Vidal, J. P. Matte, M. Casanova, and O. Larroche. Ion kinetic simulations of the formation and propagation of a planar collisional shock wave in a plasma. *Physics of Fluids B: Plasma Physics*, 5(9):3182–3190, 1993.

[8] R. F. Post. Controlled fusion research—an application of the physics of high temperature plasmas. *Rev. Mod. Phys.*, 28:338–362, Jul 1956.

[9] C. Bellei, H. Rinderknecht, A. Zylstra, M. Rosenberg, H. Sio, C. K. Li, R. Petrasso,

S. C. Wilks, and P. A. Amendt. Species separation and kinetic effects in collisional plasma shocks. *Physics of Plasmas*, 21(5):056310, 2014.

[10] C. K. Li, F. H. Séguin, J. R. Rygg, J. A. Frenje, M. Manuel, R. D. Petrasso, R. Betti, J. Delettrez, J. P. Knauer, F. Marshall, D. D. Meyerhofer, D. Shvarts, V. A. Smalyuk, C. Stoeckl, O. L. Landen, R. P. J. Town, C. A. Back, and J. D. Kilkenny. Monoenergetic-proton-radiography measurements of implosion dynamics in direct-drive inertial-confinement fusion. *Phys. Rev. Lett.*, 100:225001, Jun 2008.

[11] P. A. Amendt, J. L. Milovich, S. C. Wilks, C. K. Li, R. D. Petrasso, and F. H. Séguin. Electric field and ionization-gradient effects on inertial-confinement-fusion implosions. *Plasma Physics and Controlled Fusion*, 51(12):124048, 2009.

[12] G. Kagan and X.-Z. Tang. Electro-diffusion in a plasma with two ion species. *Physics of Plasmas*, 19(8):082709, 2012.

[13] G. Kagan and X.-Z. Tang. Thermo-diffusion in inertially confined plasmas. *Physics Letters A*, 378(21):1531–1535, 2014.

[14] J. C. Wheeler and K. Nomoto. How stars explode: A supernova is the result of either a thermonuclear explosion of a stellar core or an implosion that leads to a rebound of the core. *American Scientist*, 73(3):240–247, 1985.

[15] S. E. Woosley, W. D. Arnett, and D. D. Clayton. The Explosive Burning of Oxygen and Silicon. *The Astrophysical Journal Supplement Series*, 26:231, November 1973.

[16] S. E. Woosley and Thomas A. Weaver. The Evolution and Explosion of Massive Stars. II. Explosive Hydrodynamics and Nucleosynthesis. *The Astrophysical Journal Supplement Series*, 101:181, Nov 1995.

[17] N. Benitez, J. Maíz-Apellániz, and M. Canelles. Evidence for nearby supernova explosions. *Physical Review Letters*, 88(8):081101, 2002.

[18] S. C. Hsu, T. R. Joshi, P. Hakel, E. L. Vold, M. J. Schmitt, N. M. Hoffman, R. M Rauenzahn, G. Kagan, X. Z. Tang, R. C Mancini, Y. Kim, and H.W. Herrmann. Observation of interspecies ion separation in inertial-confinement-fusion implosions. *Europhysics Letters*, 115(6):65001, 2016.

[19] T. R. Joshi, S. C. Hsu, P. Hakel, N. M. Hoffman, H. Sio, and R. C. Mancini. Progress on observations of interspecies ion separation in inertial-confinement-fusion implosions via imaging x-ray spectroscopy. *Physics of Plasmas*, 26(6):062702, 2019.

[20] T. R. Joshi, P. Hakel, S. C. Hsu, E. L Vold, M. J. Schmitt, N. M. Hoffman, R. M Rauenzahn, G. Kagan, X. Z. Tang, R. C. Mancini, Y. Kim, and H. W. Herrmann. Observation and modeling of interspecies ion separation in inertial confinement fusion implosions via imaging x-ray spectroscopy. *Physics of Plasmas*, 24(5):056305, 2017.

[21] H. G. Rinderknecht, H. S. Park, J. S. Ross, P. A. Amendt, S. C. Wilks, J. Katz, N. M. Hoffman, G. Kagan, E. L. Vold, B. D. Keenan, A. N. Simakov, and L. Chaćon. Measurements of ion velocity separation and ionization in multi-species plasma shocks. *Physics of Plasmas*, 25(5):056312, 2018.

[22] T. Byvank, S. J. Langendorf, S. C. Hsu, and C. Thoma. Observation of shock-front separation in multi-ion-species collisional plasma shocks. *arXiv preprint arXiv:1908.00454*, 2019.

[23] J. V. Parker. Why plasma armature railguns don't work (and what can be done about it). *IEEE Transactions on Magnetics*, 25(1):418–424, 1989.

[24] J. H. Batteh. Review of armature research (railguns). *IEEE Transactions on Magnetics*, 27(1):224–227, 1991.

[25] S. C. Hsu, E. C. Merritt, A. L. Moser, T. J. Awe, S. J. E. Brockington, J. S. Davis, C. S. Adams, A. Case, J. T. Cassibry, J. P. Dunn, M. A. Gilmore, A. G. Lynn, S. J. Messer, and F. D. Witherspoon. Experimental characterization of railgun-driven supersonic plasma jets motivated by high energy density physics applications. *Physics of Plasmas*, 19(12):123514, 2012.

[26] S. C. Hsu, A. L. Moser, E. C. Merritt, C. S. Adams, J. P. Dunn, S. Brockington, A. Case, M. Gilmore, A. G. Lynn, S. J. Messer, and et al. Laboratory plasma physics experiments using merging supersonic plasma jets. *Journal of Plasma Physics*, 81(2): 345810201, 2015.

[27] F. D. Witherspoon, A. Case, S. J. Messer, R. Bomgardner, M. W. Phillips, S. Brockington, and R. Elton. A contoured gap coaxial plasma gun with injected plasma armature. *Review of Scientific Instruments*, 80(8):083506, 2009.

[28] E. C. Merritt, A. L. Moser, S. C. Hsu, J. Loverich, and M. Gilmore. Experimental characterization of the stagnation layer between two obliquely merging supersonic plasma jets. *Phys. Rev. Lett.*, 111:085003, Aug 2013.

[29] E. C. Merritt, A. L. Moser, S. C. Hsu, C. S. Adams, J. P. Dunn, A. M. Holgado, and M. A. Gilmore. Experimental evidence for collisional shock formation via two obliquely merging supersonic plasma jets. *Physics of Plasmas*, 21(5):055703, 2014.

[30] A. L. Moser and S. C. Hsu. Experimental characterization of a transition from collisionless to collisional interaction between head-on-merging supersonic plasma jets. *Physics of Plasmas*, 22(5):055707, 2015.

[31] E. C. Merritt, A. G. Lynn, M. A. Gilmore, C. Thoma, J. Loverich, and S. C. Hsu. Multi-chord fiber-coupled interferometry of supersonic plasma jets (invited). *Review of Scientific Instruments*, 83(10):10D523, 2012.

[32] Acton Research Corporation Infobase. Imaging spectrographs. Technical report, 2013.

[33] Acton Research Corporation Infobase. Grating information. Technical report, 2013.

[34] A. Kramida, Y. Ralchenko, J. Reader, and NIST ASD Team. NIST Atomic Spectra Database (ver. 5.6.1), [Online]. Available: `https://physics.nist.gov/asd` [2019, March 12]. National Institute of Standards and Technology, Gaithersburg, MD., 2018.

[35] H. R. Griem. *Principles of Plasma Spectroscopy*, volume 2. Cambridge University Press, 2005.

[36] F. Chen. *Introduction to Plasma Physics and Controlled Fusion*. Springer, 1984.

[37] J. D. Huba. *NRL PLASMA FORMULARY Supported by The Office of Naval Research*. Naval Research Laboratory, Washington, DC, 2013.

[38] S. C. Hsu, S. J. Langendorf, K. C. Yates, J. P. Dunn, S. Brockington, A. Case, E. Cruz, F. D. Witherspoon, M. A. Gilmore, J. T. Cassibry, R. Samulyak, P. Stoltz, K. Schillo, W. Shih, K. Beckwith, and Y. C. F. Thio. Experiment to form and characterize a section of a spherically imploding plasma liner. *IEEE Transactions on Plasma Science*, 46(6):1951–1961, 2018.

[39] Prism computational sciences, inc. URL `www.prism-cs.com`.

[40] R. P. Drake. *High-Energy-Density Physics*. Springer, Berlin, 2006.

[41] B. Seo and P. M. Bellan. Experimental investigation of the compression and heating of an mhd-driven jet impacting a target cloud. *Physics of Plasmas*, 25(11):112703, 2018.

Appendices

Appendix A

MATLAB Analysis Codes

The initial organization and analysis of the raw data collected during each shot is done using two main MATLAB scripts and several MATLAB functions. Each of these codes is shown and explained below. The output of running these codes is a single HDF5 (hierarchical data format) file that contains all the raw data collected during each shot, the shot parameters that were set or used for each shot, all meta data describing the setup and/or operation of each diagnostic, and data sets of analyzed and processed data. Also, PNG image files are created to show the raw and analyzed data for each diagnostic.

A.1 Organizing and saving raw shot data

The 'analysis_save_to_hdf5.m' code shown below is the first analysis code to run. This code determines which diagnostics were used for a given shot, the shot and diagnostics settings/ parameters used, and it organizes all this data along with the raw shot data into a single HDF5 file.

```
%% Save to HDF5: Linear Plasma Railgun Data Analysis
% Save raw shot data and meta data from all diagnostics to a single hdf5
% file for each shot

%% Starting commands
close all
clear variables
```

```
clc

%% User-input variables
files=1123:1124; % input shot numbers to be analyzed
meta_data='../../../Shot_Parameters.xlsx'; % directory location and file name of excel sheet
    where meta data is stored
raw_data='../Data_Analyzed/Raw'; % directory location where raw shot data is stored

%% Read raw experimental data and attributes and save them to HDF5 files
% import metadata
[~,sheet_name]=xlsfinfo(meta_data);
for k=numel(sheet_name):-1:1
  [shot_parameters_num{k},shot_parameters_txt{k}]=xlsread(meta_data,sheet_name{k});
end
clear k sheet_name
% create directory to save new hdf5 files to if one doesn't already exist
if exist('../Data_Analyzed','dir')==0
    mkdir ../ Data_Analyzed
    if exist('../Data_Analyzed/Raw','dir')==0
        mkdir ../Data_Analyzed Raw
    end
end

% Use function "read_raw_data" to import data and attribures for all shots
% and place them into structures
files_flip=flip(files);
for i=files_flip
    % if file for Shot i already exists, overwrite it
    h5_exist=exist([raw_data,num2str(i),'_raw.h5'],'file');
    if h5_exist==2
        delete([raw_data,num2str(i),'_raw.h5'])
        disp(['Existing data structure found and deleted for Shot ',num2str(i)])
    end
    clear h5_exist

    %% Save High-level Shot Parameters
    h5create([raw_data,num2str(i),'_raw.h5'],'/Shot_parameters',[1,1])
    h5write([raw_data,num2str(i),'_raw.h5'],'/Shot_parameters',i)
    h5writeatt([raw_data,num2str(i),'_raw.h5'],'/Shot_parameters','GPV_time(mu-s)',int32(-
```

```
        shot_parameters_num{2}(i,3)))
    h5writeatt([raw_data,num2str(i),'_raw.h5'],'/Shot_parameters','GPV_pressure(psi)',int32(
        shot_parameters_num{2}(i,2)))
    h5writeatt([raw_data,num2str(i),'_raw.h5'],'/Shot_parameters','GPV_voltage(V)',int32(
        shot_parameters_num{2}(i,4)))
    h5writeatt([raw_data,num2str(i),'_raw.h5'],'/Shot_parameters','PFN_voltage(kV)',int32(
        shot_parameters_num{2}(i,5)))
    for j=length(shot_parameters_num{1}):-1:1
        if i>=shot_parameters_num{1}(j,1) && i<=shot_parameters_num{1}(j,2)
            h5writeatt([raw_data,num2str(i),'_raw.h5'],'/Shot_parameters','experiment_date',
                datestr(shot_parameters_txt{1}(j+1,1)))
            break
        end
    end
    %use the read_raw_data.m function to import and organize data
    [time_pxie,Ch0,Ch1,Ch2,Ch3,Ch4,Ch5,Ch6,~,time_scope,scope1,scope2,scope3,scope4,spec,
        pxie_sample_rate,~,time_data_acq,pxie_sample_spark_gap_start,scope_sample_spark_gap_start
        ,~,time_pxie_max,~,~,scope_sample_rate,~,time_scope_max,pxie_file_exist,scope_file_exist,
        spec_file_exist]=read_raw_data(i);
    clear j

    %% Save Time Data
    % determine whether the pxie and scope were used to save data and save
    % meta data and time data for the daqs that were used
    if isempty(time_pxie)==0
        h5create([raw_data,num2str(i),'_raw.h5'],'/Time/PXIe(mu-s)',length(time_pxie))
        h5write([raw_data,num2str(i),'_raw.h5'],'/Time/PXIe(mu-s)',time_pxie)
        h5writeatt([raw_data,num2str(i),'_raw.h5'],'/Time/PXIe(mu-s)','sample_rate(Hz)',int32(
            pxie_sample_rate))
        h5writeatt([raw_data,num2str(i),'_raw.h5'],'/Time/PXIe(mu-s)','sample_sg_start',int32(
            pxie_sample_spark_gap_start))
        h5writeatt([raw_data,num2str(i),'_raw.h5'],'/Time/PXIe(mu-s)','time_data_acq_start(mu-s)'
            ,int32(time_data_acq))
        h5writeatt([raw_data,num2str(i),'_raw.h5'],'/Time/PXIe(mu-s)','time_data_acq_end(mu-s)',
            int32(time_pxie_max))
    end
    if isempty(time_scope)==0
        h5create([raw_data,num2str(i),'_raw.h5'],'/Time/Scope(mu-s)',length(time_scope))
        h5write([raw_data,num2str(i),'_raw.h5'],'/Time/Scope(mu-s)',time_scope)
```

```
        h5writeatt([raw_data,num2str(i),'_raw.h5'],'/Time/Scope(mu-s)','sample_rate(Hz)',int32(scope_sample_rate))
        h5writeatt([raw_data,num2str(i),'_raw.h5'],'/Time/Scope(mu-s)','sample_sg_start',int32(scope_sample_spark_gap_start))
        h5writeatt([raw_data,num2str(i),'_raw.h5'],'/Time/Scope(mu-s)','time_data_acq_start(mu-s)',int32(time_data_acq))
        h5writeatt([raw_data,num2str(i),'_raw.h5'],'/Time/Scope(mu-s)','time_data_acq_end(mu-s)',int32(time_scope_max))
    end
    clear time_pxie time_data_acq time_gas_puff time_pxie_max time_pxie_step time_scope time_scope_max time_scope_step pxie_sample_number pxie_sample_rate pxie_sample_spark_gap_start scope_sample_number scope_sample_rate scope_sample_spark_gap_start

    %% Save Rogowski Coil Data
    % determine how many coils were used and save raw data and metadata for
    % all coils that were used
    Rog_number=shot_parameters_num{6}(i,3); % Number of Rogowski Coils used
    if strcmpi(shot_parameters_txt{6}(i+1,2),'pxie')==1 % PXIe was used as daq
        if pxie_file_exist==2 % make sure raw data file exists for this shot
            Rog_and_noise=[Ch0,Ch5]; % currently, 2 coils may be used with the PXIe, the first in channel 0 and the other in channel 5
            % Add Rogowski Coil data to HDF5 file
            for j=1:Rog_number
                h5create([raw_data,num2str(i),'_raw.h5'],['/Rogowski_Coil/Coil',num2str(j),'/Signal_raw(V)'],length(Rog_and_noise(:,1)))
                h5write([raw_data,num2str(i),'_raw.h5'],['/Rogowski_Coil/Coil',num2str(j),'/Signal_raw(V)'],Rog_and_noise(:,j).*shot_parameters_num{6}(i,j*3+3)) % save the raw signal accounting for coil turn direction
                h5writeatt([raw_data,num2str(i),'_raw.h5'],['/Rogowski_Coil/Coil',num2str(j)],'calibration_factor(kA/V)',shot_parameters_num{6}(i,j*3+2)) % save the coil calibration factor
                h5writeatt([raw_data,num2str(i),'_raw.h5'],['/Rogowski_Coil/Coil',num2str(j)],'daq_source','pxie') % save the daq source that was used
                h5writeatt([raw_data,num2str(i),'_raw.h5'],['/Rogowski_Coil/Coil',num2str(j)],'coil_name',char(shot_parameters_txt{6}(i+1,j*3+1))) % save the name of the coil used
            end
        else
```

```
            disp(['No rogowski coil data saved for Shot ',num2str(i)])
        end
    elseif strcmpi(shot_parameters_txt{6}(i+1,2),'scope')==1 % Scope was used as daq, all other comments above apply here
        if scope_file_exist==2
            Rog_and_noise=[scope3,scope4];
            for j=1:Rog_number
                h5create([raw_data,num2str(i),'_raw.h5'],['/Rogowski_Coil/Coil',num2str(j),'/Signal_raw(V)'],length(Rog_and_noise(:,1)))
                h5write([raw_data,num2str(i),'_raw.h5'],['/Rogowski_Coil/Coil',num2str(j),'/Signal_raw(V)'],Rog_and_noise(:,j).*shot_parameters_num{6}(i,j*3+3))
                h5writeatt([raw_data,num2str(i),'_raw.h5'],['/Rogowski_Coil/Coil',num2str(j)],'calibration_factor(kA/V)',shot_parameters_num{6}(i,j*3+2))
                h5writeatt([raw_data,num2str(i),'_raw.h5'],['/Rogowski_Coil/Coil',num2str(j)],'daq_source','scope')
                h5writeatt([raw_data,num2str(i),'_raw.h5'],['/Rogowski_Coil/Coil',num2str(j)],'coil_name',char(shot_parameters_txt{6}(i+1,j*3+1)))
            end
        else
            disp(['No rogowski coil data saved for Shot ',num2str(i)])
        end
    else
        disp(['No rogowski coil data saved for Shot ',num2str(i)])
    end
    clear Ch0 scope3 scope4 Rog_and_noise Rog_number j scope_file_exist

    %% Save Photodiode Data
    % check to see if photodiode data was saved for shot i and save the raw
    % and meta data for shot i
    if isnan(shot_parameters_num{5}(i,2))==0 && pxie_file_exist % check to see if photodiode meta data exists for this shot and alert user if it doesn't
        h5create([raw_data,num2str(i),'_raw.h5'],'/Photodiodes/PD1_raw(V)',length(Ch1))
        h5write([raw_data,num2str(i),'_raw.h5'],'/Photodiodes/PD1_raw(V)',Ch1)
        h5create([raw_data,num2str(i),'_raw.h5'],'/Photodiodes/PD2_raw(V)',length(Ch2))
        h5write([raw_data,num2str(i),'_raw.h5'],'/Photodiodes/PD2_raw(V)',Ch2)
        h5writeatt([raw_data,num2str(i),'_raw.h5'],'/Photodiodes','daq_source','pxie')
        h5writeatt([raw_data,num2str(i),'_raw.h5'],'/Photodiodes','PD2_PD1_separation_distance(cm)',shot_parameters_num{5}(i,2)*2.54)
        if isnan(shot_parameters_num{5}(i,3))==0
```

```
            h5writeatt([raw_data,num2str(i),'_raw.h5'],'/Photodiodes','PD1_muzzle_separation_distance(cm)',shot_parameters_num{5}(i,3)*2.54)
        end
    else
        disp(['No photodiode data saved for Shot ',num2str(i)])
    end
    clear Ch1 Ch2 pxie_file_exist

    %% Save Spectrometer Data
    % determine if the thorlabs and/or spectra pro spectrometers were used
    % for shot i and save raw data and meta data for both spectrometer for
    % shot i
    if spec_file_exist==2 % save spectrometer data to the HDF5 file or alert user if no spectroemter data is found
        for j=1:length(spec)
            h5create([raw_data,num2str(i),'_raw.h5'],['/Spectrometer_',spec(j).source,'/Wavelength(nm)'],size(spec(j).wavelength))
            h5write([raw_data,num2str(i),'_raw.h5'],['/Spectrometer_',spec(j).source,'/Wavelength(nm)'],spec(j).wavelength)
            h5create([raw_data,num2str(i),'_raw.h5'],['/Spectrometer_',spec(j).source,'/Intensity(AU)'],size(spec(j).intensity))
            h5write([raw_data,num2str(i),'_raw.h5'],['/Spectrometer_',spec(j).source,'/Intensity(AU)'],spec(j).intensity)
            if strcmpi(spec(j).source,'SpectraPro')==1 % if SpectraPro spectrometer was used, also save the spectrometer attributes and row data (row of CCD pixel array each pixel belongs to)
                h5create([raw_data,num2str(i),'_raw.h5'],['/Spectrometer_',spec(j).source,'/Row'],size(spec(j).row))
                h5write([raw_data,num2str(i),'_raw.h5'],['/Spectrometer_',spec(j).source,'/Row'],spec(j).row)
                h5writeatt([raw_data,num2str(i),'_raw.h5'],['/Spectrometer_',spec(j).source],'PIMAX_intensifier_gain(0-100)',int32(shot_parameters_num{7}(i,3)))
                h5writeatt([raw_data,num2str(i),'_raw.h5'],['/Spectrometer_',spec(j).source],'grating(g/mm)',int32(shot_parameters_num{7}(i,2)))
                h5writeatt([raw_data,num2str(i),'_raw.h5'],['/Spectrometer_',spec(j).source],'t_gate_width(mu-s)',shot_parameters_num{7}(i,4))
                h5writeatt([raw_data,num2str(i),'_raw.h5'],['/Spectrometer_',spec(j).source],'slit_width(mu-m)',shot_parameters_num{7}(i,5))
                h5writeatt([raw_data,num2str(i),'_raw.h5'],['/Spectrometer_',spec(j).source],'
```

```
                    center_wavelength(nm)',shot_parameters_num{7}(i,6))
                h5writeatt([raw_data,num2str(i),'_raw.h5'],['/Spectrometer_',spec(j).source],'
                    t_gate_delay(mu-s)',shot_parameters_num{7}(i,7))
                h5writeatt([raw_data,num2str(i),'_raw.h5'],['/Spectrometer_',spec(j).source],'
                    viewing_chord_location(cm)',shot_parameters_num{7}(i,8)*2.54)
            elseif strcmpi(spec(j).source,'Thorlabs')==1 % if Thorlabs spectrometer wa used, also
                 save associated attributes
                h5writeatt([raw_data,num2str(i),'_raw.h5'],['/Spectrometer_',spec(j).source],'
                    t_gate_width(mu-s)',shot_parameters_num{8}(i,2))
                h5writeatt([raw_data,num2str(i),'_raw.h5'],['/Spectrometer_',spec(j).source],'
                    viewing_chord_location(cm)',shot_parameters_num{8}(i,3)*2.54)
            end
        end
    else
        disp(['No spectrometer data saved for Shot ',num2str(i)])
    end
    clear j spec_file_exist

    %% Save Interferometer Data
    % determine if interferometer data was saved and if so, which daq was
    % used for shot i and save the raw data and meta data for that shot
    if strcmpi(shot_parameters_txt{4}(i,3),'scope')==1 % scope was used as daq
        if isempty(scope1)==0
            h5create([raw_data,num2str(i),'_raw.h5'],'/Interferometer/I_raw(V)',length(scope1))
            h5write([raw_data,num2str(i),'_raw.h5'],'/Interferometer/I_raw(V)',scope1)
            h5create([raw_data,num2str(i),'_raw.h5'],'/Interferometer/Q_raw(V)',length(scope2))
            h5write([raw_data,num2str(i),'_raw.h5'],'/Interferometer/Q_raw(V)',scope2)
            h5writeatt([raw_data,num2str(i),'_raw.h5'],'/Interferometer','daq_source','scope')
            h5writeatt([raw_data,num2str(i),'_raw.h5'],'/Interferometer','
                chord_bore_axis_intersection_distance(cm)',shot_parameters_num{4}(i,2)*2.54)
        else
            disp(['No interferometer data saved for Shot ',num2str(i)])
        end
    elseif strcmpi(shot_parameters_txt{4}(i,3),'pxie')==1 % pxie was used as daq
        if shot_parameters_num{4}(i,4)==1
            if isempty(Ch3)==0
                h5create([raw_data,num2str(i),'_raw.h5'],'/Interferometer/I_raw(V)',length(Ch3))
                h5write([raw_data,num2str(i),'_raw.h5'],'/Interferometer/I_raw(V)',Ch3)
                h5create([raw_data,num2str(i),'_raw.h5'],'/Interferometer/Q_raw(V)',length(Ch4))
```

```
                h5write([raw_data,num2str(i),'_raw.h5'],'/Interferometer/Q_raw(V)',Ch4)
                h5writeatt([raw_data,num2str(i),'_raw.h5'],'/Interferometer','daq_source','pxie')
                h5writeatt([raw_data,num2str(i),'_raw.h5'],'/Interferometer','chord_bore_axis_intersection_distance(cm)',shot_parameters_num{4}(i,2)*2.54)
                h5create([raw_data,num2str(i),'_raw.h5'],'/Interferometer/I2_raw(V)',length(Ch5))
                h5write([raw_data,num2str(i),'_raw.h5'],'/Interferometer/I2_raw(V)',Ch5)
                h5create([raw_data,num2str(i),'_raw.h5'],'/Interferometer/Q2_raw(V)',length(Ch6))
                h5write([raw_data,num2str(i),'_raw.h5'],'/Interferometer/Q2_raw(V)',Ch6)
                h5writeatt([raw_data,num2str(i),'_raw.h5'],'/Interferometer','2nd_chord_bore_axis_intersection_distance(cm)',shot_parameters_num{4}(i,5)*2.54)
                h5writeatt([raw_data,num2str(i),'_raw.h5'],'/Interferometer','number_of_chords',int32(2))
            else
                disp(['No interferometer data saved for Shot ',num2str(i)])
            end
        elseif shot_parameters_num{4}(i,4)==0
            if isempty(Ch3)==0
                h5create([raw_data,num2str(i),'_raw.h5'],'/Interferometer/I_raw(V)',length(Ch3))
                h5write([raw_data,num2str(i),'_raw.h5'],'/Interferometer/I_raw(V)',Ch3)
                h5create([raw_data,num2str(i),'_raw.h5'],'/Interferometer/Q_raw(V)',length(Ch4))
                h5write([raw_data,num2str(i),'_raw.h5'],'/Interferometer/Q_raw(V)',Ch4)
                h5writeatt([raw_data,num2str(i),'_raw.h5'],'/Interferometer','daq_source','pxie')
                h5writeatt([raw_data,num2str(i),'_raw.h5'],'/Interferometer','chord_bore_axis_intersection_distance(cm)',shot_parameters_num{4}(i,2)*2.54)
                h5writeatt([raw_data,num2str(i),'_raw.h5'],'/Interferometer','number_of_chords',int32(1))
            else
                disp(['No interferometer data saved for Shot ',num2str(i)])
            end
        end
    else
        disp(['No interferometer data saved for Shot ',num2str(i)])
    end
    clear scope1 scope2 Ch3 Ch4 Ch5 Ch6

    %% Save PIMAX Data
    % determine if the pimax camera was used for shot i and if it was used
    % to image the plasma directly or as the imager for the spectrometer,
```

```
    % save the raw data in either case
    pimax_file_exist=exist(['../Data/pimax',num2str(i),'.tif'],'file');
    pimax_spec_exist=exist(['../Data/pimax',num2str(i),'.csv'],'file');
    if pimax_file_exist==2 && pimax_spec_exist==0
        pimax=imread(['../Data/pimax',num2str(i),'.tif']);
        h5create([raw_data,num2str(i),'_raw.h5'],'/PIMAX/Plasma_image',size(pimax),'Datatype','
            uint16')
        h5write([raw_data,num2str(i),'_raw.h5'],'/PIMAX/Plasma_image',pimax)
        h5writeatt([raw_data,num2str(i),'_raw.h5'],'/PIMAX/Plasma_image','gate_delay(mus)',
            shot_parameters_num{3}(i,4))
        h5writeatt([raw_data,num2str(i),'_raw.h5'],'/PIMAX/Plasma_image','mount_angle(deg)',
            shot_parameters_num{3}(i,2))
        h5writeatt([raw_data,num2str(i),'_raw.h5'],'/PIMAX/Plasma_image','mount_distance(in)',
            shot_parameters_num{3}(i,3))
        h5writeatt([raw_data,num2str(i),'_raw.h5'],'/PIMAX/Plasma_image','t_gate_open(\mus)',
            shot_parameters_num{3}(i,4))
        h5writeatt([raw_data,num2str(i),'_raw.h5'],'/PIMAX/Plasma_image','t_gate_width(\mus)',
            shot_parameters_num{3}(i,6))
        h5writeatt([raw_data,num2str(i),'_raw.h5'],'/PIMAX/Plasma_image','intensifier_gain(1-100)
            ',shot_parameters_num{3}(i,5))
        h5writeatt([raw_data,num2str(i),'_raw.h5'],'/PIMAX/Plasma_image','lens_aperture(f/)',
            shot_parameters_num{3}(i,7))
    elseif pimax_file_exist==2 && pimax_spec_exist==2
        pimax=imread(['../Data/pimax',num2str(i),'.tif']);
        h5create([raw_data,num2str(i),'_raw.h5'],'/Spectrometer_SpectraPro/PIMAX_image',size(
            pimax),'Datatype','uint16')
        h5write([raw_data,num2str(i),'_raw.h5'],'/Spectrometer_SpectraPro/PIMAX_image',pimax)
    else
        disp(['No PIMAX image saved for Shot ',num2str(i)])
    end
    clear pimax_file_exist pimax_spec_exist pimax spec
end
clear files i shot_parameters_num shot_parameters_txt
```

A.2 Basic analysis and plotting

The 'analysis_processing_and_plotting_hdf5.m' code shown below takes the hdf5 file that was the output of the 'analysis_save_to_hdf5.m' code and conducts preliminary analysis for each diagnostic. For example, this includes calculating phase shift and line-integrated density from the raw interferometer I and Q signals, integrating and detrending Rogowski coil signal, and binning and summing spectral intensity data. This analyzed data is saved to a new HDF5 file along with all the raw and meta data contained in the original file. Finally, the code also creates PNG images to show the raw and analyzed data for each diagnostic, providing a quick, easy way to visualize shot data.

```
%% Processing and Plotting: Linear Plasma Railgun Data Analysis
% Import saved hdf5 raw shot data and attributes for each shot and and
% analyze date, create plots, and update saved hdf5 file

%% Starting Commands
close all
clear variables
clc
set(0,'DefaultAxesXGrid','on','DefaultAxesYGrid','on') %turn grid on for all plots
set(0,'DefaultAxesFontSize',16) %change the default figure axes font size

%% User-input Variables
files=1123:1124; % input shot numbers to analyze
spec_rows_to_bin=[460,580]; %rows in the pimax image to bin when summing intensity of SpectraPro
    spectrometer (input [1,1024] if you want to sum all rows)
raw_hdf5_folder='../Data_Analyzed/Raw/'; %directory location where the hdf5 file with raw and
    meta data is kept
analyzed_hdf5_folder='../../../Analyzed_hdf5_data_files/'; % directory location where you want
    new hdf5 files with analyzed data to be saved

%% Setup
% initialize data_exist structure to ensure all fields exist as empty
% matrices for each shot; this is necessary for using matlab's isempty
% function to determine for each individual diagnostic section below
```

```
% whether or not to attempt analysis for that each shot
data_exist(files(end)).rogowski_coil=[];
data_exist(files(end)).photodiodes=[];
data_exist(files(end)).spectrometer_sp=[];
data_exist(files(end)).spectrometer_th=[];
data_exist(files(end)).interferometer=[];
data_exist(files(end)).pimax=[];
% for each shot, fill in the data_exist structure and create analyzed.h5
% file to populate with analyzed data in the following sections.
files_flip=flip(files);
for i=files_flip
    % if analyzed data hdf5 file already exists for Shot i, overwrite it
    h5_analyze_exist=exist([analyzed_hdf5_folder,num2str(i),'_analyzed.h5'],'file');
    if h5_analyze_exist==2
        delete([analyzed_hdf5_folder,num2str(i),'_analyzed.h5'])
        disp(['Existing data structure found and deleted for Shot ',num2str(i)])
    end
    clear h5_analyze_exist
    % copy raw data hdf5 file to shot#_analyzed.h5 file
    copyfile([raw_hdf5_folder,num2str(i),'_raw.h5'],[analyzed_hdf5_folder,num2str(i),'_analyzed.
        h5'])
    % Determine which diagnostics were used for shot i and add that
    % information to a structure so that analysis sections below can be
    % skipped for diagnostics where no data was recorded
    info=h5info([analyzed_hdf5_folder,num2str(i),'_analyzed.h5']);
    for j=1:length(info.Groups)
        if strcmpi(info.Groups(j).Name,'/Rogowski_Coil')==1
            data_exist(i).rogowski_coil=1;
            Rog_number(i)=length(info.Groups(j).Groups);
        elseif strcmpi(info.Groups(j).Name,'/Photodiodes')==1
            data_exist(i).photodiodes=1;
        elseif strcmpi(info.Groups(j).Name,'/Spectrometer_SpectraPro')==1
            data_exist(i).spectrometer_sp=1;
        elseif strcmpi(info.Groups(j).Name,'/Spectrometer_Thorlabs')==1
            data_exist(i).spectrometer_th=1;
        elseif strcmpi(info.Groups(j).Name,'/Interferometer')==1
            data_exist(i).interferometer=1;
        elseif strcmpi(info.Groups(j).Name,'/PIMAX')==1
            data_exist(i).pimax=1;
```

```
        end
    end
end

%% Rogowski Coil Analysis
for i=files_flip
    if data_exist(i).rogowski_coil==1
        legend_info=string(zeros(1,Rog_number(i)));
        A=figure('Name',['Shot ',num2str(i),' Rogowski Coil Current']);
        %set(A,'Visible','off');
        % for the number of coils used in each shot, determine whehter the
        % pxie or scope was used as a daq and raw and meta data
        for j=1:Rog_number(i)
            if strcmpi(h5readatt([analyzed_hdf5_folder,num2str(i),'_analyzed.h5'],['/Rogowski_Coil/Coil',num2str(j)],'daq_source'),'pxie')==1
                time_Rog=h5read([analyzed_hdf5_folder,num2str(i),'_analyzed.h5'],'/Time/PXIe(mu-s)');
                sample_start=h5readatt([analyzed_hdf5_folder,num2str(i),'_analyzed.h5'],'/Time/PXIe(mu-s)','sample_sg_start');
                sample_end=length(time_Rog);
                sample_rate=h5readatt([analyzed_hdf5_folder,num2str(i),'_analyzed.h5'],'/Time/PXIe(mu-s)','sample_rate(Hz)');
            elseif strcmpi(h5readatt([analyzed_hdf5_folder,num2str(i),'_analyzed.h5'],['/Rogowski_Coil/Coil',num2str(j)],'daq_source'),'scope')==1
                time_Rog=h5read([analyzed_hdf5_folder,num2str(i),'_analyzed.h5'],'/Time/Scope(mu-s)');
                sample_start=h5readatt([analyzed_hdf5_folder,num2str(i),'_analyzed.h5'],'/Time/Scope(mu-s)','sample_sg_start');
                sample_end=length(time_Rog);
                sample_rate=h5readatt([analyzed_hdf5_folder,num2str(i),'_analyzed.h5'],'/Time/Scope(mu-s)','sample_rate(Hz)');
            end
            signal_raw=h5read([analyzed_hdf5_folder,num2str(i),'_analyzed.h5'],['/Rogowski_Coil/Coil',num2str(j),'/Signal_raw(V)']);
            %use the rogowski_analysis.m function to integrate and
            %calibrate the raw data to obtain a current trace
            [current_raw,current_calibrated,trend_line,sg_delay_time]=rogowski_analysis(signal_raw,h5readatt([analyzed_hdf5_folder,num2str(i),'_analyzed.h5'],['/Rogowski_Coil/Coil',num2str(j)],'calibration_factor(kA/V)'),time_Rog,sample_rate,
```

```
            sample_start,sample_end,i);
        h5create([analyzed_hdf5_folder,num2str(i),'_analyzed.h5'],['/Rogowski_Coil/Coil',
            num2str(j),'/Current(kA)'],length(signal_raw))
        h5write([analyzed_hdf5_folder,num2str(i),'_analyzed.h5'],['/Rogowski_Coil/Coil',
            num2str(j),'/Current(kA)'],current_calibrated.*1E-3)
        h5writeatt([analyzed_hdf5_folder,num2str(i),'_analyzed.h5'],['/Rogowski_Coil/Coil',
            num2str(j)],'current_peak(kA)',max(current_calibrated))
        h5writeatt([analyzed_hdf5_folder,num2str(i),'_analyzed.h5'],['/Rogowski_Coil/Coil',
            num2str(j)],'t_spark_gap_delay(mu-s)',sg_delay_time)
        legend_info{j}=['Coil ',h5readatt([analyzed_hdf5_folder,num2str(i),'_analyzed.h5'],['
            /Rogowski_Coil/Coil',num2str(j)],'coil_name')];
        %create and save a plot of the raw rowoski coil signal,
        %analysis process, and final current calculated
        subplot(2,2,1)
        plot(time_Rog,signal_raw)
        hold on
        if j==Rog_number(i)
            xlim([-200 800])
            ylabel('Signal (V)')
            xlabel('Time (\mus)')
            legend({legend_info},'FontSize',10)
        end
        subplot(2,2,2)
        plot(time_Rog,current_raw)
        hold on
        plot(time_Rog,trend_line,'--k')
        hold on
        if j==Rog_number(i)
            xlim([-50 250])
            ylabel('Integrated Signal (A.U.)')
            xlabel('Time (\mus)')
            legend({legend_info},'FontSize',10)
        end
        subplot(2,2,[3 4])
        plot(time_Rog,current_calibrated)
        hold on
    end
    xlabel('Time (\mus)')
    ylabel('Current (kA)')
```

```
121         xlim([-50 250])
122         legend({legend_info},'FontSize',14)
123         fig=gcf;
124         fig.PaperUnits='inches';
125         fig.PaperPosition=[0 0 8 6];
126         print(['../../../Figures_and_images/PNG/Rogowski_Coil/Shot',num2str(i),'_Rogowski_Current
                '],'-dpng','-r200')
127         close
128     end
129 end
130 clear legend_info Rog_number A fig j sample_rate sample_end sample_start trend_line i time_Rog
        signal_raw current_raw current_calibrated trend line sg_delay_time
131
132 %% Photodiode Analysis
133 for i=files_flip
134     if data_exist(i).photodiodes==1
135         % read raw photodiode data and associated time data
136         PD1=h5read([analyzed_hdf5_folder,num2str(i),'_analyzed.h5'],'/Photodiodes/PD1_raw(V)');
137         PD2=h5read([analyzed_hdf5_folder,num2str(i),'_analyzed.h5'],'/Photodiodes/PD2_raw(V)');
138         time=h5read([analyzed_hdf5_folder,num2str(i),'_analyzed.h5'],'/Time/PXIe(mu-s)');
139         if data_exist(i).rogowski_coil==1
140             % if rogowski coil data exists for shot i import that data as
141             % well to be included in the photodiode figure created
142             Rog=h5read([analyzed_hdf5_folder,num2str(i),'_analyzed.h5'],'/Rogowski_Coil/Coil1/
                    Current(kA)');
143             if strcmpi(h5readatt([analyzed_hdf5_folder,num2str(i),'_analyzed.h5'],'/Rogowski_Coil
                    /Coil1','daq_source'),'pxie')==1
144                 time_Rog=h5read([analyzed_hdf5_folder,num2str(i),'_analyzed.h5'],'/Time/PXIe(mu-s
                        )');
145             elseif strcmpi(h5readatt([analyzed_hdf5_folder,num2str(i),'_analyzed.h5'],'/
                    Rogowski_Coil/Coil1','daq_source'),'scope')==1
146                 time_Rog=h5read([analyzed_hdf5_folder,num2str(i),'_analyzed.h5'],'/Time/Scope(mu-
                        s)');
147             end
148         end
149         %create and save a figure of normalized photodiode signal and
150         %rogowski coil signal
151         A=figure('Name',['Shot ',num2str(i),' Photodiode Signal']);
152         %set(A,'Visible','off');
```

```
        plot(time,PD1./max(PD1))
        hold on
        plot(time,PD2./max(PD2))
        hold on
        if data_exist(i).rogowski_coil==1
            plot(time_Rog,Rog./max(Rog))
        end
        grid minor
        xlim([-10 200])
        ylim([-0.5 1.1])
        xlabel('Time (\mus)')
        ylabel('Normalized Signal (V/V_{max})')
        legend({'PD 1','PD 2','Normalized current'},'FontSize',16)
        fig=gcf;
        fig.PaperUnits='inches';
        fig.PaperPosition=[0 0 8 6];
        print(['../../../Figures_and_images/PNG/Photodiodes/Shot',num2str(i),'_Photodiode_Signal'
            ],'-dpng','-r200')
        close
    end
end
clear A time_Rog PD1 PD2 time time_Rog fig Rog

%% Spectrometer Analysis
for i=files_flip
    % Thorlabs Spectrometer
    if data_exist(i).spectrometer_th==1
        % plot and save a figure of the raw wavelength vs intensity trace
        A=figure('Name',['Shot ',num2str(i),' Thorlabs Spectrometer Signal']);
        %set(A,'Visible','off');
        th_wavelength=h5read([analyzed_hdf5_folder,num2str(i),'_analyzed.h5'],'/
            Spectrometer_Thorlabs/Wavelength(nm)');
        th_intensity=h5read([analyzed_hdf5_folder,num2str(i),'_analyzed.h5'],'/
            Spectrometer_Thorlabs/Intensity(AU)');
        plot(th_wavelength,th_intensity)
        xlabel('Wavelength (nm)')
        ylabel('Intensity (A.U.)')
        xlim([floor(th_wavelength(1)) ceil(th_wavelength(end))])
        fig=gcf;
```

```
        fig.PaperUnits='inches';
        fig.PaperPosition=[0 0 8 6];
        print(['../../../Figures_and_images/PNG/Spectrometer/Shot',num2str(i),'_Thorlabs_Spectrometer_Signal'],'-dpng','-r200')
        close
    end
    % SpectraPro Spectrometer
    if data_exist(i).spectrometer_sp==1
        % sum the intensity over all pixels of shot i and create a figure
        % showing a plot of wavelength vs summed intensities
        A=figure('Name',['Shot ',num2str(i),' SpectraPro Spectrometer Signal']);
        %set(A,'Visible','off');
        sp_wavelength=h5read([analyzed_hdf5_folder,num2str(i),'_analyzed.h5'],'/Spectrometer_SpectraPro/Wavelength(nm)');
        sp_intensity=h5read([analyzed_hdf5_folder,num2str(i),'_analyzed.h5'],'/Spectrometer_SpectraPro/Intensity(AU)');
        h5create([analyzed_hdf5_folder,num2str(i),'_analyzed.h5'],'/Spectrometer_SpectraPro/Wavelength_plot(nm)',length(sp_wavelength))
        h5write([analyzed_hdf5_folder,num2str(i),'_analyzed.h5'],'/Spectrometer_SpectraPro/Wavelength_plot(nm)',sp_wavelength(:,1))
        h5create([analyzed_hdf5_folder,num2str(i),'_analyzed.h5'],'/Spectrometer_SpectraPro/Intensity_sum(AU)',length(sp_intensity))
        h5write([analyzed_hdf5_folder,num2str(i),'_analyzed.h5'],'/Spectrometer_SpectraPro/Intensity_sum(AU)',sum(sp_intensity(:,spec_rows_to_bin(1):spec_rows_to_bin(2)),2))
        plot(sp_wavelength(:,1),sum(sp_intensity,2))
        xlabel('Wavelength (nm)')
        ylabel('Intensity (A.U.)')
        xlim([floor(sp_wavelength(1,1)) ceil(sp_wavelength(end,1))])
        fig=gcf;
        fig.PaperUnits='inches';
        fig.PaperPosition=[0 0 8 6];
        print(['../../../Figures_and_images/PNG/Spectrometer/Shot',num2str(i),'_SpectraPro_Spectrometer_Signal'],'-dpng','-r200')
        close
    end
end
clear A fig sp_intensity sp_wavelength th_intensity th_wavelength

%% PIMAX Image Analysis
```

```
for i=files_flip
    % determine if pimax image was taken either with the spectrometer or
    % just as a stand alone image of the plasma in the chamber
    if data_exist(i).pimax==1
        % if the PIMAX camera was used to take an image of the plasma, use
        % the pimax_analysis.m function to analyze the raw image data to
        % create and save grayscale and false-colored images of the data in
        % both original and log form.
        plasma_image=h5read([analyzed_hdf5_folder,num2str(i),'_analyzed.h5'],'/PIMAX/Plasma_image');
        [grayscale_image,grayscale_image_log,color_image,color_image_log]=pimax_analysis(plasma_image,i,1);
        h5create([analyzed_hdf5_folder,num2str(i),'_analyzed.h5'],'/PIMAX/Plasma_Image/Grayscale_image',size(grayscale_image))
        h5write([analyzed_hdf5_folder,num2str(i),'_analyzed.h5'],'/PIMAX/Plasma_Image/Grayscale_image',grayscale_image)
        h5create([analyzed_hdf5_folder,num2str(i),'_analyzed.h5'],'/PIMAX/Plasma_Image/Grayscale_image_log',size(grayscale_image_log))
        h5write([analyzed_hdf5_folder,num2str(i),'_analyzed.h5'],'/PIMAX/Plasma_Image/Grayscale_image_log',grayscale_image_log)
        h5create([analyzed_hdf5_folder,num2str(i),'_analyzed.h5'],'/PIMAX/Plasma_Image/Color_image',size(color_image))
        h5write([analyzed_hdf5_folder,num2str(i),'_analyzed.h5'],'/PIMAX/Plasma_Image/Color_image',color_image)
        h5create([analyzed_hdf5_folder,num2str(i),'_analyzed.h5'],'/PIMAX/Plasma_Image/Color_image_log',size(color_image_log))
        h5write([analyzed_hdf5_folder,num2str(i),'_analyzed.h5'],'/PIMAX/Plasma_Image/Color_image_log',color_image_log)
    elseif data_exist(i).spectrometer_sp==1
        % if the PIMAX camera was used to image the spectrometer, use the
        % pimax_analysis.m function to create grayscale image files of the
        % raw spectral data
        plasma_image=h5read([analyzed_hdf5_folder,num2str(i),'_analyzed.h5'],'/Spectrometer_SpectraPro/PIMAX_image');
        [grayscale_image,grayscale_image_log,~,~]=pimax_analysis(plasma_image,i,0);
        h5create([analyzed_hdf5_folder,num2str(i),'_analyzed.h5'],'/Spectrometer_SpectraPro/PIMAX_grayscale_image',size(grayscale_image))
        h5write([analyzed_hdf5_folder,num2str(i),'_analyzed.h5'],'/Spectrometer_SpectraPro/PIMAX_grayscale_image',grayscale_image)
```

```
        h5create([analyzed_hdf5_folder,num2str(i),'_analyzed.h5'],'/Spectrometer_SpectraPro/PIMAX_grayscale_image_log',size(grayscale_image_log))
        h5write([analyzed_hdf5_folder,num2str(i),'_analyzed.h5'],'/Spectrometer_SpectraPro/PIMAX_grayscale_image_log',grayscale_image_log)
    end
end
clear grayscale_image grayscale_image_log color_image color_image_log plasma_image

%% Interferometer Analysis
for i=files_flip
    % determine if interferometer data was saved for shot i and if so which
    % daq was used to take the data, then use the interferometer_analysis.m
    % code to calculate phase shift and density from the raw I and Q
    % signals
    if data_exist(i).interferometer==1
        if strcmpi(h5readatt([analyzed_hdf5_folder,num2str(i),'_analyzed.h5'],'/Interferometer','daq_source'),'pxie')==1
            time_int=h5read([analyzed_hdf5_folder,num2str(i),'_analyzed.h5'],'/Time/PXIe(mu-s)');
        elseif strcmpi(h5readatt([analyzed_hdf5_folder,num2str(i),'_analyzed.h5'],'/Interferometer','daq_source'),'scope')==1
            time_int=h5read([analyzed_hdf5_folder,num2str(i),'_analyzed.h5'],'/Time/Scope(mu-s)');
        end
        sample_end=length(time_int);
        time_polyfit=[time_int(1),ceil(time_int(end))];
        I_raw=h5read([analyzed_hdf5_folder,num2str(i),'_analyzed.h5'],'/Interferometer/I_raw(V)');
        Q_raw=h5read([analyzed_hdf5_folder,num2str(i),'_analyzed.h5'],'/Interferometer/Q_raw(V)');
        [~,~,~,phi_adj_detrend_original,~,~]=interferometer_analysis(I_raw,Q_raw,time_int,time_polyfit,sample_end);
        % have the user choose which points between which MATLAB should use
        % its built-in polyfit function to detrend the data.  Choose two
        % points for the low and high range before the plasma signal and
        % two points for the low and high range after the plasma signal
        figure('Name',['User Input Points Between Which MATLAB Will Polyfit for Shot ',num2str(i),' Chord 1']);
        plot(time_int,phi_adj_detrend_original)
        xlim([-100 300])
```

```
        [x_input,~]=ginput;
        close
        time_polyfit=[x_input(1) x_input(2);x_input(3) x_input(4)];
        [~,phi_adj,phi_trend,phi_adj_detrend,density,samples_rog]=interferometer_analysis(I_raw,
            Q_raw,time_int,time_polyfit,sample_end);
        k=1;
        % if the first attempt at detrend is not suffient, give the option
        % to redo the detrend by inputing 0.  This will repeat this loop
        % and you will go through the point selection for detrend again.
        % If the detrend is sufficient, input 1.  Repeat this process as
        % many times as is necessary to obtain the proper detrended signal
        while k==1
            figure('Name',['Updated Interferometer Detrend for Shot ',num2str(i),' Chord 1'])
            plot(time_int,phi_adj_detrend)
            xlim([-10 150])
            prompt='Is the detrend sufficient? Enter 1 for yes or 0 for no';
            redo=input(prompt);
            close
            if redo==0
                B=figure('Name',['User Input Points Between Which MATLAB Will Polyfit for Shot ',
                    num2str(i),' Chord 1']);
                set(B,'Visible','off');
                plot(time_int,phi_adj_detrend)
                xlim([-100 300])
                [x_input,~]=ginput;
                close
                time_polyfit=[x_input(1) x_input(2);x_input(3) x_input(4)];
                [phi_adj_detrend,phi_adj,phi_trend,samples_rog]=third_order_detrend(
                    phi_adj_detrend,time_int,time_polyfit,sample_end);
                density=phi_adj_detrend.*(pi/180)./(1.778E-21);
            elseif redo==1
                break
            else
                disp('Please enter 1 or 0 as response to the prompt')
            end
        end
        h5create([analyzed_hdf5_folder,num2str(i),'_analyzed.h5'],'/Interferometer/
            Phase_shift_raw(degrees)',size(phi_adj))
        h5write([analyzed_hdf5_folder,num2str(i),'_analyzed.h5'],'/Interferometer/Phase_shift_raw
```

```
(degrees)',phi_adj)
    h5create([analyzed_hdf5_folder,num2str(i),'_analyzed.h5'],'/Interferometer/Phase_shift_detrended(degrees)',size(phi_adj_detrend))
    h5write([analyzed_hdf5_folder,num2str(i),'_analyzed.h5'],'/Interferometer/Phase_shift_detrended(degrees)',phi_adj_detrend)
    h5create([analyzed_hdf5_folder,num2str(i),'_analyzed.h5'],'/Interferometer/Line_integrated_density(cm^-2)',size(density))
    h5write([analyzed_hdf5_folder,num2str(i),'_analyzed.h5'],'/Interferometer/Line_integrated_density(cm^-2)',density./1E4)
    % create and save a plot of the interferometer analysis process
    % ending with a plot of the line-integrated density
    A=figure('Name',['Shot ',num2str(i),' Interferometer Analysis']);
    %set(A,'Visible','off');
    subplot(2,2,1)
    plot(time_int,I_raw)
    hold on
    plot(time_int,Q_raw)
    xlim([-10 100])
    xlabel('Time (\mus)')
    ylabel('Signal (Voltage)')
    legend({'I Raw','Q Raw'},'FontSize',8)
    subplot(2,2,2)
    plot(time_int,phi_adj)
    hold on
    plot(time_int,phi_trend,'--k','LineWidth',1)
    xlim([-10 100])
    xlabel('Time (\mus)')
    ylabel('Phase Shift (degrees)')
    legend({'Phase Shift Raw','Trend Line'},'FontSize',8)
    subplot(2,2,3)
    plot(time_int,phi_adj_detrend)
    if data_exist(i).rogowski_coil==1
        if strcmpi(h5readatt([analyzed_hdf5_folder,num2str(i),'_analyzed.h5'],'/Rogowski_Coil/Coil1','daq_source'),'pxie')==1
            time_Rog=h5read([analyzed_hdf5_folder,num2str(i),'_analyzed.h5'],'/Time/PXIe(mu-s)');
        elseif strcmpi(h5readatt([analyzed_hdf5_folder,num2str(i),'_analyzed.h5'],'/Rogowski_Coil/Coil1','daq_source'),'scope')==1
            time_Rog=h5read([analyzed_hdf5_folder,num2str(i),'_analyzed.h5'],'/Time/Scope(mu-
```

```
                s)');
            end
            rog_signal=h5read([analyzed_hdf5_folder,num2str(i),'_analyzed.h5'],'/Rogowski_Coil/Coil1/Current(kA)');
            hold on
            mult_factor=max(rog_signal)/max(phi_adj_detrend(samples_rog(1):samples_rog(end)));
            plot(time_Rog,rog_signal./mult_factor,'--k')
            legend({'Phase Shift Detrended','Normalized Rogowski Signal'},'FontSize',8)
        else
            legend({'Phase Shift Detrended'},'FontSize',8)
        end
        xlim([-10 100])
        xlabel('Time (\mus)')
        ylabel('Phase Shift (degrees)')
        subplot(2,2,4)
        plot(time_int,density./1E4)
        xlim([-10 100])
        xlabel('Time (\mus)')
        ylabel('Line-integrated n_e (cm^{-2})')
        fig=gcf;
        fig.PaperUnits='inches';
        fig.PaperPosition=[0 0 8 6];
        print(['../../../Figures_and_images/PNG/Interferometer/Shot',num2str(i),'_Interferometer_Analysis'],'-dpng','-r200')
        close

        if h5readatt([analyzed_hdf5_folder,num2str(i),'_analyzed.h5'],'/Interferometer','number_of_chords')==2
            if strcmpi(h5readatt([analyzed_hdf5_folder,num2str(i),'_analyzed.h5'],'/Interferometer','daq_source'),'pxie')==1
                time_int=h5read([analyzed_hdf5_folder,num2str(i),'_analyzed.h5'],'/Time/PXIe(mu-s)');
            elseif strcmpi(h5readatt([analyzed_hdf5_folder,num2str(i),'_analyzed.h5'],'/Interferometer','daq_source'),'scope')==1
                time_int=h5read([analyzed_hdf5_folder,num2str(i),'_analyzed.h5'],'/Time/Scope(mu-s)');
            end
            sample_end=length(time_int);
            time_polyfit=[time_int(1),ceil(time_int(end))];
```

```
I_raw=h5read([analyzed_hdf5_folder,num2str(i),'_analyzed.h5'],'/Interferometer/I2_raw
    (V)');
Q_raw=h5read([analyzed_hdf5_folder,num2str(i),'_analyzed.h5'],'/Interferometer/Q2_raw
    (V)');
[~,~,~,phi_adj_detrend_original,~,~]=interferometer_analysis(I_raw,Q_raw,time_int,
    time_polyfit,sample_end);
% have the user choose which points between which MATLAB should use
% its built-in polyfit function to detrend the data.  Choose two
% points for the low and high range before the plasma signal and
% two points for the low and high range after the plasma signal
B=figure('Name',['User Input Points Between Which MATLAB Will Polyfit for Shot ',
    num2str(i),' Chord 2']);
set(B,'Visible','off');
plot(time_int,phi_adj_detrend_original)
xlim([-100 300])
[x_input,~]=ginput;
close
time_polyfit=[x_input(1) x_input(2);x_input(3) x_input(4)];
[~,phi_adj,phi_trend,phi_adj_detrend,density,samples_rog]=interferometer_analysis(
    I_raw,Q_raw,time_int,time_polyfit,sample_end);
k=1;
% if the first attempt at detrend is not suffient, give the option
% to redo the detrend by inputing 0.  This will repeat this loop
% and you will go through the point selection for detrend again.
% If the detrend is sufficient, input 1.  Repeat this process as
% many times as is necessary to obtain the proper detrended signal
while k==1
    figure('Name',['Updated Interferometer Detrend for Shot ',num2str(i),' Chord 2'])
    plot(time_int,phi_adj_detrend)
    xlim([-10 150])
    prompt='Is the detrend sufficient? Enter 1 for yes or 0 for no';
    redo=input(prompt);
    close
    if redo==0
        B=figure('Name',['User Input Points Between Which MATLAB Will Polyfit for
            Shot',num2str(i),' Chord 2']);
        set(B,'Visible','off');
        plot(time_int,phi_adj_detrend)
        xlim([-100 300])
```

```
                [x_input,~]=ginput;
                close
                time_polyfit=[x_input(1) x_input(2);x_input(3) x_input(4)];
                [phi_adj_detrend,phi_adj,phi_trend,samples_rog]=third_order_detrend(
                    phi_adj_detrend,time_int,time_polyfit,sample_end);
                density=phi_adj_detrend.*(pi/180)./(1.778E-21);
            elseif redo==1
                break
            else
                disp('Please enter 1 or 0 as response to the prompt')
            end
        end
        h5create([analyzed_hdf5_folder,num2str(i),'_analyzed.h5'],'/Interferometer/
            Phase_shift_raw2(degrees)',size(phi_adj))
        h5write([analyzed_hdf5_folder,num2str(i),'_analyzed.h5'],'/Interferometer/
            Phase_shift_raw2(degrees)',phi_adj)
        h5create([analyzed_hdf5_folder,num2str(i),'_analyzed.h5'],'/Interferometer/
            Phase_shift_detrended2(degrees)',size(phi_adj_detrend))
        h5write([analyzed_hdf5_folder,num2str(i),'_analyzed.h5'],'/Interferometer/
            Phase_shift_detrended2(degrees)',phi_adj_detrend)
        h5create([analyzed_hdf5_folder,num2str(i),'_analyzed.h5'],'/Interferometer/
            Line_integrated_density2(cm^-2)',size(density))
        h5write([analyzed_hdf5_folder,num2str(i),'_analyzed.h5'],'/Interferometer/
            Line_integrated_density2(cm^-2)',density./1E4)
        % create and save a plot of the interferometer analysis process
        % ending with a plot of the line-integrated density
        A=figure('Name',['Shot ',num2str(i),' Interferometer Analysis Chord 2']);
        %set(A,'Visible','off');
        subplot(2,2,1)
        plot(time_int,I_raw)
        hold on
        plot(time_int,Q_raw)
        xlim([-10 100])
        xlabel('Time (\mus)')
        ylabel('Signal (Voltage)')
        legend({'I Raw','Q Raw'},'FontSize',8)
        subplot(2,2,2)
        plot(time_int,phi_adj)
        hold on
```

```
            plot(time_int,phi_trend,'--k','LineWidth',1)
            xlim([-10 100])
            xlabel('Time (\mus)')
            ylabel('Phase Shift (degrees)')
            legend({'Phase Shift Raw','Trend Line'},'FontSize',8)
            subplot(2,2,3)
            plot(time_int,phi_adj_detrend)
            if data_exist(i).rogowski_coil==1
                if strcmpi(h5readatt([analyzed_hdf5_folder,num2str(i),'_analyzed.h5'],'/
                    Rogowski_Coil/Coil1','daq_source'),'pxie')==1
                    time_Rog=h5read([analyzed_hdf5_folder,num2str(i),'_analyzed.h5'],'/Time/PXIe(
                        mu-s)');
                elseif strcmpi(h5readatt([analyzed_hdf5_folder,num2str(i),'_analyzed.h5'],'/
                    Rogowski_Coil/Coil1','daq_source'),'scope')==1
                    time_Rog=h5read([analyzed_hdf5_folder,num2str(i),'_analyzed.h5'],'/Time/Scope
                        (mu-s)');
                end
                rog_signal=h5read([analyzed_hdf5_folder,num2str(i),'_analyzed.h5'],'/
                    Rogowski_Coil/Coil1/Current(kA)');
                hold on
                mult_factor=max(rog_signal)/max(phi_adj_detrend(samples_rog(1):samples_rog(end)))
                    ;
                plot(time_Rog,rog_signal./mult_factor,'--k')
                legend({'Phase Shift Detrended','Normalized Rogowski Signal'},'FontSize',8)
            else
                legend({'Phase Shift Detrended'},'FontSize',8)
            end
            xlim([-10 100])
            xlabel('Time (\mus)')
            ylabel('Phase Shift (degrees)')
            subplot(2,2,4)
            plot(time_int,density./1E4)
            xlim([-10 100])
            xlabel('Time (\mus)')
            ylabel('Line-integrated n_e (cm^{-2})')
            fig=gcf;
            fig.PaperUnits='inches';
            fig.PaperPosition=[0 0 8 6];
            print(['../../../Figures_and_images/PNG/Interferometer/Shot',num2str(i),'
```

```
                _Interferometer_Analysis_Chord2'],'-dpng','-r200')
            close
        end
    end
end
clear A B data_exist density fig files i I_raw info k mult_factor phi_adj phi_adj_detrend
    phi_adj_detrend_original phi_trend prompt Q_raw redo rog_signal sample_end samples_rog
    time_int time_polyfit time_Rog x_input
```

A.3 MATLAB functions

This section contains MATLAB functions that are required and used in the two codes listed above.

A.3.1 read_raw_data.m

```
% This function takes a single specified shot number and reads data for
% that shot from the oscilloscope, NI PXIe, and both spectrometers

function [time_pxie,Ch0,Ch1,Ch2,Ch3,Ch4,Ch5,Ch6,Ch7,time_scope,scope1,scope2,scope3,scope4,spec,
    pxie_sample_rate,pxie_sample_number,time_data_acq,pxie_sample_spark_gap_start,
    scope_sample_spark_gap_start,time_gas_puff,time_pxie_max,time_pxie_step,scope_sample_number,
    scope_sample_rate,time_scope_step,time_scope_max,pxie_file_exist,scope_file_exist,
    spec_file_exist] = read_raw_data(shot_number)

% Read data from NI PXIe
pxie_file_exist=exist(['../Data/',num2str(shot_number),'.h5'],'file'); % determine if .h5 data
    was saved for this shot number
if pxie_file_exist==2 % if .h5 data was saved import the .h5 data saved for each of the 8 pxie
    channels
        Ch0=h5read(['../Data/',num2str(shot_number),'.h5'],'/RogowskiCoil1_Data/Y1_Data');
        Ch1=h5read(['../Data/',num2str(shot_number),'.h5'],'/Photodiodes_Data/Y2_Data');
        Ch2=h5read(['../Data/',num2str(shot_number),'.h5'],'/Interferometer_Data/Y1_Data');
        Ch3=h5read(['../Data/',num2str(shot_number),'.h5'],'/Interferometer_Data/Y2_Data');
```

```
        Ch4=h5read(['../Data/',num2str(shot_number),'.h5'],'/RogowskiCoil2_Data/Y1_Data');
        Ch5=h5read(['../Data/',num2str(shot_number),'.h5'],'/RogowskiCoil3_Data/Y1_Data');
        Ch6=h5read(['../Data/',num2str(shot_number),'.h5'],'/RogowskiCoil4_Data/Y1_Data');
        Ch7=h5read(['../Data/',num2str(shot_number),'.h5'],'/Photodiodes_Data/Y1_Data');

        % import important pxie shot attributes and meta data as well
        pxie_sample_rate=h5readatt(strcat('../Data/',num2str(shot_number),'.h5'),'/
            Interferometer_Data/Y1_Data','Samples_Second');
        pxie_sample_number=h5readatt(strcat('../Data/',num2str(shot_number),'.h5'),'/
            Interferometer_Data/Y1_Data','Number_Of_Samples');
        time_gas_puff=round(-1E6*h5readatt(strcat('../Data/',num2str(shot_number),'.h5'),'/
            Interferometer_Data/Y1_Data','Delay_Between_Spark_Gap_Switch_and_Gas_Puff_Valve (s)')
            );
        time_data_acq=time_gas_puff+round(-1E6*h5readatt(strcat('../Data/',num2str(shot_number),'
            .h5'),'/Interferometer_Data/Y1_Data','
            Delay_Between_Gas_Puff_Valve_and_Data_Acquisition_Trigger (s)'));
        time_pxie_max=(1E6*pxie_sample_number/pxie_sample_rate)+time_data_acq;
        time_pxie_step=1E6*(1/pxie_sample_rate);
        pxie_sample_spark_gap_start=round(pxie_sample_number*(-time_data_acq/(time_pxie_max-
            time_data_acq)));
        time_pxie=time_data_acq:time_pxie_step:time_pxie_max-time_pxie_step;
else % if no .h5 data is found, save pxie variables as empty matrices, and alert user
    Ch0=[];
    Ch1=[];
    Ch2=[];
    Ch3=[];
    Ch4=[];
    Ch5=[];
    Ch6=[];
    Ch7=[];

    pxie_sample_rate=[];
    pxie_sample_number=[];
    time_gas_puff=[];
    time_data_acq=[];
    time_pxie_max=[];
    time_pxie_step=[];
    pxie_sample_spark_gap_start=[];
    time_pxie=[];
```

```
    disp(['No PXIe data .h5 file was found for Shot ',num2str(shot_number)])
end

% Read data from oscilloscope
scope_file_exist=exist(['../Data/',num2str(shot_number),'.csv'],'file'); %determine is scope data was saved for this shot number

% user input data acquisition start time if scope data was collected but
% pxie data was not
if scope_file_exist==2 && pxie_file_exist==0
    prompt=['At what time in microseconds did scope data collection begin relative to the spark gap trigger for Shot ',num2str(shot_number),'?'];
    time_data_acq=input(prompt);
end

if scope_file_exist==2 % if scope data was saved, import data for however many channels collected data (1-4)
    scope=csvread(['../Data/',num2str(shot_number),'.csv'],2,0);
    if size(scope,2)==2
        time_scope=1E6.*scope(:,1);
        scope1=scope(:,2);
        scope2=[];
        scope3=[];
        scope4=[];
    elseif size(scope,2)==3
        time_scope=1E6.*scope(:,1);
        scope1=scope(:,2);
        scope2=scope(:,3);
        scope3=[];
        scope4=[];
    elseif size(scope,2)==4
        time_scope=1E6.*scope(:,1);
        scope1=scope(:,2);
        scope2=scope(:,3);
        scope3=scope(:,4);
        scope4=[];
    else
        time_scope=1E6.*scope(:,1);
```

```
        scope1=scope(:,2);
        scope2=scope(:,3);
        scope3=scope(:,4);
        scope4=scope(:,5);
    end
    % save important scope attributes as well
    scope_sample_number=size(scope,1);
    scope_sample_rate=1/(scope(2,1)-scope(1,1));
    time_scope_step=(1E6*(1/scope_sample_rate));
    time_scope=time_scope+time_data_acq;
    scope_sample_spark_gap_start=round(((time_scope(1)*-1)/(time_scope(end)+time_scope_step-
        time_scope(1)))*scope_sample_number);
    time_scope_max=(1E6*scope_sample_number/scope_sample_rate)+time_data_acq;
else % if no scope file was found, save scope variables as empty matrices and alert user
    time_scope=[];
    scope1=[];
    scope2=[];
    scope3=[];
    scope4=[];

    scope_sample_number=[];
    scope_sample_rate=[];
    time_scope_step=[];
    scope_sample_spark_gap_start=[];
    time_scope_max=[];

    disp(['No scope data .csv file was found for Shot ',num2str(shot_number)])
end

%Read data from spectrometer
spec_file_exist_thorlabs=exist(['../Data/spec',num2str(shot_number),'txt.txt'],'file'); %
    determine if data was saved for the Thorlabs spectrometer
spec_file_exist_pi=exist(['../Data/pimax',num2str(shot_number),'.csv'],'file'); % determine if
    data was saved for the PI SpectraPro spectrometer
if spec_file_exist_thorlabs==2 && spec_file_exist_pi==2 % if both files exist, import and save
    data from both spectrometers
    spec_file_exist=2;
    spec1=importdata(['../Data/spec',num2str(shot_number),'txt.txt']);
    spec(1).wavelength=spec1(:,1);
```

```
    spec(1).intensity=spec1(:,2);
    spec(1).row=[];
    spec(1).source='Thorlabs';
    spec2=csvread(['../Data/pimax',num2str(shot_number),'.csv']);
    spec(2).wavelength=reshape(spec2(:,1),[1024 1024]);
    spec(2).intensity=reshape(spec2(:,2),[1024 1024]);
    spec(2).row=reshape(spec2(:,3),[1024 1024]);
    spec(2).source='SpectraPro';
elseif spec_file_exist_thorlabs==2 && spec_file_exist_pi==0 % if only the Thorlabs spectrometer
    data exists, import and save that data
    spec_file_exist=2;
    spec1=importdata(['../Data/spec',num2str(shot_number),'txt.txt']);
    spec(1).wavelength=spec1(:,1);
    spec(1).intensity=spec1(:,2);
    spec(1).row=[];
    spec(1).source='Thorlabs';
elseif spec_file_exist_thorlabs==0 && spec_file_exist_pi==2 % if only the PI SpectraPro
    spectrometer data exists, import and save that data
    spec_file_exist=2;
    spec2=csvread(['../Data/pimax',num2str(shot_number),'.csv']);
    spec(1).wavelength=reshape(spec2(:,1),[1024 1024]);
    spec(1).intensity=reshape(spec2(:,2),[1024 1024]);
    spec(1).row=reshape(spec2(:,3),[1024 1024]);
    spec(1).source='SpectraPro';
elseif spec_file_exist_thorlabs==0 && spec_file_exist_pi==0 % if no spectrometer data saved,
    alert user
    spec_file_exist=0;
    spec(1).wavelength=[];
    spec(1).intensity=[];
    spec(1).row=[];
    spec(1).source=[];
    disp(['No spectrometer data file was found for Shot ',num2str(shot_number)])
end
```

A.3.2 interferometer_analysis.m

```
% function to convert raw I and Q interferometer traces into phase shift
```

```
% and line-integrated density traces.

function [phi,phi_adj,phi_trend,phi_adj_detrend,density,samples_Rog]=interferometer_analysis(I,Q,
    time,time_polyfit,sample_number)

set(0,'DefaultAxesXGrid','on','DefaultAxesYGrid','on') %turn grid on for all plots
set(0,'DefaultAxesFontSize',12) %change the default figure axes font size

phi=atan2(Q,I)*180/pi; % calculate raw phase shift

% remove jumps that appear as a result of taking the inverse tan
order=zeros(length(phi),1);
for j=1:1:length(phi)-1
    if phi(j+1)-phi(j)<-180
        order(j+1:length(phi))=order(j)+1;
    elseif phi(j+1)-phi(j)>180
        order(j+1:length(phi))=order(j)-1;
    end
end
phi_adj=phi+360*order;

% detrend data based on user-provided "time-polyfit" variable.  See the
% main "analysis_processing_and_plotting_hdf5" code for details
samples_polyfit=[];
for i=1:size(time_polyfit,1)
    samples_polyfit=[samples_polyfit,round(((((time_polyfit(i,1)-time(1))/(ceil(time(end))-time
        (1)))*sample_number)+100):100:((time_polyfit(i,2)-time(1))/(ceil(time(end))-time(1))*
        sample_number))];
end

samples_Rog=samples_polyfit(1):samples_polyfit(end);

p=polyfit(time(samples_polyfit),phi_adj(samples_polyfit),3);
phi_trend=(p(1).*time.^3+p(2).*time.^2+p(3).*time+p(4));
phi_adj_detrend=phi_adj-(p(1).*time.^3+p(2).*time.^2+p(3).*time+p(4)); % calculate detrended
    phase shift

density=phi_adj_detrend.*(pi/180)./(1.778E-21); %convert to line-integrated density based on
    laser and IF setup as of Dec. 2019
```

A.3.3 pimax_analysis.m

```
% function to convert raw images taken with the PIMAX iCCD camera into
% grayscale and false color PNGs

% Inputs
%   pimax_raw: raw pimax data (create using "imread" command on .tiff file)
%   file_number: shot number to be used when saving PNGs to file
%   data_source: set as 1 if image is a direct plasma image and set as 0 if
%   image is a spectral image

function [image_double,image_double_log,image_double_color,image_double_color_log]=pimax_analysis
    (pimax_raw,file_number,data_source)

%convert image to type double and scale, create a logarithmic scale version
%as well
image_double=im2double(pimax_raw);
image_double_log=log(image_double);
min_double=min(image_double(:));
min_double_log=min(image_double_log(:));
max_double=max(image_double(:));
max_double_log=max(image_double_log(:));
image_double=(image_double-min_double)./(max_double-min_double);
image_double_log=(image_double_log-min_double_log)./(max_double_log-min_double_log);

% save grayscale images to PNG files, one with and one without the
% logarithmic scale
if data_source==1
    imwrite(image_double,['../../../Figures_and_Images/PNG/PIMAX_Images/Plasma_Images/PIMAX',
        num2str(file_number),'grayscale.png'])
    imwrite(image_double_log,['../../../Figures_and_Images/PNG/PIMAX_Images/Plasma_Images/PIMAX',
        num2str(file_number),'grayscale_log.png'])
elseif data_source==0
    imwrite(image_double,['../../../Figures_and_Images/PNG/PIMAX_Images/Spectrometer_Images/PIMAX
        ',num2str(file_number),'grayscale.png'])
    imwrite(image_double_log,['../../../Figures_and_Images/PNG/PIMAX_Images/Spectrometer_Images/
        PIMAX',num2str(file_number),'grayscale_log.png'])
end

```

```
% if the image is a direct plasma image, also create a false-color version
% using the "parula" colormap and save a PNG of the logarithmic and
% non-logarithmic version of each of these as well
if data_source==1
    image_double_color_log=image_double_log.*255+1;
    image_double_color=image_double.*255+1;
    imwrite(image_double_color,parula(256),['../../../Figures_and_Images/PNG/PIMAX_Images/
        Plasma_Images/PIMAX',num2str(file_number),'parula.png'])
    imwrite(image_double_color_log,parula(256),['../../../Figures_and_Images/PNG/PIMAX_Images/
        Plasma_Images/PIMAX',num2str(file_number),'parula_log.png'])
elseif data_source==0
    image_double_color=[];
    image_double_color_log=[];
end
```

A.3.4 rogowski_analysis.m

```
% function to integrate raw Rogowski coil signal and detrend integrated
% signal.  The function also calculates and saves the delay between when
% the spark gap switch was triggered and when the Rogowski coil saw current
% start to rise.  When prompted, user should select the point of the shown
% figure where the trace begins to rise steeply, then press enter.

function [Rog_current_raw,Rog_current_detrend_calibrated,Rog_current_trend_line,shot_delay]=
    rogowski_analysis(Rog,calibration_factor,time,sample_rate,sample_start,sample_number,
    shot_number)

time=time.*10^-6; %convert back to seconds
Rog_current_raw=cumtrapz(time,Rog); %integrate raw signal

max_delay=1; %maximum allowable spark gap switch jitter in microseconds

% plot and have user choose point where rise in current begins, this will
% be defined as the spark gap delay
[~,index]=max(Rog);
if index>sample_start+(max_delay*1E-6*sample_rate)
    figure('Name',['Shot ',num2str(shot_number),' Raw Rogowski Coil Signal'])
```

```
    plot(Rog)
    xlim([index-(max_delay*1E-6*2*sample_rate),index+(max_delay*1E-6*2*sample_rate)])
    [x_input,~]=ginput;
    shot_delay=(time(round(x_input))).*1E6;
    close
else
    shot_delay=0;
    x_input=sample_start;
end

% use MATLAB polyfit function to detrend integrated signal
samples_polyfit=[1:x_input,round(x_input+(sample_rate*200*1E-6)):sample_number];
p=polyfit(time(samples_polyfit),Rog_current_raw(samples_polyfit),2);
Rog_current_trend_line=(p(1).*time.^2+p(2).*time+p(3));
Rog_current_detrend_calibrated=(Rog_current_raw-(p(1).*time.^2+p(2).*time+p(3))).*
    calibration_factor;
Rog_current_detrend_calibrated=Rog_current_detrend_calibrated-Rog_current_detrend_calibrated(
    sample_start);
```

A.4 Plotting interferometer average and standard deviation

```
%Code for averaging interferometer traces and plotting the average trace
%with standard deviation also plotted as a semi-transparent shape

%This example code shows how to plot the average and standard deviation of
%two data sets on the same plot, in this case chords 1 and 2 of the same
%set of shots.  If you'd like to plot additional groups just add additional
%variables definiting more sets of shots and copy and past code segments to
%add more groups

%Note that the function titled "function_matlab_plot_color" is needed to
%run this code.

%% Starting Commands
```

```
close all
clear variables
clc
set(0,'DefaultAxesXGrid','on','DefaultAxesYGrid','on') %turn grid on for all plots
set(0,'DefaultAxesFontSize',14) %change the default figure axes font size

%% User-input parameters
shots=[1077:1097,1099:1122]; % what shots should be averaged
hdf5_folder='../../Analyzed_hdf5_data_files/'; % folder directory where analyzed hdf5 files for
    the shots above are contained

%% Pre-allocate matrices
max_matrix=zeros(length(shots),7);
int1_matrix=zeros(18001,length(shots));
int2_matrix=zeros(18001,length(shots));

%% Create figure showing individual traces for all shots
% Create a plot that shows the individual traces that will be averaged all
% on the same plot, show the groups in the same color.  This helps to find
% any outliers and to see detail features that may be lost when the average
% is taken
figure('Name','Individual traces for all shots')

% first chord shots
for i=1:length(shots)
    %Load time delay between when spark gap was trigered and when current
    %rise began and subtract this time from the time array
    time_delay=h5readatt([hdf5_folder,num2str(shots(i)),'_analyzed.h5'],'/Rogowski_Coil/Coil1','
        t_spark_gap_delay(mu-s)');
    time=h5read([hdf5_folder,num2str(shots(i)),'_analyzed.h5'],'/Time/PXIe(mu-s)');
    time=time-time_delay;
    % find the index of the new time array above -100 microseconds and
    % below 200 microseconds so that all shots will have a line integrated
    % density array corresponding to the same time array
    index_above_neg100us=find(abs(time+100)<0.005);
    index_below_pos200us=find(abs(time-200)<0.005);
    time_plot=time(index_above_neg100us:index_below_pos200us);
    %load line integrated interferometer data
```

```
    int1=h5read([hdf5_folder,num2str(shots(i)),'_analyzed.h5'],'/Interferometer/
        Line_integrated_density(cm^-2)');
    int1_matrix(:,i)=int1(index_above_neg100us:index_below_pos200us);
    a=plot(time_plot,-int1_matrix(:,i),'color',function_matlab_plot_color(1));
    hold on
end

% second chord shots, same commands as above the only different is the hdf5
% dataset name has a 2 at the end to denote the second chord
for i=1:length(shots)
    time_delay=h5readatt([hdf5_folder,num2str(shots(i)),'_analyzed.h5'],'/Rogowski_Coil/Coil1','
        t_spark_gap_delay(mu-s)');
    time=h5read([hdf5_folder,num2str(shots(i)),'_analyzed.h5'],'/Time/PXIe(mu-s)');
    time=time-time_delay;
    index_above_neg100us=find(abs(time+100)<0.005);
    index_below_pos200us=find(abs(time-200)<0.005);
    time_plot=time(index_above_neg100us:index_below_pos200us);
    int2=h5read([hdf5_folder,num2str(shots(i)),'_analyzed.h5'],'/Interferometer/
        Line_integrated_density2(cm^-2)');
    int2_matrix(:,i)=int2(index_above_neg100us:index_below_pos200us);
    b=plot(time_plot,-int2_matrix(:,i),'color',function_matlab_plot_color(2));
end

% set plot parameters, add a legend, annotation, and axes labels
xlim([15 40])
xlabel('Time (\mus)')
ylabel('Line-integrated n_e (cm^{-2})')
legend([a b],{'Chord 1','Chord 2'},'Location','northwest')
dim=[0.5 0.15 0.1 0.05];
str='add string here is desired';
annotation('textbox',dim,'String',str,'FitBoxtoText','on','FontSize',10,'EdgeColor','none');

% save a PNG of this plot
fig=gcf;
fig.PaperUnits='inches';
fig.PaperPosition=[0 0 6 4.5];
print('Interferometer_all_shots_individual_traces_plot','-dpng','-r300')

```

```
%% Create a figure showing the same shots as the figure created above, but this time plotting the
    average and 1 sigma standard deviation for each chord location
% take the average and standard devaition of each group
int1_mean=mean(int1_matrix,2,'omitnan');
int1_std=std(int1_matrix,0,2,'omitnan');
int2_mean=mean(int2_matrix,2,'omitnan');
int2_std=std(int2_matrix,0,2,'omitnan');

figure('Name','Interferometer Averaged Data for Shots 541-593')

% chord 1 average and standard deviation, plot the average trace and plot
% the average trace plus and minus the standard deviation but set the
% LineStyle to "none".  This will be used later to denote the area to fill
% for the standard deviation
a=plot(time_plot,-int1_mean,'color',function_matlab_plot_color(1),'LineWidth',2);
hold on
plot(time_plot,-int1_mean-int2_std,'LineStyle','none')
hold on
plot(time_plot,-int1_mean+int2_std,'LineStyle','none')
hold on
% define region to be filled in with the semi-transparent shape to show the
% standard deviation and plot it
time_fill=[time_plot',fliplr(time_plot')];
inBetween=[(-int1_mean-int1_std)',fliplr((-int1_mean+int1_std)')];
h=fill(time_fill,inBetween,function_matlab_plot_color(1));
set(h,'EdgeColor','none')
% set alpha to a value between 0 (completely transparent) and 1 (completely
% opaque)
alpha(0.3)

%chord 2 average and standard deviation, do the same for the second group
b=plot(time_plot,-int2_mean,'color',function_matlab_plot_color(2),'LineWidth',2);
hold on
plot(time_plot,-int2_mean-int2_std,'LineStyle','none')
hold on
plot(time_plot,-int2_mean+int2_std,'LineStyle','none')
hold on
time_fill=[time_plot',fliplr(time_plot')];
inBetween=[(-int2_mean-int2_std)',fliplr((-int2_mean+int2_std)')];
```

```
h=fill(time_fill,inBetween,function_matlab_plot_color(2));
set(h,'EdgeColor','none')
alpha(0.3)

% additional plot commands
xlabel('Time (\mus)')
ylabel('Line-integrated n_e (cm^{-2})')
xlim([15 40])
legend([a b],{'chord 1','chord 2'},'Location','northwest')
dim=[0.5 0.15 0.1 0.05];
str='add string here if desired';
annotation('textbox',dim,'String',str,'FitBoxtoText','on','FontSize',14,'EdgeColor','none');

% save a PNG of this figure
fig=gcf;
fig.PaperUnits='inches';
fig.PaperPosition=[0 0 6 4.5];
print('Interferometer_all_shots_average_and_stdev','-dpng','-r300')
```

A.5 Comparing PrismSPECT simulations to experimental spectral data

```
% Code to import PrismSPECT simulations and plot them against experiment
% data imported from saved .mat data files created in another code

%% Starting Commands
close all
clear variables
clc
set(0,'DefaultAxesXGrid','on','DefaultAxesYGrid','on') %turn grid on for all plots
set(0,'DefaultAxesFontSize',10) %change the default figure axes font size

%% User-input variables
%what densities, temperatures, and species do you want to import?  Input
%values as strings just as they appear in the .ppd file name
```

```
density=["4.8e16"];
temperature=["1.6","1.8","2","2.2","2.4","2.6","2.8","3"];
species=["ArII"];
include_all_species_plot=0; %if you saved and want to load the plot with all spectral lines make
    this 1, otherwise set it to 0

%numbered simulation to import, note, file must be named sim# when it is
%saved in PrismSPECT
sim_number=6;

%% Plot intensities simulated using PrismSPECT
% Depending on whether a single or multiple densities, temperatures, and
% species were simulated, the code will import that data and place it in
% the "data" structure, with substructures for density, temperature, and
% species.
if length(density)==1
    if length(temperature)==1
        if length(species)==1
            % fill in correct commands if this is the case
        else
            for k=1:length(species)
                fileID=fopen(strcat('../../PrismSPECT/2019_10_31/sim',num2str(sim_number),'_(',
                    species(k),') _ 0.ppd'),'r');
                cell_data=textscan(fileID,'%f%f','headerlines',7);
                data_array=[cell2mat(cell_data(1)),cell2mat(cell_data(2))];
                data.density(1).temperature(1).species(k).data=data_array;
                fclose(fileID);
            end
            if include_all_species_plot==1
                % fill in correct commands if this is the case
            end
        end
    else
        for j=1:length(temperature)
            if length(species)==1
                fileID=fopen(strcat('../../PrismSPECT/2019_10_31/sim',num2str(sim_number),'_(',
                    species(1),') _',{' '},temperature(j),' _ 0.ppd'),'r');
                cell_data=textscan(fileID,'%f%f','headerlines',7);
                data_array=[cell2mat(cell_data(1)),cell2mat(cell_data(2))];
```

```
                data.density(1).temperature(j).species(1).data=data_array;
                fclose(fileID);
                if include_all_species_plot==1
                    fileID=fopen(strcat('PrismSPECT/2019_10_15/sim',num2str(sim_number),'/sim',
                        num2str(sim_number),'_',temperature(j),' _ 0.ppd'),'r');
                    cell_data=textscan(fileID,'%f%f','headerlines',7);
                    data_array=[cell2mat(cell_data(1)),cell2mat(cell_data(2))];
                    data.density(1).temperature(j).species(2).data=data_array;
                    fclose(fileID);
                end
            else
                for k=1:length(species)
                    fileID=fopen(strcat('../../PrismSPECT/2019_10_31/sim',num2str(sim_number),'_(
                        ',species(k),') _',{' '},temperature(j),' _ 0.ppd'),'r');
                    cell_data=textscan(fileID,'%f%f','headerlines',7);
                    data_array=[cell2mat(cell_data(1)),cell2mat(cell_data(2))];
                    data.density(1).temperature(j).species(k).data=data_array;
                    fclose(fileID);
                end
                if include_all_species_plot==1
                    for k=1:length(species)
                        fileID=fopen(strcat('PrismSPECT/2019_10_15/sim',num2str(sim_number),'/sim
                            ',num2str(sim_number),'_',temperature(j),' _ 0.ppd'),'r');
                        cell_data=textscan(fileID,'%f%f','headerlines',7);
                        data_array=[cell2mat(cell_data(1)),cell2mat(cell_data(2))];
                        data.density(1).temperature(j).species(k+1).data=data_array;
                        fclose(fileID);
                    end
                end
            end
        end
    end
else
    if length(temperature)==1
        if length(species)==1
            % fill in correct commands if this is the case
        else
            % fill in correct commands if this is the case
            if include_all_species_plot==1
```

```
                % fill in correct commands if this is the case
            end
        end
    else
        if length(species)==1
            % fill in correct commands if this is the case
            if include_all_species_plot==1
                % fill in correct commands if this is the case
            end
        else
            % fill in correct commands if this is the case
            if include_all_species_plot==1
                % fill in correct commands if this is the case
            end
        end
    end
end

%% Comparing to pre-saved experimental data
% this section of the code loads pre-saved experimental data and plots the
% data against the prismSPECT simulations that were loaded above.  This
% section is meant as a guide but should be altered to match what the user
% wants to plot

load spectrometer_shock_data % the name of the data file where experimental data is stored

% example figure that plots all the PrismSPECT data for each temperature
% against loaded experimental data, and normalizes each such that the max
% of each trace is 1
figure('Name','Comparison to first jet unobstructed data')
for i=1:length(temperature)
    plot(data.density(1).temperature(i).species(1).data(:,1),data.density(1).temperature(i).
        species(1).data(:,2)./max(data.density(1).temperature(i).species(1).data(:,2)),'LineWidth
        ',2)
    hold on
end
plot(wavelength_460-0.1,(jet1_unobstructed_intensity_460./max(jet1_unobstructed_intensity_460))-
    trend,'--k')
legend('1.6 eV','1.8 eV','2.0 eV','2.2 eV','2.4 eV','2.6 eV','2.8 eV','3.0 eV','exp')
```

```
xlabel('Wavelength (nm)')
ylabel('Intensity (A.U.)')
```